UNIVERSITÀ DEGLI STUDI DI TRIESTE

XXX CICLO DEL DOTTORATO DI RICERCA IN SCIENZE DELLA TERRA E MECCANICA DEI FLUIDI

LARGE EDDY SIMULATION OF A MARINE TURBINE IN A STABLE STRATIFIED FLOW CONDITION

Settore scientifico-disciplinare: ICAR/01 IDRAULICA

Ph.D. Student:
ANNA BRUNETTI

Ph.D. Program Director:
PROF. PIERPAOLO OMARI

Thesis Supervisor:
PROF. VINCENZO ARMENIO

ANNO ACCADEMICO 2016/2017

Abstract

The present study concerns the evaluation of the effects of stable stratified condition on turbine performance and wake development. The numerical analysis has been carried out by means of Large Eddy simulation (LES) through the in-house LES-COAST model coupled with a turbine module that computes the turbine induced forces. The capability of the model in reproducing power and thrust characteristics of a turbine has been proved from the comparison between the numerical results and the experimental data supplied by literature. Since the stratification is an important factor in the marine dynamics, the aim is to evaluate the interaction between the stratification and the turbine. Moreover the overall power production of a tidal farm and the power output of the single turbines can be influenced by the effects that stratification entails on the flow field. To the best of our knowledge, in the marine field there is no research aimed at studying the influence of marine stratification on wake recover and turbine performance. Tidal sites where marine turbines are installed can be subject to the presence of density stable stratified conditions. The density stratification is due to temperature and/or salinity variations between the superficial and the bottom water. In order to evaluate the influence of stratification on power output and wake development and recover, we simulated two types of stable stratified condition: a weak and a strong stratification. The weak stratification has been simulated imposing a temperature jump in order to obtain a vertical density profile with a step shape. For the strong stratification, we imposed a salinity jump with a step shape which gives rise to an higher density variation compared to the weak case. Then the turbine has been introduced into the stratified fields and the results have been compared. The analysis of the results highlights that the stratification has an impact on turbine production and on wake development and recover. Moreover the turbine mixing effect is analyzed.

Table of contents

Chapter 1

Introduction

The development of efficient renewable energy technologies is still a technological challenge for engineers and scientists all over the world. In particular, oceans and seas are a consistent source of kinetic energy that could be converted in electricity. Areas characterized by high tidal stream potential have been identified, where peak flow rates are around 4-5 m/s. Over the next 30 years, it seems possible that thousand of turbines will be placed in situ, with a total installed capacity up to 3 GW [1]. Although research on marine turbines deal with several areas of interest, the most investigated topic is definitely the power performance issue. As for wind farms, the wakes behind the rotors cause a reduction of velocity and hence a decrease in energy extraction. Finding the optimal configuration is crucial in order to gather as much energy as possible, thus making the technology competitive in the renewable energy scenario. For this purpose, several studies have been carried out to evaluate efficiency and energy production. Most of them concerns experimental investigations and numerical simulations of a single turbine. In their study, Bai et al. [2] predicted power performance of a marine current turbine under a free surface through a finite volume solver coupled with immersed boundary method. Two free surface methods have been applied and validated. Then the power coefficient at different tip speed ratios was calculated and the results compared with reference experimental data exhibiting a general good agreement. Noruzi et al. [3] carried out a numerical simulations by means of Reynolds-averaged Navier-Stokes (RANS) with and without gravity waves and the results were compared to experimental data. The results showed that when the ratio between the installation depth and the total depth of the domain is below a critical value, the installation depth of the rotor influences the performance of the turbine. A few studies concern the investigation of power performance of turbines arrays. Mycek et al. [4] carried out an experimental and numerical study both for a single turbine and for two turbines. A three-dimensional software was employed based on a Lagrangian vortex particle method for numerical

simulations. The study showed that the turbine is deeply affected by the presence of an upstream device in terms of power coefficient and thus of power production. Churchfield et al. [5] performed Large Eddy Simulation (LES) to study power production and wake propagation of tidal turbines array. The LES model was coupled with a rotating actuator line method for modeling the turbines. This work highlights that the application of the tangential forces induced by the turbines is important in reproducing the wake asymmetry that develops behind turbines. Moreover, it shows that the inflow turbulent characteristics affect significantly the propagation and power production of the turbine array.

As mentioned before, concerning turbine farm dynamics, the power production, although influenced by many factors, is connected to the wake development downstream of rotors. If the downstream turbines are remarkably affected by wakes of upstream turbines, both the efficiency of the single turbine and the global array efficiency are subject to a decrease in terms of power that can be extracted. For this reason, many studies focused on the investigation of wake characteristics and development under different flow conditions. Maganga et al. [6] performed experimental tests in order to study the flow effects on marine turbine wake characteristics and turbine performance. The aim of the study was also to supply an experimental database available for the validation of numerical studies. In this work, the power performance of a turbine was measured for different flow conditions and turbine configurations: different speed rates and inflow fields and three immersions of the blades tip. Moreover, the impact of two levels of turbulence intensity rates on wake development and behavior was investigated. The experimental results showed that the velocity recovery is faster in the area of higher ambient turbulence intensity. Moreover, the study indicates high loading fluctuations on the blades in the case of higher ambient turbulence intensity. Other studies, both numerical and experimental, focused on the effects of turbulence intensity on wake recover [7] [8].

Although the working principle of a marine turbine is similar to the wind device, comparatively, less research has been done in the marine field. This is definitely true as concerns the environmental stratification issue. In the wind field, the effects of atmospheric stratification has been taken into account. Zhang et al. [9] studied the effects of thermal stability on the wind-turbine wakes. In their study, wind-tunnel experiments were carried out with a simulated convective boundary layer and a neutral boundary layer. The results highlight that the velocity deficit is smaller in the convective case compared to the neutral case, in particular the velocity deficit at the wake center is about 15% less than for the convective case. Churchfield et al. [10] studied the effects of convective atmospheric turbulence on power performance of a wind turbine. The numerical study was carried out through LES and the turbine was modeled with an actuator line method coupled to a wind turbine structural and system dynamic model. They simulated and computed the power performance of a turbine placed 7 diameters downstream of another turbine. The results showed that

under the unstable condition the power production of the downstream turbine was 15%-20% higher than under neutral condition. Abkar et al. [11] studied the influence of thermal stability on a wind turbine wake. The study was performed by means of LES coupled with the actuator disk model with rotation to compute the turbine induced forces. The turbine wake behavior was studied under three atmospheric conditions: neutral, convective and stable conditions. The results showed that the wake recovers faster if it is subject to a convective atmospheric boundary layer compared to neutral and stable conditions. Moreover, the study indicates that the wake velocity deficit is well characterized by an analytical model based on the assumption of a self-similar Gaussian distribution.

Going back to the marine field, a few studies have been performed on the marine stratification issue. They concern mainly the study at large scales of the turbine extraction effects on stratification. Yang et al. [12] studied the effects of tidal energy extraction due to the presence of tidal turbines, on estuarine hydrodynamics in a stratified estuary. The study was performed numerically by means of a 3-D unstructured-grid Finite Volume Community Ocean Model (FVCOM) coupled with a tidal turbine module. The sink term added to the momentum equations of the FVCOM is computed through the turbine module as a function of the thrust coefficient and drag of turbines. The idealized model domain consists of a semi-enclosed bay that is forced by the upstream river discharge and tidal forcing through a narrow tidal channel. The annual cycle with seasonal variability of stratification and two-layer estuarine circulation was simulated with forcing of tide, river inflow, and meteorological heat flux. The main outcome of the study is that the effect of energy extraction on the surface tidal current is the phase shift. Moreover the results show that the power extraction has an effect on salinity/temperature stratification: the difference between surface salinity/temperature and bottom salinity/temperature decreases as the number of turbines installed increases. De Dominicis et al. [13] studied numerically the potential effects on the hydrodynamics of Pentland Firth site, caused by a realistic large arrays of tidal turbines. This investigation has been carried out through FVCOM, whereas the turbines are parameterized with a sink approach: the loss of momentum due to tidal energy extraction is calculated as a function of the thrust coefficient and it is added to the 3D momentum equations. The authors studied the influence of the turbines array in far-field stratification: the results shows that the energy extraction in the Pentland Firth influences bottom temperature more than superficial temperature, producing a larger decrease in the bottom temperature than the increase in superficial temperature. Moreover, they showed that the turbine farm can produce remarkable far-field variations on tidal elevation. To the best of our knowledge, in the marine field there is no research aimed at studying the influence of marine stratification on wake recover and turbine performance.

Concerning the numerical tools employed for the investigation of the interference

between the flow field and turbines, two methodologies are mainly used: RANS and LES techniques. RANS solves the mean flow field, it is definitely computationally less expensive compared to LES, but on the other hand the disadvantage consists in less accuracy in the results. Whereas LES allows a detailed analysis of the flow field and the transient effects may be captured, making LES one of the most promising methodology for simulating turbulent flows [14] [15]. A distinction should be done if we consider the wind or the marine field, since the first is more investigated, both RANS and LES studies has been widely carried out, in particular LES studies have been performed for wind farm simulations [16][17]. Moreover LES validation studies have been carried out [18][19] proving the capability of the model in capture the main characteristics of the flow in presence of turbines. Conversely in the marine field, most of the numerical studies have been performed by means of RANS [3][20], and only a few studies concern LES methodology [5].

The aim of this research is to provide an insight on the interaction between the turbine and stable stratification, in particular evaluating the effects that marine stratification entails on turbine power performance, wake behavior and velocity deficit recover. It is of great importance to establish whether stratification might bring changes in the field of a turbine, especially as regards the design of tidal farms. For these reasons, the present study can provide a first step in the comprehension of the effects of stratification. Moreover the influence of turbine mixing on stratification will be also evaluated. The numerical investigation is performed by means of the in-house LES-COAST (IE-FLUIDS research group) model coupled with a turbine module which computes the turbine induced forces. The LES-COAST model solves the filtered Boussinesq form of the unsteady three-dimensional Navier-Stokes equations and the two transport equations for temperature and salinity [21]. By means of LES technique the large scales of motion are solved directly, whereas the smallest scales are modeled using a sub-grid scale model [22]. The dissertation is organized as follows. First the turbine module and the LES-COAST model are introduced, then we show the validation of the model carried out comparing the experimental data supplied by literature with the numerical results. After validation, the results of a simulation in absence of stratification is illustrated and it will be useful for a subsequent comparison. In order to take into account the effects of stratification, two different levels of stratification are simulated: a weak and a strong stable stratified condition. The results of the two cases are analyzed and finally a summary and conclusions are provided.

Chapter 2

Actuator Disc Model

In order to take into account the presence of the turbine into the flow field we decided to take advantage of the Actuator Disk Model [23], [24], herein after called ADM. As mentioned into the introduction section, the advancement in the marine energy research is nowadays still trailing the more investigated field of wind energy technology. The employment of the ADM method for modeling the turbine induced forces is widely used in both sectors, however if we consider the variety of the investigations and also from a quantitative point of view, the methodology has been applied and tested more extensively in the wind field. In the wind turbine field, numerical studies based on LES coupled with the ADM have been performed, in particular wind farm simulations [25][26]. Moreover validation studies [18][19][27][28], highlights that employing LES coupled with the ADM, allows to reproduce accurately the spatial distribution of the main turbulent statistics like mean velocity, turbulence intensity and turbulent kinetic energy and also supplies detailed information on flow fluctuations and eddies. Another method extensively used for modeling the presence of the turbines is the actuator line method (ALM). Comparison between the ALM and ADM have been carried out, showing that the first method leads to more accurate results in the near field of the wake, however it entails a more expensive computational coast compared to the ADM [19][29]. Also in the marine field RANS investigations has been carried out coupled with the ADM method [30][20][31]. For what concerns the LES methodology only a few studies uses LES as a numerical tool and employ the ALM for modeling the turbine presence [32][5]. The choice of using the ADM as a tool for the current investigation, was made with the intention of addressing our study not only toward the pure research but also to make this instrument of numerical simulation useful for the applied field. In fact, we could have chosen to handle the problem for example by means of resolved geometry or through the actuator line method, but compared to the ADM they are computationally much more expensive, especially for what concerns the resolved geometry approach. The

simulation of a cluster of turbines through the above mentioned methods nowadays is difficult to achieve, due to computational limits. Even if it goes beyond the subject matter of the present work, the study of a multi-array turbines will be one of the future objectives for IE-fluids research group, for these reasons we decided to use the ADM.

Simplifying the function of the turbine module, it works in the following way: physically the presence of the blades gives rise to normal and tangential forces that act in opposition to the flow, these forces are calculated through the ADM and applied to the flow field as body force. There are two versions of the ADM: the ADM without rotation (ADM-NR) and the ADM with rotation (ADM-R). The ADM-NR will be first introduced since is the simpler and quicker among the two two methods. Before going into details about the mathematical model and its physical interpretation, regardless if we consider the ADM-NR or the ADM-R, there are two fundamental coefficients that describe the thrust and the power characteristics of a marine turbine: the thrust coefficient and the power coefficient. The thrust coefficient is the ratio between the trust force that is the force of the water on the turbine and the dynamic force:

$$C_T = \frac{T}{\frac{1}{2}\rho U^2 A} \tag{2.1}$$

The power coefficient is the ratio between the rotor power and the power in the wind:

$$C_P = \frac{P}{\frac{1}{2}\rho U^3 A} \tag{2.2}$$

The power coefficient is a key parameter since it is an esteem of the power that can be extracted.

2.1 Actuator Disk Model without rotation (ADM-NR)

The ADM-NR doesn't take into account the rotation of the wake downstream the rotor. It is based on the one-dimensional momentum theory for which the rotor is ideally substituted by an actuator disk. The analysis is made considering a control volume represented by a stream tube in which the actuator disk creates a jump of pressure into the fluid that flows throughout it, figure 2.1. Before going into details it is worth to list the assumptions that the theory implies:

- the flow is homogenous, incompressible and steady
- there is no frictional drag

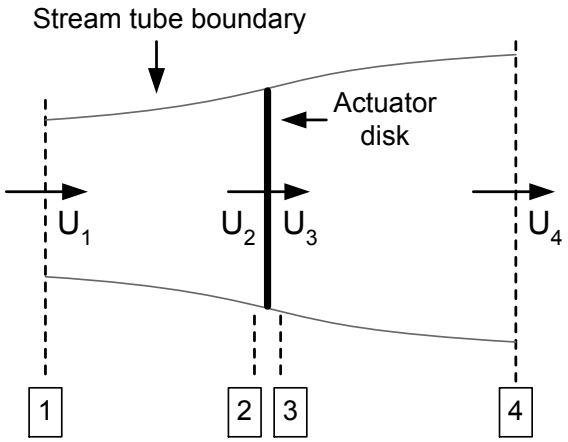

Figure 2.1: Control volume for ADM-NR momentum analysis

- the trust force and velocity are uniform over the disk
- the far upstream static pressure is equal to the far downstream static pressure
- there is no rotation of the wake

Applying the conservation of momentum on the control volume, two expressions for the thrust force are obtained:

$$T = \frac{1}{2}\rho A_2 \left(U_1^2 - U_4^2\right) \tag{2.3}$$

$$T = \dot{m}\left(U_1 - U_4\right) \tag{2.4}$$

Equating (2.3) and (2.4) one obtains:

$$U_2 = \frac{U_1 + U_4}{2} \tag{2.5}$$

It follows that the velocity at the rotor is the average between the unperturbed upstream velocity and far downstream velocity. The axial induction factor is defined as the relative decrease between the far upstream velocity and the velocity at the rotor:

$$a = \frac{U_1 - U_2}{U_1} \tag{2.6}$$

Then:

$$U_2 = U_1(1 - a) \tag{2.7}$$

$$U_4 = U_1(1 - 2a) \tag{2.8}$$

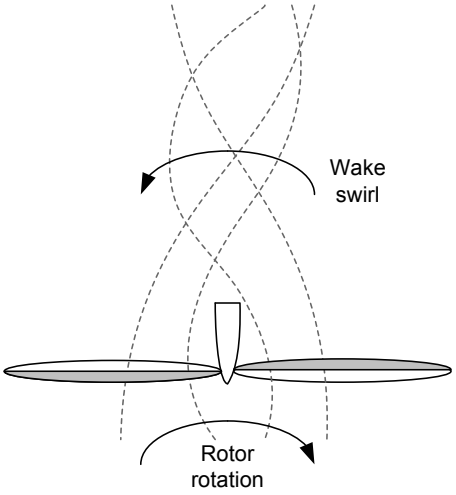

Figure 2.2: Sketch of wake rotation

Combining equations (2.3), (2.7) and (2.8), the thrust results:

$$T = \frac{1}{2}\rho A U_\infty^2 \left[4a(1-a)\right] \tag{2.9}$$

where U_1 is substituted by U_∞. Substituting the thrust (eq. 2.9) in the thrust coefficient relation (eq. 2.1), C_T is equal to:

$$C_T = 4a(1-a) \tag{2.10}$$

That leads to the following expression for a as a function of the thrust coefficient:

$$a = \frac{1}{2}\left(1 - \sqrt{1 - C_T}\right) \tag{2.11}$$

Finally for the actuator disk model without rotation the thrust force can be calculated by means of the following relation:

$$T = F^{ADM-NR} = \frac{\rho}{2} U_\infty^2 C_T A = \frac{\rho}{2} \frac{U_2^2}{(1-a)^2} C_T A \tag{2.12}$$

Where A_2 is substitued by A. The same procedure is applied for the computation of the power:

$$P = P^{ADM-NR} = \frac{\rho}{2} U_\infty^2 C_P A = \frac{\rho}{2} \frac{U_2^3}{(1-a)^2} C_P A \tag{2.13}$$

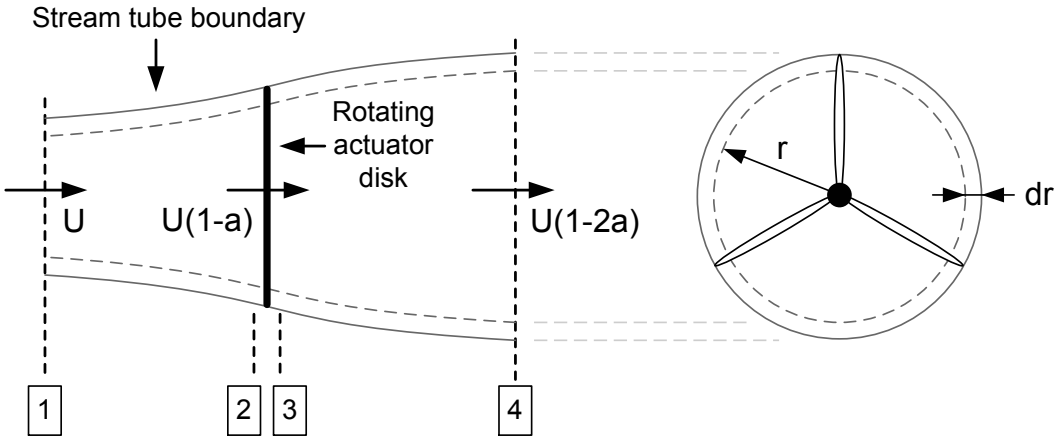

Figure 2.3: Control volume for ADM-R momentum analysis

2.2 Actuator Disk Model with rotation (ADM-R)

In the previous analysis it was assumed that the flow downstream the rotor is not subject to rotation. Since the rotation of the wake causes a reduction of the power coefficient and then of the power that can be extracted, it's important to evaluate such condition. The ADM-R takes into account the wake rotation thanks to the evaluation of the tangential forces, besides as well as the normal forces. Physically the flow downstream the rotor spins in the opposite direction to the rotor rotation as it is depicted in figure 2.2. As logically expected the production of rotational kinetic energy means a loss of energy that can be extracted, that in the case of ADM-NR is not considered.

2.2.1 Blade Element Momentum theory (BEM)

For the ADM-R the method used to compute the turbine induced forces is the BEM theory which merges the momentum theory with the blade element theory. The momentum theory is based on the analysis of forces over a control volume, the relations for the normal and tangential force are calculated through the conservation of linear and angular momentum. Whereas the blade element theory consists in an analysis of forces at blade sections based on the blade section geometric characteristics.

Momentum Theory

For what concerns the one dimensional momentum theory, the analysis can be made using a stream tube with a radius r and annular sections of dr thickness and area equal to $2\pi r dr$, figure 2.3. Across the actuator disk, the normal velocity doesn't

change, however the angular velocity increases from Ω to $\Omega + \omega$, where Ω is the rotor's angular velocity and ω is the angular velocity imparted to the flow. It follows that the thrust force at the annular section is:

$$dT = (p_2 - p_3)dA = \left[\rho\left(\Omega + \frac{1}{2}\omega\right)\omega r^2\right] 2\pi r dr \tag{2.14}$$

Introducing the angular induction factor as:

$$a^{'} = \frac{\omega}{2\Omega} \tag{2.15}$$

the thrust becomes:

$$dT = 4a^{'}(1 + a^{'})\frac{1}{2}\rho\Omega^2 r^2 2\pi r dr \tag{2.16}$$

Another expression for the thrust can be derived using the axial induction factor, a:

$$dT = 4a(1 - a)\rho U^2 r^2 \pi r dr \tag{2.17}$$

Applying the conservation of angular momentum is possible to determine the torque as follows:

$$dQ = 4a^{'}(1 - a)\rho U\Omega r^2 \pi r dr \tag{2.18}$$

Blade Element Theory

For the blade element theory, the blade is divided into N sections or elements, figure 2.4, where forces are calculated based on blade section geometry characteristics and lift and drag features. The lift coefficient is defined as:

$$C_L = \frac{\frac{L}{l}}{\frac{1}{2}\rho U^2 c} \tag{2.19}$$

where L is lift force, l the unit length, c the chord and U is the incoming velocity at the blade element. The drag coefficient is defined as:

$$C_D = \frac{\frac{D}{l}}{\frac{1}{2}\rho U^2 c} \tag{2.20}$$

where D is the drag force. The lift force is perpendicular to the unperturbed upstream flow direction and it is due to the pressure difference between the lower and upper surface of the blade. The drag force is parallel to the unperturbed upstream flow direction and is due to: 1) the friction force at the surface and 2) the pressure difference between the surfaces that are hit by the incoming flow and the surfaces at the opposite side (outgoing flow). The 2D drag and the lift coefficients are usually

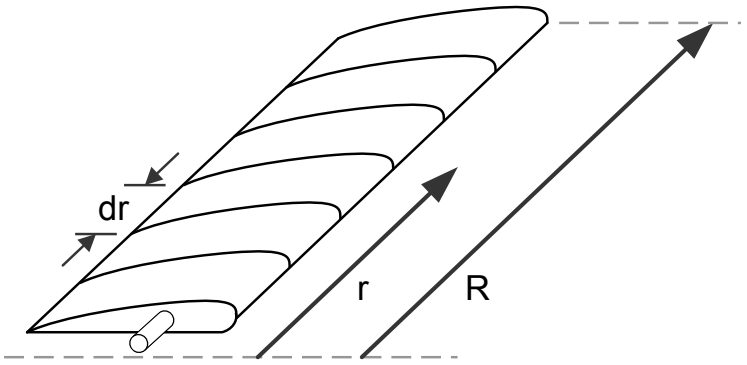

Figure 2.4: Blade element configuration

expressed as a function of the angle of attack for a range of Reynolds number. In figure 2.5 is depicted the blade geometry with the interaction between the incoming flow and forces that act on the blade. The relative velocity is the sum of the flow velocity at the rotor which is $U(1-a)$ and the velocity due to the blade rotation which is $\Omega r(1+\alpha^{'})$, where r is the radius of the element that is the distance between the center of the hub and the blade element. The relative velocity is defined as:

$$U_{rel} = \frac{U(1-a)}{\sin(\varphi)} \tag{2.21}$$

The angle of relative flow φ which is the angle between the rotor plane and U_{rel} can be derived from the following relation:

$$\tan(\varphi) = \frac{U(1-a)}{\Omega r(1+\alpha')} \tag{2.22}$$

Another important geometrical relation that could be determined from figure 2.5 is:

$$\varphi = \theta_p + \alpha \tag{2.23}$$

where θ_p is the pitch angle of the element and α is the angle of attack which is the angle between the relative velocity and the chord line. The drag force is equal to:

$$D = \int_0^R \frac{1}{2}\rho U_{rel}^2 C_D c dr \tag{2.24}$$

where dr is the length of the blade element. The lift force is:

$$L = \int_0^R \frac{1}{2}\rho U_{rel}^2 C_L c dr \tag{2.25}$$

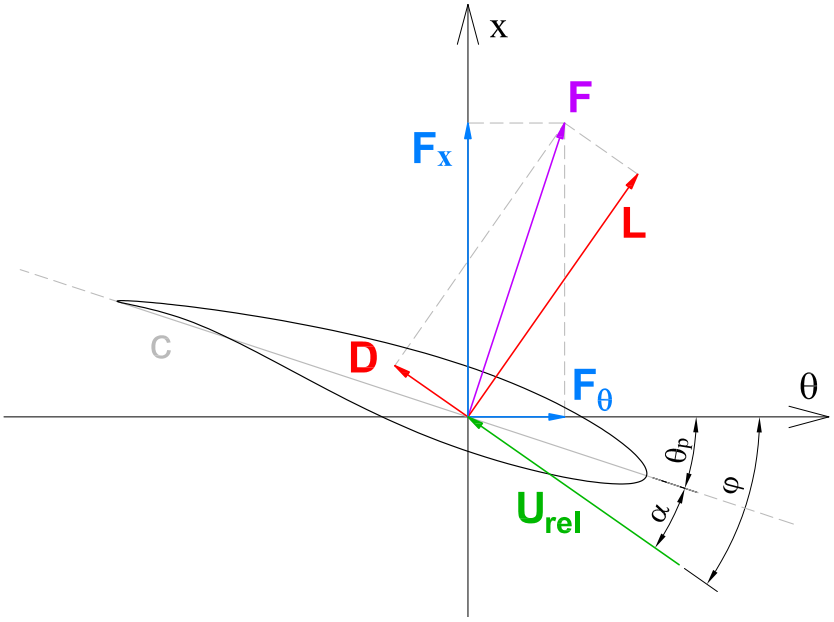

Figure 2.5: Blade section geometry and forces

The normal force is defined as:

$$F_x = L\cos(\varphi) + D\sin(\varphi) \tag{2.26}$$

and the tangential force:

$$F_\theta = L\sin(\varphi) - D\cos(\varphi) \tag{2.27}$$

The blade element analysis leads to the following important result for the normal force written in differential form and for a number of blades equal to B:

$$F_x = \int_0^R B\frac{1}{2}\rho U_{rel}^2 \left[C_L\cos(\varphi) + C_D\sin(\varphi)\right] cdr \tag{2.28}$$

which has been obtained substituting (2.24) and (2.25) into (2.26). The same procedure for the formulation of the differential torque which is obtained from the substitution of (2.24) and (2.25) into (2.27) and multiplied for the radius, leads to:

$$F_\theta = \int_0^R B\frac{1}{2}\rho U_{rel}^2 \left[C_L L\sin(\varphi) - C_D\cos(\varphi)\right] cdr \tag{2.29}$$

Tip Loss Correction

The pressure difference between the two surfaces of a blade causes a circulation around the tip from the lower to the upper surfaces which reduces the lift force. This effect is more intense in presence of fewer and larger blades. For this reason a correction factor must be applied to the momentum equations. The correction factor F based on Prandtl's method is:

$$F = \left(\frac{2}{\pi}\right)\cos^{-1}\left\{\exp\left[-\frac{\left(\frac{B}{2}\right)\left(1-\left(\frac{r}{R}\right)\right)}{\left(\frac{r}{R}\right)\sin(\varphi)}\right]\right\} \tag{2.30}$$

where B is the number of blades and R is the rotor radius. Equations (2.17) and (2.18) respecively becomes:

$$dT = 4Fa(1-a)\rho U^2 r^2 \pi r dr \tag{2.31}$$

$$dQ = 4Fa^{'}(1-a)\rho U\Omega r^2 \pi r dr \tag{2.32}$$

2.2.2 Solution of BEM equations

The classic approach for the solution of BEM equations is to arrange the equations as a function of two variables which are the axial induction factor and the tangential induction factor. The relations for the two induction factors are derived equating the formulas for the thrust and the power of the momentum theory and the blade element theory. Equating the relation (2.28) with the relation (2.31) it can be obtained the axial induction factor:

$$a = \frac{1}{\left\{1+\frac{4F\sin^2(\varphi)}{\sigma'\left[C_L\cos(\varphi)+C_D\sin(\varphi)\right]}\right\}} \tag{2.33}$$

Where the local rotor solidity is defined as $\sigma^{'} = \frac{Bc}{2\pi r}$. The axial induction factor is derived equating the relation (2.29) with the relation (2.32):

$$a^{'} = \frac{1}{\left\{\frac{4F\sin(\varphi)\cos(\varphi)}{\sigma'\left[C_L\sin(\varphi)-C_D\cos(\varphi)\right]}-1\right\}} \tag{2.34}$$

In order to compute the normal and tangential forces induced by the presence of the turbine, the classic approach was first implemented. The method used to find the solution of the axial and tangential induction factors and then compute the normal and tangential forces is a fixed point iteration method. The algorithm realized for

the solution of BEM equation based on the classic approach, it is characterize by an external loop for the convergence of the axial induction factor, preceded by a first loop for the convergence of the tangential induction factor. The fixed point method relates the current solution of the induction factors to the solution at the previous iteration through a function or a coefficient [33] [34]. We tested the algorithm in view of the validation of the model and we found that this approach is not robust in terms of convergence, both for the weakness of the method and also for the fact that there are points of singularities in the solution. Moreover we found that applying the fixed point iteration the errors of convergence can affect the results heavily, in fact the relative errors in the solution of power and thrust coefficients can reach 40%.

In order to solve BEM equations we finally implemented the procedure proposed by Ning [35] [36] which will be illustrated below. The approach indicated by Ning consists in reducing the two variable, two set of equations into one equation problem, namely the residual function. This procedure entails a remarkable advantage since it avoids the resolution of the two nonlinear equations, simplifying the problem. To solve the residual equation that is function of a single variable, it is employed a root finding method allowing the use of a robust method of convergence. Moreover in order to have a guaranteed convergence it's fundamental to bracket a region where to find a zero of residual function that does not contain any singularities in its interior. In fact the turbine operates at different working states that correspond to different regions of the solution. There are mainly three regions: the momentum, the empirical and the propeller brake region. As it is possible to observe from figure 2.6, a point of singularity lies between the empirical and the propeller brake region. The method consists in solving this regions separately in order to keep singularities at the boundaries and so avoiding the convergence issues connected to the presence of points of discontinuity. We can arrange equation (2.22) to have the three variables a, $a^{'}$ and φ related together:

$$\tan(\varphi) = \frac{1-a}{(1+a')\lambda_r} \tag{2.35}$$

This equation can be combined in different forms to get a residual function, but since the aim is to keep singularities at the boundaries, $(1-a)$ and $(1+a)$ should be at the denominator, in this way singularities will be placed at specific locations, that are $\varphi = [0, \pm\pi]$. Through this arrangement, these specific locations split the regions where there is a change in the physic state. In this perspective the residual function becomes the following equation:

$$f(\varphi) = \frac{\sin(\varphi)}{1-a} - \frac{\cos(\varphi)}{(1+a')\lambda_r} = 0 \tag{2.36}$$

This method solves the residual equation for the momentum region, the empirical and the propeller brake region separately This regions are characterized by different

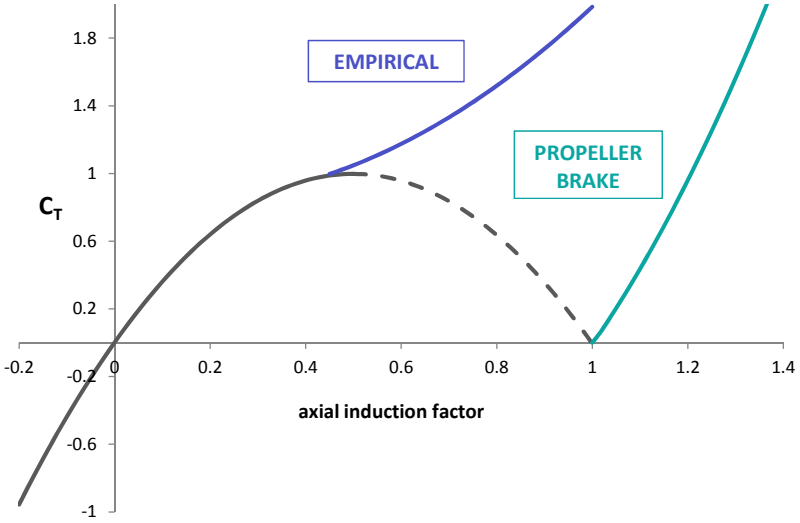

Figure 2.6: Thrust coefficient as a function of the axial induction factor

local thrust coefficient and consequently different axial and tangential induction factors.

The present method, compared to the classic approach above mentioned, overcomes the need to compute the induction factors to update the lift and drag coefficients. The solution of the angle of relative flow is computed through the following steps:

1. define the angle of relative flow
2. compute the angle of attack
3. compute the lift and drag coefficients
4. estimate the normal and tangential force coefficients
5. evaluate the induction factors
6. evaluate the error in the residual function
7. if the error is greater than the tolerance, specify again another angle of relative flow

As concerns the momentum region, the local thrust coefficient from the blade element theory is defined as:

$$C_T = \left(\frac{1-a}{\sin(\varphi)}\right)^2 c_n \sigma' \tag{2.37}$$

where the normal force coefficient is equal to:

$$c_n = C_L \cos(\varphi) + C_D \sin(\varphi) \tag{2.38}$$

For the momentum theory the local thrust coefficient is expressed as:

$$C_T = 4a(1-a)F \tag{2.39}$$

Equating (2.37) and (2.39) and solving for the axial induction factor:

$$a(\varphi) = \frac{k(\varphi)}{1+k(\varphi)} \tag{2.40}$$

where k is a parameter defined as:

$$k(\varphi) = \frac{\sigma' c_n(\varphi)}{4F(\varphi)\sin^2(\varphi)} \tag{2.41}$$

Since the blade element momentum theory is valid up to a maximum value of the axial induction that varies from 0.3 to 0.5, relation (2.40) is valid for $-1 < k \leq \frac{\beta}{(1-\beta)}$ where β is defined as the maximum axial induction factor.

The BEM theory is no longer applicable for axial induction factors between β and 1. In this range an empirical relation for the local thrust coefficient must be employed. Buhl [37] derived the relation between the thrust coefficient and the axial induction factor as follows:

$$C_T = \left(\frac{50}{9} - 4F\right)a^2 - \left(\frac{40}{9} - 4F\right)a + \frac{8}{9} \tag{2.42}$$

Equating (2.37) and (2.42) and arranging the equation to obtain the axial induction factor:

$$a(\varphi) = \frac{\gamma_1 - \sqrt{\gamma_2}}{\gamma_3} \tag{2.43}$$

where γ_1, γ_2 and γ_3 are parameters defined respectively as:

$$\gamma_1 = 2Fk - \left(\frac{10}{9} - F\right) \tag{2.44}$$

$$\gamma_2 = 2Fk - F\left(\frac{4}{3} - F\right) \tag{2.45}$$

$$\gamma_3 = 2Fk - \left(\frac{25}{9} - 2F\right) \tag{2.46}$$

This parametrization is valid for $0.4 < a < 1.0$ and $k \geq \frac{2}{3}$.

Finally the propeller brake region is characterized by induction factors higher than 1, under this condition the formulation of the thrust coefficient is given by the change of sign of the momentum theory:

$$C_T = 4a(a-1)F \tag{2.47}$$

Again equating (2.37) and (2.47) and solving for the axial induction factor:

$$a(\varphi) = \frac{k(\varphi)}{1+k(\varphi)} \tag{2.48}$$

This formulation is applicable only for $k > 1.0$.

As concerns the computation of the tangential induction factor, the same procedure is applied for the torque, in fact equating the torque derived from the blade element theory (eq. 2.29) and the torque derived from the momentum theory (eq. 2.32), and arranging as a function of the tangential induction factor, the following result is obtained:

$$a^{'}(\varphi) = \frac{k^{'}(\varphi)}{1+k^{'}(\varphi)} \tag{2.49}$$

Where $k^{'}$ is a parameter defined as:

$$k^{'}(\varphi) = \frac{\sigma^{'} c_t(\varphi)}{4F(\varphi)\sin(\varphi)\cos(\varphi)} \tag{2.50}$$

where c_t is the tangential force coefficient is defined as:

$$c_t = C_L \sin(\varphi) - C_D \cos(\varphi) \tag{2.51}$$

The relations (2.49) and (2.50) are valid for all of three regions.

Moving from a formulation with two variables to one variable problem, we can use a robust root finding method of convergence. Among the most used root finding techniques, we decided to implement the Brent's method [38] which combines the inverse quadratic interpolation with the bisection method. One of the simplest root finding methods is the bisection method that consists in bisect the interval where it can be found the root of the function and at every iteration select the sub interval that contains the root. Giving an interval [a,b] which contains a zero of the function f, that is $f(\varphi) = 0$, where $\varphi \in$ [a,b] or $f(a) \cdot f(b) < 0$, the midpoint of the interval is $c = (a+b)/2$, then (c,$f(c)$) will substitute (a,$f(a)$) or (b,$f(b)$) for a new bisection of the interval depending on the sign of $f(a)$ and $f(b)$ product (if is negative there is a root of the function inside the interval). Bisection method is a robust method of convergence because it never diverges from the root, at any rate the number of iteration could be very large and could be necessary long time for the

convergence. Instead the inverse quadratic interpolation method is generally much faster especially when it gets close to the solution.

The Brent's algorithm switches between the two methods, using the method that guarantees better performance. It employes a robust method of convergence that is the bisection method together with a faster but a less robust method (which can go outside the bracket), like the inverse quadratic interpolation. In brief the inverse quadratic algorithm follows the steps listed below:

- fit an inverse parabola by means of $f(a)$,$f(b)$,$f(c)$:

$$\begin{aligned}\varphi =& \frac{\big[f(\varphi)-f(b)\big]\big[f(\varphi)-f(c)\big]}{\big[f(a)-f(b)\big]\big[f(a)-f(c)\big]}a + \frac{\big[f(\varphi)-f(a)\big]\big[f(\varphi)-f(c)\big]}{\big[f(b)-f(a)\big]\big[f(b)-f(c)\big]}b \\ &+ \frac{\big[f(\varphi)-f(a)\big]\big[f(\varphi)-f(b)\big]}{\big[f(c)-f(a)\big]\big[f(c)-f(b)\big]}c\end{aligned} \tag{2.52}$$

  where a is the best guess root for the previous iteration $a_j = b_{j-1}$, b is the best guess at the present iteration, c is at the opposite side of b, b and c are the limits of the bracket.

- find the φ point at which the functions is equal to zero $y = 0$
- this point where $y = 0$ becomes b, and the previous value of b becomes a
- if c and b don't bracket a root for the function, then $c = a$

Regardless of the root finding method employed to solve the residual function, a successfully solution can be reached only if the bracket doesn't contain singularities in its interior. To this purpose every region has to be limited by a specific bracket. In this context we can consider two main regions: the momentum plus the empirical range and the propeller brake region.

As concerns the momentum/empirical region, the angle of relative flow inside this range varies from 0 to π. Solutions larger than $\pi/2$ lead to a tangential induction factor equal to -1 which means a reversed tangential flow, that is mathematically possible but occurs rarely. As we saw previously, the momentum theory is valid for $k > -1$, instead for $k < -1$ where there is no solution there are two possibilities: the first is to limit the bracket to $k = -1$, the second chance is to extend the use of the momentum equation also for $k < -1$, which doesn't entail the introduction of artificial solution as it is proved in [35]. The second option, that is to use the momentum equation was chosen to deal with the range where $k < -1$. Finally the bracket for the momentum/empirical region is $[\epsilon, \frac{\pi}{2}]$ where ϵ is equal to 10^{-6}.

Concerning the propeller brake region, angles of relative flow vary from $-\pi$ to 0 , but as for the momentum region we will consider a smaller range where solution could be also physically feasible instead that only mathematically possible. The bracket for the propeller brake region is $[-\frac{\pi}{4}, -\epsilon]$.

Chapter 3

LES-COAST Model

3.1 The governing equations

The LES-COAST model was first developed with the aim of studying close or semi-closed area with complex geometry [21]. Petronio et al. [39] simulated the water renewal and mixing in Muggia Bay and carried out the validation of the model against field data. Galea et al. [40] studied the water mixing and circulation in Barcelona harbour and in Taranto bay. Moreover the study carries out a comparison between the observational data and the results proving that LES-COAST is reliable for coastal modeling. Santo [41] studied the wind-driven circulation and mixing in a alpine lake both in a neutral stratified condition and also in presence of a thermal stable stratification. By means of the LES-WIND (a modified version of LES-COAST for atmospheric applications) Balog [42] simulated a theoretical wind farm parameterizing the turbines through the ADM-NR. In this chapter an overview of the LES-COAST model will be presented.

The Navier-Stokes equations describe and govern the motion of the fluids. For many fluid dynamics problems the Navier-Stokes equations are written under the Boussinesq approximation which allows to simplify the Navier-Stokes equations without losing appreciable accuracy. The Boussinesq approximation assumes that the variation of density $\Delta\rho$ due to fluid fluxes or temperature and/or salinity stratification, is considered small compared to the reference value ρ_0. Since the relative variations of density are usually much less then the relative variations of the velocity field, the density variations can be neglected in the continuity and momentum equation, except for the vertical momentum equation, where the variations of density together with the gravity term give rise to the buoyancy term. Under this approximation the fluid is considered incompressible. By means of LES technique the large scales of motion are solved directly, whereas the smallest scales are modeled using a sub-grid scale model. The splitting of the two scales is carried out by a low-pass

filter which is applied to the variable:

$$\overline{u}(\mathbf{x}) = \int G(\mathbf{x},\mathbf{x}')u(\mathbf{x}')d\mathbf{x}'; \tag{3.1}$$

where $\mathbf{x}$ is the Cartesian coordinate vector, G is the filter function, Δ is the filter width. The top-hat function is used as filter:

$$G(x) = \begin{cases} 1/\Delta & \text{if } |x| < \Delta/2; \\ 0 & \text{otherwise;} \end{cases} \tag{3.2}$$

where the filter cutoff Δ is proportional to the size of grid cells. The filtering procedure decomposes the variable into two components, one is resolved directly and the other one is solved by the SGS model. The filtering splits the scales at high frequencies which are solved directly from the scales at lower frequency. In a cartesian frame of reference, the filtered form of the unsteady three-dimensional Navier-Stokes equations under the Boussinesq approximation and the two transport equations for temperature and salinity are:

$$\frac{\partial \overline{u}_j}{\partial x_j} = 0; \tag{3.3}$$

$$\frac{\partial \overline{u}_i}{\partial t} + \frac{\partial \overline{u}_i \overline{u}_j}{\partial x_j} = -\frac{1}{\rho_0}\frac{\partial \overline{p}}{\partial x_i} + \nu \frac{\partial^2 \overline{u}_i}{\partial x_j \partial x_j} + B_i - \frac{\Delta\rho}{\rho_0} g_i \partial_{i2} - \frac{\partial \tau_{ij}}{\partial x_j}; \tag{3.4}$$

$$\frac{\partial \overline{T}}{\partial t} + \frac{\partial \overline{u}_j \overline{T}}{\partial x_j} = k^T \frac{\partial^2 \overline{T}}{\partial x_j \partial x_j} - \frac{\partial \lambda_j^T}{\partial x_j}; \tag{3.5}$$

$$\frac{\partial \overline{S}}{\partial t} + \frac{\partial \overline{u}_j \overline{S}}{\partial x_j} = k^S \frac{\partial^2 \overline{S}}{\partial x_j \partial x_j} - \frac{\partial \lambda_j^S}{\partial x_j}; \tag{3.6}$$

where u_i is the velocity component in direction i, x_i is the spatial coordinate in direction i, t is time, ρ_0 is the reference density, $\Delta\rho$ is the density anomaly, p is the pressure, ν is the kinematic viscosity, g is the gravity acceleration, τ_{ij} is the SGS stress. Into the equations of transport for temperature and salinity, T is the temperature, S the salinity, k^T and k^S are respectively the coefficients of temperature and salinity diffusion, λ_j^T and λ_j^S are respectively the SGS temperature and salinity fluxes. The equation of state for density completes this set of equations:

$$\frac{\Delta\rho}{\rho_0} = \frac{\rho - \rho_0}{\rho_0} = -\beta^T(T - T_0) + \beta^S(S - S_0); \tag{3.7}$$

The equation 3.7 assumes that the relation between density and temperature/salinity is linear and that the density is independent of pressure.

LES-COAST was first developed with the aim of studying coastal dynamics which are usually characterized by shallow waters, complex geometry and sharp

varying bathymetry. For this reason within the model, equations are transformed in curvilinear coordinates. Equations (3.4)-(3.6) in the curvilinear frame of reference become:

$$\frac{\partial U_m}{\partial \xi_m} = 0; \tag{3.8}$$

$$\frac{\partial J^{-1}\overline{u}_i}{\partial t} + \frac{\partial U_m \overline{u}_i}{\partial \xi_m} = -\frac{1}{\rho_0}\frac{\partial}{\partial \xi_m}\Big(J^{-1}\frac{\partial \xi_m}{\partial x_i}\overline{p}\Big) + \frac{\partial}{\partial \xi_m}\Big(\nu G^{mn}\frac{\partial \overline{u}_i}{\partial \xi_n}\Big) + \\ + B_i J^{-1} - \frac{\overline{\rho}}{\rho_0} J^{-1} g_i \partial_{i2} - J^{-1}\frac{\partial \xi_m}{\partial x_j}\frac{\partial \tau_{ij}}{\partial \xi_m}; \tag{3.9}$$

$$\frac{\partial J^{-1}\overline{T}}{\partial t} + \frac{\partial U_m \overline{T}}{\partial \xi_m} = \frac{\partial}{\partial \xi_m}\Big(k^T G^{mn}\frac{\partial \overline{T}}{\partial \xi_n}\Big) - \frac{\partial \xi_m}{\partial x_j}\frac{\partial \lambda_j^T}{\partial \xi_m}; \tag{3.10}$$

$$\frac{\partial J^{-1}\overline{S}}{\partial t} + \frac{\partial U_m \overline{S}}{\partial \xi_m} = \frac{\partial}{\partial \xi_m}\Big(k^S G^{mn}\frac{\partial \overline{S}}{\partial \xi_n}\Big) - \frac{\partial \xi_m}{\partial x_j}\frac{\partial \lambda_j^S}{\partial \xi_m}; \tag{3.11}$$

where ξ_m, (m = 1,2,3) are the coordinates in transformed computational space $\big(\xi = (x,y,z), \eta = (x,y,z), \zeta = (x,y,z)\big)$, J^{-1} is the inverse of the Jacobian which is the cell volume, U_m is the volumetric flux normal to the surface ξ_m =cost, it is calculated as the product between the contravariant velocity and the inverse of the Jacobian.

$$J^{-1} = \det\Big(\frac{\partial x_i}{\partial \xi_j}\Big); \tag{3.12}$$

$$U_m = J^{-1}\frac{\partial \xi_m}{\partial x_j}\overline{u}_j; \tag{3.13}$$

$$G^{mn} = J^{-1}\frac{\partial \xi_m}{\partial x_j}\frac{\partial \xi_n}{\partial x_j}. \tag{3.14}$$

3.2 Equations set in discretized form

The LES-COAST model employs a non-staggerd grid approach: pressure, Cartesian velocity components and body forces are located at the cell centroid, whereas the controvariant flux at the midpoint of the cell boundary. The equations are integrated using a semi-implicit fractional step method [43] [44], the Adams-Bashforth method is applied for the explicit terms, whereas for the implicit terms is applied the Crank-Nicholson method that allows to overcome the problem of viscous stability limit. The spatial derivatives are discretized using a central second order differences method.

The discretization of equations (3.8)-(3.11) leads to:

$$\frac{\partial U_m}{\partial \xi_m} = 0; \tag{3.15}$$

$$J^{-1}\frac{\overline{u}_i^{n+1}-\overline{u}_i^n}{\Delta t} = \frac{3}{2}\big(C(\overline{u}_i^n)+D_E(\overline{u}_i^n)+B_i^n\big)-\frac{1}{2}\big(C(\overline{u}_i^{n-1})+D_E(\overline{u}_i^{n-1}) +B_i^{n-1}\big)+R_i(\overline{p}^{n+1})+\frac{1}{2}\big(D_I(\overline{u}_i^{n+1})+D_I(\overline{u}_i^n)\big); \tag{3.16}$$

$$J^{-1}\frac{\overline{\lambda}^{n+1}-\overline{\lambda}^n}{\Delta t} = \frac{3}{2}\big(C(\overline{\lambda}^n)+D_E(\overline{\lambda}^n)\big)-\frac{1}{2}\big(C(\overline{\lambda}^{n-1})+D_E(\overline{\lambda}^{n-1})\big) +\frac{1}{2}\big(D_I(\overline{\lambda}^{n+1})+D_I(\overline{\lambda}^n)\big); \tag{3.17}$$

where:

$$C_i = -\frac{\partial}{\partial \xi_m}(U_m u_i); \tag{3.18}$$

$$R_i = -\frac{\partial}{\partial \xi_m}\Big(J^{-1}\frac{\partial \xi_m}{\partial x_i}\Big); \tag{3.19}$$

$$D_I = \frac{\partial}{\partial \xi_m}\Big(\nu G^{mn}\frac{\partial}{\partial \xi_n}\Big) \quad m=n; \tag{3.20}$$

$$D_E = \frac{\partial}{\partial \xi_m}\Big(\nu G^{mn}\frac{\partial}{\partial \xi_n}\Big) \quad m\neq n; \tag{3.21}$$

$\partial/\partial\xi_m$ are the finite difference operators in the computational space, the superscripts represent the time steps, C defines the convective terms, D_E and D_I are respectively, the off-diagonal viscous terms treated explicitly, and the diagonal viscous terms treated implicitly, B_i is the body force, R_i is the discrete operator for the pressure gradient terms, λ are the scalars (temperature or salinity).

3.3 Fractional step method

The equations (3.15)-(3.17) are solved using the fractional step method [43] [44], which is a procedure that consists in two steps: the predictor and the corrector. The corrector step solves the equations for an intermediate velocity u_i^* which satisfies advective and diffusive transport and body force processes:

$$\Big(I-\frac{\Delta t}{2J^{-1}}D_I\Big)(u_i^*-u_i^n) = \frac{\Delta t}{J^{-1}}\Big[\frac{3}{2}\big(C(\overline{u}_i^n)+D_E(\overline{u}_i^n)+B_i^n\big) -\frac{1}{2}\big(C(\overline{u}_i^{n-1})+D_E(\overline{u}_i^{n-1})+B_i^{n-1}\big)+D_I(u_i^n)\Big]; \tag{3.22}$$

where I is the identity matrix. To invert the matrix D_I, the approximate factorization method is applied and equation (3.22) becomes:

$$\Big(I-\frac{\Delta t}{2J^{-1}}D_1\Big)\Big(I-\frac{\Delta t}{2J^{-1}}D_2\Big)\Big(I-\frac{\Delta t}{2J^{-1}}D_3\Big)(u_i^*-u_i^n)=\frac{\Delta t}{J^{-1}}\Big[\frac{3}{2}\big(C(\overline{u}_i^n) +D_E(\overline{u}_i^n)+B_i^n\big)-\frac{1}{2}\big(C(\overline{u}_i^{n-1})+D_E(\overline{u}_i^{n-1})+B_i^{n-1}\big)+D_I(u_i^n)\Big]; \quad (3.23)$$

where:

$$D_k=\frac{\partial}{\partial\xi_k}\Big(\nu G^{kk}\frac{\partial}{\partial\xi_k}\Big) \quad k=1,2,3. \quad (3.24)$$

The corrector step computes the velocity u_i^{n+1} which satisfies the continuity equation, from the intermediate velocity u_i^*. Both velocities are related to the pressure gradient by:

$$u_i^{n+1}-u_i^*=\frac{\Delta t}{J^{-1}}[R_i(\phi^{n+1})]; \quad (3.25)$$

where:

$$R_i(p)=\Big(J^{-1}-\frac{\Delta t}{2}D_I\Big)\Big(\frac{R_i(\phi)}{J^{-1}}\Big). \quad (3.26)$$

By interpolating the relation (3.25) on the cell face we obtain:

$$U_m^{n+1}=U_m^*-\Delta t\Big(G^{mn}\frac{\partial\phi^{n+1}}{\partial\xi_n}\Big); \quad (3.27)$$

where U_m^* is the intermediate volume flux defined as: $U_m^{n+1}=J^{-1}\left(\partial\xi_m/\partial x_j\right)u_j^*$. Substituing equation (3.27) into the continuity equation, we obtain the Poisson equation for the pressure ϕ^{n+1}:

$$\frac{\partial}{\partial\xi_n}\Big(G^{mn}\frac{\partial\phi^{n+1}}{\partial\xi_n}\Big)=\frac{1}{\Delta t}\frac{\partial U_m^*}{\partial\xi_n} \quad (3.28)$$

The Poisson equation is solved using a SOR iterative technique combined with a multigrid method.

3.4 Subgrid scale model

As mentioned above, the LES technique is based on the resolution of the large scales, whereas small scales are parametrized through a sub-grid scale model. The filtering of Navier-Stokes equations, in particular the filtering of the non linear term gives rise to the residual stress tensor:

$$\tau_{ij}^R=\overline{u_iu_j}-\bar{u}_i\bar{u}_j \quad (3.29)$$

The residual tensor can be considered as the sum of an isotropic and an anisotropic term:

$$\tau_{ij}^{R} = \tau_{ij}^{SGS} + \frac{1}{3}\tau_{kk}^{R}\delta_{ij} \tag{3.30}$$

The isotropic term or deviatoric part of the stress tensor, is added to the filtered pressure which becomes the modified kinematic pressure:

$$\overline{P} = \overline{p} + \frac{1}{3}\tau_{kk}^{R}\delta_{ij} \tag{3.31}$$

The deviatoric part is usually modeled by means of eddy-viscosity models which approximate the SGS processes by analogy with the effects of molecular viscosity. The eddy viscosity models relate the deviatoric part to the resolved strain rate tensor S_{ij} through a SGS eddy viscosity:

$$\tau_{ij}^{SGS} = -2\nu_{SGS}\overline{S}_{ij} = -\nu_{SGS}\Big(\frac{\partial\overline{u}_i}{\partial x_j} + \frac{\partial\overline{u}_j}{\partial x_i}\Big) \tag{3.32}$$

The eddy viscosity is modeled throught the Smagorinsky [22] approach, by which the eddy viscosity is the product between a lengh scale l_{nr} and a velocity scale ν_{nr} related to the unresolved scales of motion. Through the Smagorinski model the eddy viscosity is the following:

$$\nu_t = l_{nr} \cdot \nu_{nr} = C^2\Delta^2\left|\overline{S_{ij}}\right| \tag{3.33}$$

where C is the Smagorinsky coefficient, Δ is a characteristic lengh scale proportional to the cell dimension and $\left|\overline{S_{ij}}\right|$ is the contraction of resolved strain rate tensor.

3.5 Boundary conditions on solid walls

The direct solution of the viscous sub-layer of the boundary layer becomes unfeasible at hight reynold number because of the expensive computational costs [45]. In order to model the solid boundaries a wall function is used to skip the direct solution of the viscous sub-layer. In the inner layer a logaritmic profile for the velocity can be defined as:

$$v^{+} = \frac{1}{\kappa}logy^{+} + B \tag{3.34}$$

where v^{+} is the non-dimensional tangential velocity scaled with the friction velocity $u_\tau = \sqrt{\tau_w/\rho}$, where τ_w is the shear stress at the wall. The wall normal coordinate is $y^{+} = y/l_\tau$, with $l_\tau = \nu/u_\tau$. The von Karman constant κ is 0.41, while B is equal to 5.1. The classical approach requires that the centroid of the first cell lies within the logaritmic layer, then the wall shear stress τ_w is computed using equation (3.34).

3.6 Turbine induced forces

The turbine induced forces computed by the turbine module are applied to the flow field as a body force (B in the previous governing equations). In order to obtain a smooth solution and to avoid problems of singularities and numerical instabilities the turbine induced forces are distributed using a Gaussian approach [23] [27]. So far we applied the Gaussian distribution in the streamwise direction. The Gaussian approach consists in taking the convolution of the local force $\mathtt{f}$ and a regularization kernel η_ϵ as:

$$\mathtt{f}^\epsilon = \mathtt{f} \otimes \eta_\epsilon \tag{3.35}$$

where:

$$\eta_\epsilon = \frac{1}{\epsilon^3 \pi^{3/2}} \exp\left[-\frac{d^2}{\epsilon^2}\right] \tag{3.36}$$

where d is the distance between grid points and the blade elements, ϵ is a constant parameter that adjusts the distribution of the regularized load; the value that has been chosen for ϵ is proportional to the dimensions of the grid cells.

Chapter 4

Turbine Module Validation

The turbine module computes the normal and tangential forces induced by the presence of the turbine through the ADM-R model. Within the turbine module, besides the ADM-R it is also implemented the ADM-NR. As we said in chapter 2, the ADM-NR doesn't take into account the rotation of the wake and computes only the normal force. At the end of the chapter there will a comparison between the results obtained from the two models, whereas the validation of the ADM-R will be illustrated in the next sections.

The ADM-R is based on the BEM equations; in order to solve the BEM's equations and compute the turbine induced forces, it is necessary to implement an iterative method. In order to avoid the well known BEM's equation convergence issue we followed the procedure proposed by Ning [35]. The ADM-R model was implemented and integrated into the LES-COAST model environment. In this chapter experimental data of Bahaj et al. [46] [47] have been used with the purpose of evaluating the capability of the model in reproducing the thrust and power characteristics of a turbine. This goal has been achieved first simulating numerically the experimental case and then comparing the numerical results with the experimental data. The large collection of data supplied in the above mentioned paper gave us the possibility to validate the model in particular against the blade pitch angle. In the first section there will be a description of the data available from the Bahaj study, then the numerical setup will be presented and finally the comparison between the experimental data and the numerical results will be shown and discussed.

4.1 Experimental data

In order to evaluate the reliability of the ADM-R implementation coupled with the LES-COAST model, experimental data of Bahaj et al. [46] [47] have been used to

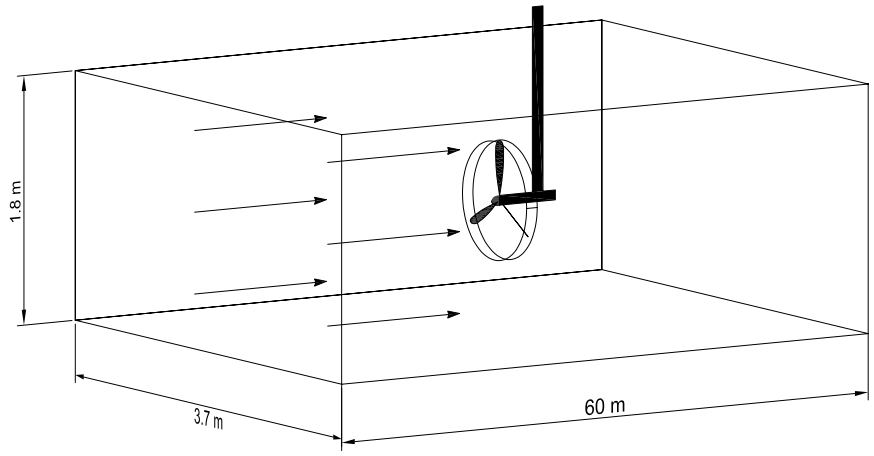

Figure 4.1: Sketch of the experimental towing tank

validate the model. In the tests carried out in the Southampton laboratory towing tank, a three-blade horizontal axis turbine of $D = 0.8$ m diameter was employed. The towing tank has a free surface on the top and the turbine blades are completely immersed into the fluid, in particular two types of tip immersion have been adopted: a shallow tip immersion of $0.19D$ and a deep tip immersion of $0.55D$. The dimensions of the towing tank, which measures 60 m in length, 3.7 m in width and with a depth of 1.8 m, are shown in figure 4.1.

The blade shape and geometric characteristics were developed from the interpolation of the airfoil shape of NACA 63-812, 63-815, 63-818, 63-821 and 63-821 for 17 sections along the blade. Radius, chord, pitch angle and thickness, the geometric characteristics of the 17 blade sections, are shown in table 4.1. In the experimental study of Bahaj et al., measurements of thrust and power characteristics have been collected for different types of flow conditions and blade settings. The wide set of measurements reported in the study provide the thrust and the power coefficient as a function of *tip speed ratio* (TSR). The employed TSR range is not fixed, the upper and the lower bands of TSR change based on the experimental setup conditions. In the experimental tests the range of TSR was obtained varying the rotor angular velocity, and at the same time keeping constant the inflow velocity. The variation of the rotor angular velocity was achieved applying a variable load on the rheostat. The tests were carried out in order to study the influence of pitch angle, yaw angle, tunnel velocities and tip immersion depth on power and thrust characteristics of the

Element No.	**Radius** [mm]	**c/R** [-]	**Pitch** [deg]	**t/c** [%]
1	80	0.1250	15.0	24.0
2	100	0.1203	12.1	22.5
3	120	0.1156	9.5	20.7
4	140	0.1109	7.6	19.5
5	160	0.1063	6.1	18.7
6	180	0.1016	4.9	18.1
7	200	0.0969	3.9	17.6
8	220	0.0922	3.1	17.1
9	240	0.0875	2.4	16.6
10	260	0.0828	1.9	16.1
11	280	0.0781	1.5	15.6
12	300	0.0734	1.2	15.1
13	320	0.0688	0.9	14.6
14	340	0.0641	0.6	14.1
15	360	0.0594	0.4	13.6
16	380	0.0547	0.2	13.1
17	400	0.0500	0.0	12.6

Table 4.1: Section blade characteristics: from left to right the columns respectively refer to the number of element, the element radius, c is the chord divided by R that is the rotor radius, the pitch section angle and finally t is the element thickness divided by the chord.

turbine as a function of TSR. As regards the towing tank, power and the thrust coefficients were computed from the measurements performed under the following test conditions:

- pitch angle of 20 degrees with a velocity of 1.5 m/s, zero yaw angle and a shallow and a deep tip immersion
- pitch angle of 25 degrees with a velocity of 1.4 m/s for the deep tip immersion and a velocity of 1.2 m/s for the shallow tip immersion, at zero yaw angle
- pitch angle of 20 degrees with a velocity of 1.4 m/s for four different yaw angles: 0°, 15°, 22.5°, 30°
- pitch angle of 25 degrees with a velocity of 1.4 m/s for four different yaw angles: 0°, 15°, 22.5°, 30°

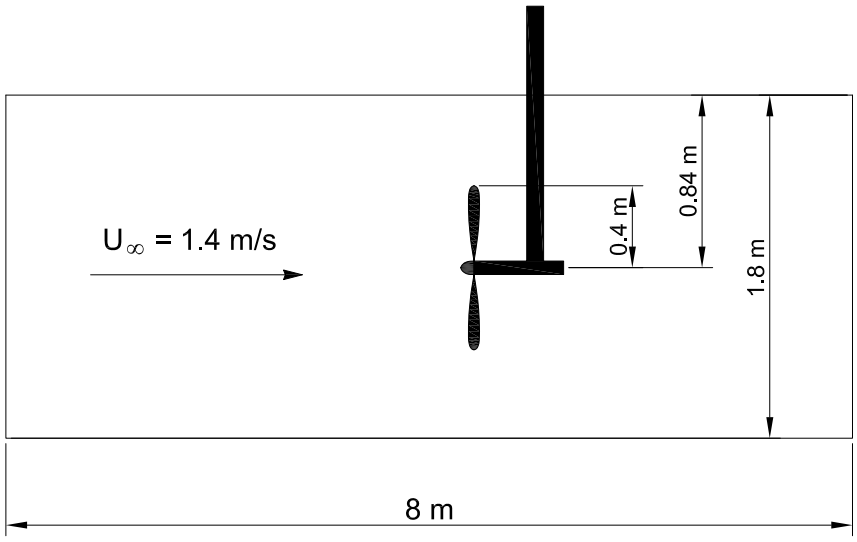

Figure 4.2: Vertical section of the domain of simulation

4.2 Numerical simulation characteristics

LES coupled with ADM-R have been performed with the aim of reproducing numerically the experimental data. The experimental setup has been recreated numerically with the domain and flow characteristics illustrated below. First of all, the domain of the simulation was reduced compared to the experimental domain as concerns the length in the streamwise direction. This choice has been made since we wanted to limit the number of grid cells and maintain approximately equal the dimensions of the cell for the three spatial directions. The domain of the simulation measures L=8 m in the streamwise direction x, W=3.7 m in the spanwise direction z and H=1.8 m in the vertical direction y.

The computational grid is uniform and the number of the grid cells are N_x=64, N_y=32 and N_z=64 respectively for the streamwise, spanwise and vertical direction. The grid resolution has been defined based on the studies of Wu and Porté-Agel [19] and Abkar and Porté-Agel [11]. Wu and Porté-Agel investigated the characteristics of a wake behind a wind turbine using LES coupled with the ADM-R. They compared the streamwise velocity and the turbulence intensity results with the high-resolution wind tunnel measurements obtained in the wake of a miniature wind turbine. The comparison is made for four different grid resolutions and it highlights that the model shows small sensitivity to grid resolution, both in the near

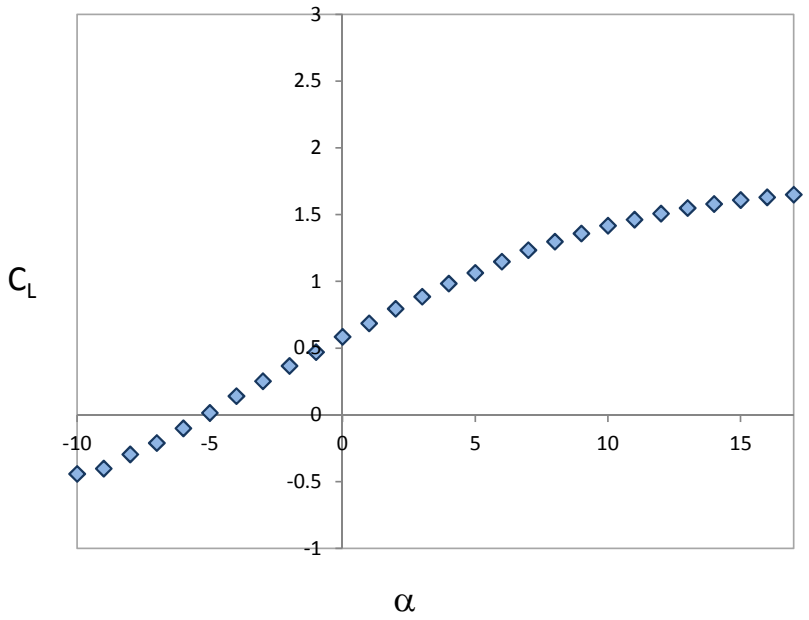

Figure 4.3: Lift coefficient as a function of the angle of attack

and far wake. In particular in the far wake region the results are nearly identical using the four resolutions, whereas in the near wake the results start to underestimate values when the number of cells within the rotor are around 7 both in the spanwise and vertical direction. The study highlights that there is very little grid resolution dependence when the number of cells inside the rotor are at least eight in spanwise and vertical direction. Abkar and Porté-Agel studied the influence of three atmospheric conditions on wake development and behavior of a wind turbine. They tested two grid resolutions and they found that the results are subject to little grid sensitivity between the coarse grid of 10 and 5 cells and the finest grid of 16 and 8 cells that cover the rotor area, respectively for the vertical and spanwise direction. Fernandez [31] performed a numerical simulation of the wakes behind 5 marine turbines. The numerical results were compared to the experimental data for three different grid resolutions. The resolution study carried out by Fernandez indicates that a grid independence is observed when the number of points per turbine diameter are equal or more than 48. In this perspective and in order to avoid problems of grid sensitivity, we set the number of grid cells within the rotor area to 14 and 13, respectively for the vertical and spanwise direction. The free stream velocity at the rotor hub height is equal to $U_\infty = 1.4$ m/s, consequently the Reynolds number based on the rotor diameter can be expressed as:

$$Re_D = \frac{U_\infty \cdot D}{v} = \frac{1.4 \cdot 0.8}{10^{-6}} = 1.12 \cdot 10^6 \tag{4.1}$$

The blade tip immersion is set to 0.55D and the rotor is placed at center of the transversal section (in the spanwise direction) and at the coordinate x_{rot}=3.2 in the streamwise direction. Figure 4.2 shows a sketch of the domain of simulation with the turbine for a vertical section. As regards the boundary conditions, we consider the presence of solid walls at the bottom of the domain as well as at the lateral walls. Here a wall-layer model is considered to skip the solution of the near-wall part of the boundary layer.

A stress-free condition is applied at the free surface. The inflow was obtained from a previous simulation, over the same domain but imposing periodicity along the streamwise direction and collecting dataset at a fixed transversal plane, moreover in the streamwise direction the flow was driven by a constant pressure gradient $dp/dx = 2.252 \cdot 10^{-6}\ m/s^2$. Concerning the blade settings, the blade pitch angle is set to 25 degrees with a zero yaw angle. The computation of normal and tangential forces requires the knowledge of the lift drag coefficients. The 2D lift and drag coefficients are function of the angle of attack and the Reynolds number. In the present study we use the data supplied by Bahaj et al. for the computation of the lift and drag coefficients. In their study they provide the two coefficients for all of five NACA 63-8xx airfoil shapes. The computation has been made by means of XFOIL, a software for the design and the analysis of airfoils. Specifying the geometric characteristics of the airfoil section and the Reynolds number, XFOIL computes the lift and drag coefficient as a function of the angle of attack. As regards the lift and

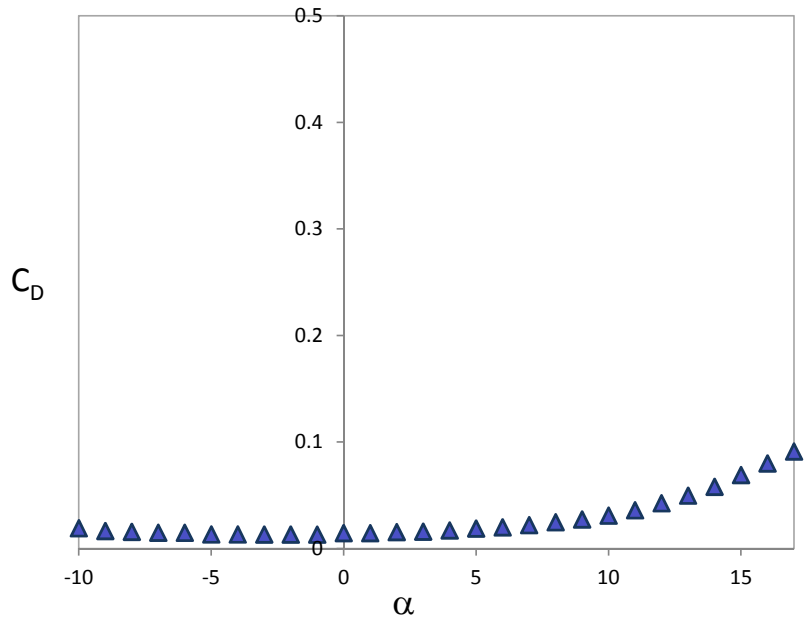

Figure 4.4: Drag coefficient as a function of the angle of attack

drag coefficients, figures 4.3 and 4.4, which have been used in the present study, they have been derived from the interpolation of the curves supplied in the Bahaj el al. investigation.

4.3 Comparison between the experimental data and numerical results

Based on the above mentioned characteristics of the domain and blade settings, LESs were performed coupled with the ADM-R model in order to test the module capability in reproducing the experimental measurements in terms of extracted power and the entity of loads that the turbine is subject to. The key parameters that have been compared with the experimental data are the power coefficient and the thrust coefficient. The evaluation of the two coefficients have been done for a

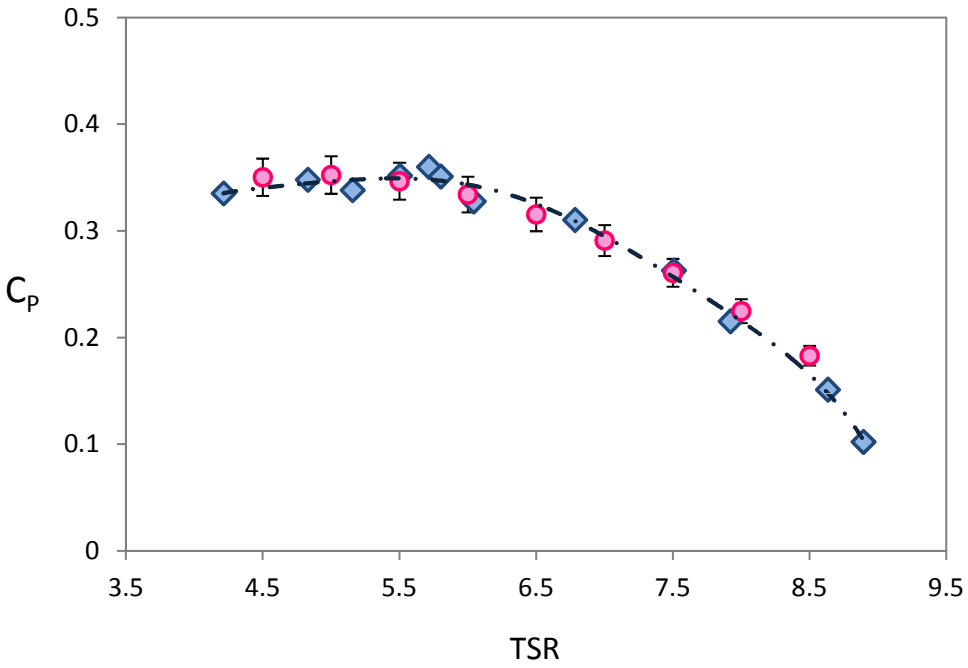

Figure 4.5: Power coefficient as a function of tip speed ratio. Comparison between experimental data (blue diamond) and numerical results (red circles), error bars of 5%

range of tip speed ratios that varies from 4.5 to 8.5. Figure 4.5 shows the comparison between the experimental data and the simulation results of the power coefficient as a function of tip speed ratio. The figure 4.5 shows that there is a good agreement

between the experimental data and the results for the esteem of the power that can be extracted, except for hight values of TSR. Figure 4.6 shows the comparison between the measured thrust coefficient and the numerical results. Figure 4.6 indicates that the thrust coefficient is a bit underestimated except for high values of TSR. Nevertheless the maximum relative error is below 5%. The underestimation of the thrust coefficient might be ascribed to the fact that in our simulation we do not consider the generation of surface waves, which might have been present in the laboratory experiments. However, this aspect needs further investigation.

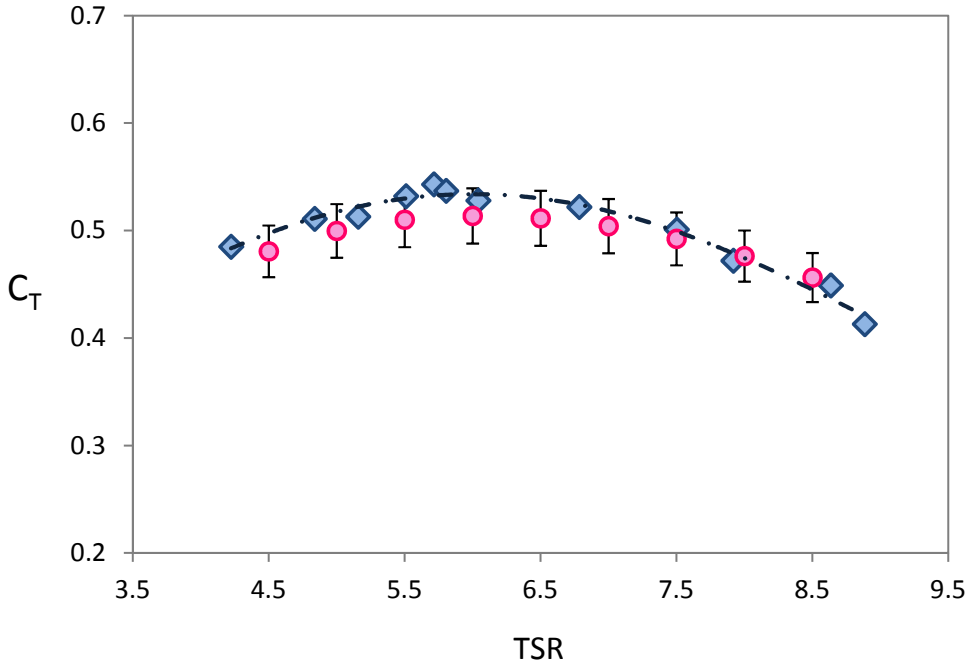

Figure 4.6: Thrust coefficient as a function of tip speed ratio. Comparison between experimental data (blue diamond) and numerical, e results (red circles), error bars of 5%

4.4 Comparison between ADM-R and ADM-NR for wake modeling

In the previous section the ADM-R module was validated against experimental data. The comparison between the experimental data and the numerical results shows the capability of the ADM-R model in reproducing the thrust and power coefficients of

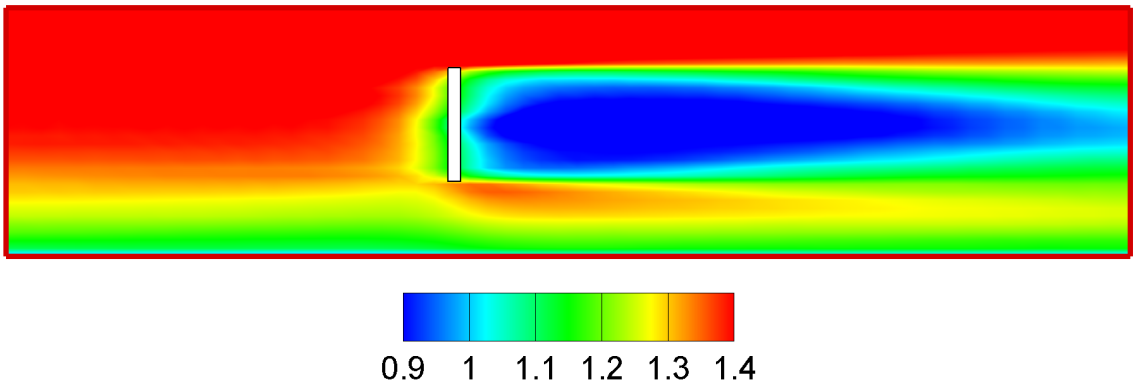

Figure 4.7: ADM-R model - contour plot of time averaged streamwise velocity U [m/s] for a vertical plane (x-y), across the turbine center. The white rectangle represent the turbine rotor.

a turbine. Besides the evaluation of the loads that act on the turbine and the energy production, another important characteristic that is fundamental to take into consideration is the wake, produced by the interference of the turbine over the flow field. In this section the results of the modeling of the rotor's wake will be shown. A comparison between the wake modeled by the ADM-R and the wake modeled by the ADM-NR will be analyzed. The presence of the turbine influences the flow field since the extraction of energy causes a reduction of velocity downstream the rotor. The wake region is also affected by characteristic phenomena like the increasing level of turbulence, the rotation of the wake and pressure difference. Downstream the rotor there is a spreading of the wake which moving downwards recovers to the free stream conditions. The expansion of the wake is influenced by the ambient turbulence, the turbine induced turbulence, the stream velocity, and the distance where the wake hits the ground, and as we will see in chapter 5 by marine stratification conditions. The wake is usually considered split into two parts: the near and the far wake. The near wake is characterized by a remarkable decrease of velocities and high levels of shear and pressure gradients and turbulence intensity. The turbulent intensity moving downward tends to decrease and the velocity deficit progressively recovers. The velocity deficit in the near wake is remarkably influenced by the momentum jump across the rotor. As concerns the far wake, it is characterize by a turbulent mixing between the wake and the surrounding flow field. This mechanism is mainly responsible for the dissipation of the wake that gradually expands moving downstream, where the edges of the wake are entrained into the surrounding field. Modeling accurately the wake and its recover is particularly significant for turbines farms. If the wake of an upstream turbine affects remarkably the field of a subsequent turbine, the global production decreases. A solution could be to distance enough the spacing between upstream and downstream turbines, however some practical restrictions like

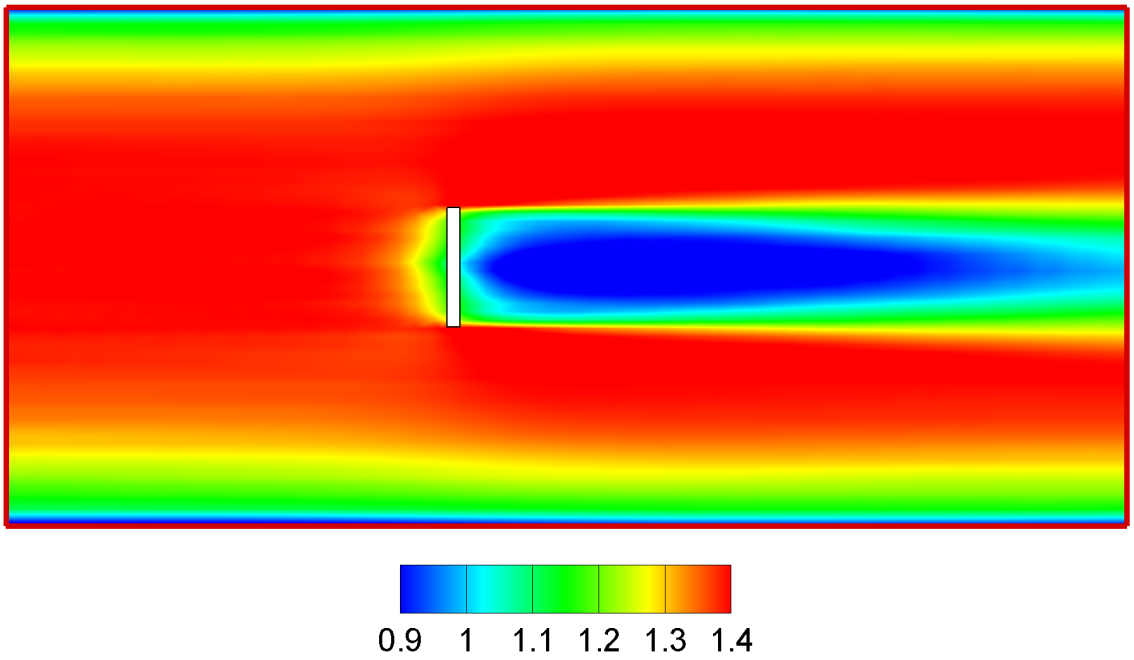

Figure 4.8: ADM-R model - contour plot of time averaged streamwise velocity U [m/s] for a horizontal plane (x-z), across the turbine center.

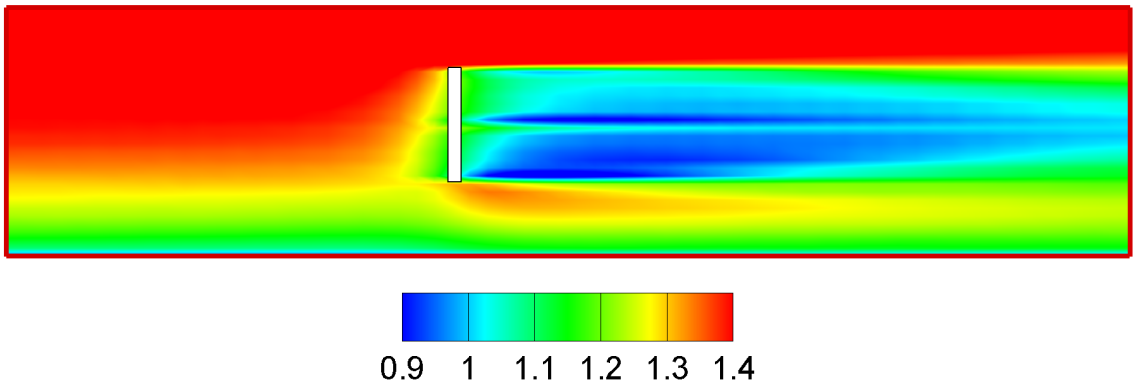

Figure 4.9: ADM-NR model - contour plot of time averaged streamwise velocity U [m/s] for a vertical plane (x-y), across the turbine center.

cabling costs and overall site limitation space makes it unfeasible. Moreover, within a farm site, more turbines are installed and more energy can be extracted. In this perspective a compromise between the spacing and the number of turbines has to be find in order to reach the maximum global efficiency of the farm. For these reasons it's important to predict accurately the development of the wake and its recover.

Within the ADM model, we can choose to employ the ADM-R or the ADM-NR

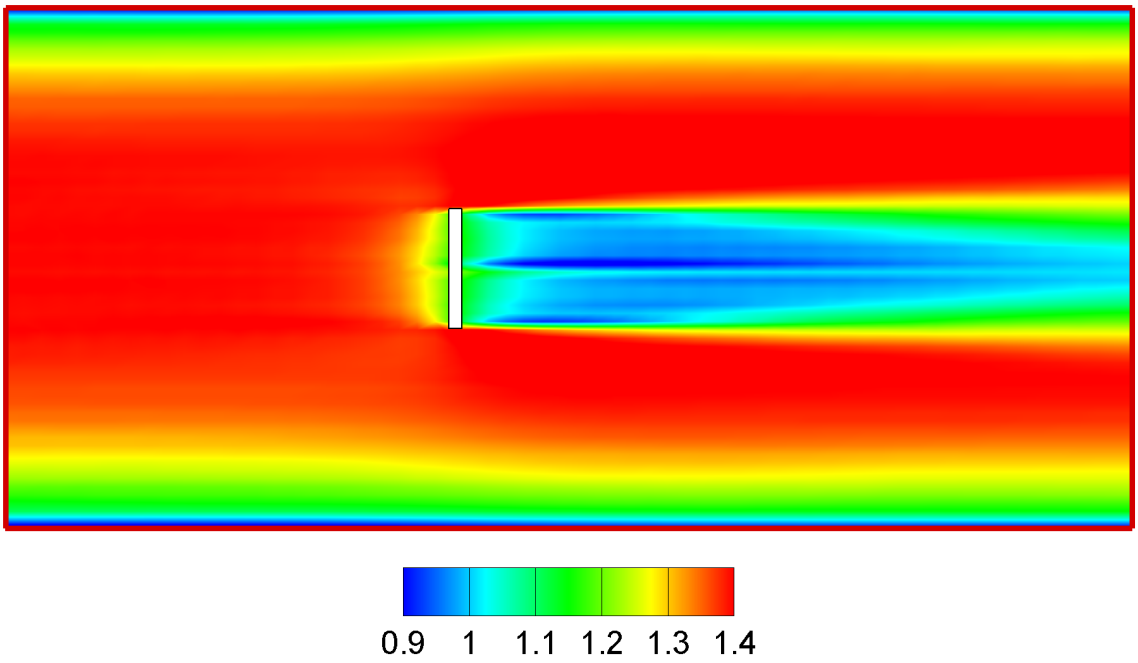

Figure 4.10: ADM-NR model - contour plot of time averaged streamwise velocity U [m/s] for an horizontal plane (x-z), across the turbine center.

to simulate the presence of the turbine and model the wake. For the ADM-NR the advantage consists in the simple theory and consequently the implementation becomes straightforward. The drawback lies in the need to specify the thrust coefficient to determine the normal force that in this case is distributed uniformly over the rotor cells. Concerning the ADM-R, aside a more complex implementation, problems of convergence for the solution of BEM equation (as we saw in section 2.2.2) can arise, moreover forces must be distributed appropriately to obtain smooth results. These characteristics make the ADM-R more demanding compared to the ADM-NR. In this section we are going to compare the results in terms of mean velocity field between the two models. The simulation concerns the data of the experimental case that have been used for the validation of ADM-R for the thrust and power coefficient. In the case of the ADM-NR tabulated values for the thrust coefficient expressed as a function of the velocity magnitude have been employed. LES coupled with the ADM-R based on the characteristic mentioned in section 4.2 has been performed. The non-dimensional lapse of time of the simulation is $t = 80.25$, long enough to reach a steady state condition, and to obtain convergent statistics.

The results in terms of streamwise mean velocity averaged in time are showed in figures 4.7 and 4.8. As it was expected, looking at figures 4.7 and 4.8 a wake forms downstream the rotor as a result of the energy extraction. The streamwise

velocity deficit is larger closer to the rotor and it is subject to a decrease as the wake moves downwards expanding and entraining the surrounding flow. Figures 4.9 and 4.10 show the streamwise mean velocity, averaged in time, for the ADM-NR model respectively for a vertical and horizontal plane. As for the ADM-R a wake forms beyond the rotor which tends to recover downstream. Comparing the wake shape between the two models, it's evident that in the case of the ADM-R the wake has an approximately symmetric behavior. This result is more consistent to the measurements data [6] [48]. For a qualitative analysis of the wake modeling between the two models we refer to the study of Wu and Porté-Agel [19]. As reported in [19], the ADM-NR it's not able to reproduce accurately the mean velocity field in the wake of a rotor. The study points out that the discrepancy between the measurements and the results occurs in the near wake, in particular the mean velocity within this region is over predicted at the center of the wake. Instead there is a good agreement between the mean streamwise velocities measured and the results of ADM-NR in the far region of the wake. This lack of capability of the ADM-NR in reproducing the experimental data is due in particular to the assumptions that are at the basis of the ADM-NR theory. The first assumption is that the wake rotation is not taken into account, then the tangential forces induced by the presence of the turbine are not computed. The second assumption is that the normal force is distributed uniformly over the rotor area. This last simplification is the main reason because the ADM-NR it is not able to reproduce the wake as accurately as the ADM-R.

Considering the above analysis, the ADM-R will be employ as the tool for the subsequent investigation, since it has been demonstrated its capability to reproduce thrust and power characteristics and moreover it is able to model accurately the characteristics of the rotor's wake.

Chapter 5

Results

5.1 Stable stratification

Stable stratification is ubiquitous of the marine environment, associated to vertical gradient of either salinity or temperature along the water column. Stable stratification produces variation along the vertical direction of the horizontal velocity profile and turbulent kinetic energy. Moreover where density gradient is sharp, for example at the interface between two layers with different densities, the development of internal waves transfers energy in the vertical direction. Since the presence of marine stratification entails an effect on the flow field, it is important to assess the influence of stratification on the turbine efficiency and on rotor wake. The esteem of wake extent is particularly significant for the arrangement of a cluster of turbines, since the global efficiency and the energy production could be affected if the distances between the turbines are not enough to allow the recovery of the velocity deficit. Beyond the turbine performance issue, another important aspect to take into consideration is the turbine impact on stratification. The presence of the turbine may produce vertical mixing and, locally alter the features of the stable stratified ambient, increasing vertical mixing in a region typically characterized by internal waves. The tidal sites where marine turbines are usually installed, can be characterized by the presence of stable stratified flow conditions, where temperature and/or salinity are the stratifying agents. Mainly there are two types of sites associated to specific marine dynamics and stratification conditions: the shelf seas and the estuarine environment. Shelf seas are characterized by seasonal temperature stratification that occurs when superficial heating is enough to overcome the vertical mixing process. The sharp seasonal thermocline, which takes place in the summer season, keeps an abrupt separation between the superficial water, warm and less dense, from the deep water, denser and colder. The temperature thermocline moreover determines the

biological marine dynamics of the site, where usually the superficial layer is characterized by high light and low nutrient content and the deeper layer by high nutrient fluid. The temporal evolution between mixing and seasonal stratification is an important cycle that controls the biological process of the shelf seas [49]. Besides the shelf seas, the other environment where turbines can be installed is the estuarine two layer circulation. Stratification within the estuary dynamics is one of the most important characteristics since it has a control on vertical mixing and influences the vertical distribution of chemical and biological substances. Stratification in an estuarine environment is due to the input of fresh water from the mouth of a river into the saline basin forming a sharp halocline between the upper layer of freshwater and the bottom layer of saline water. Also temperature variations can be an agent of stratification but in the estuarine environment the salinity contribution dominates. In order to form, the stratification must overcome the mixing process due to the tidal streams; this is possible if the tidal stream is weak or if the freshwater input is strong. For example as regards the salt wedges, which are classified as highly stratified estuaries [50], stratification occurs even in presence of strong tidal streams, as long as the freshwater input from the river is enough to renew the stratification.

Considering the importance of the stratification in the flow dynamics, the aim of this chapter is to evaluate whether stable stratification could entail an impact on turbine efficiency and on wake development and extent. On the other side we want to estimate the effect of turbine mixing on stable stratified conditions. Two types of stable stratified conditions have been taken into account: a weak stratification and a strong stratified condition. The weak stratification has been simulated imposing a temperature jump in order to obtain a vertical density profile with a step shape. The same has been done for the strong stratification, but imposing a salinity jump which originates a higher density variation between the two layers compared to the weak case. Then the turbine was introduced into the two stratified fields and the analysis of results of the two cases will be illustrated. At the end of the chapter a comparison between the two stratified cases will be shown, evaluating the difference in terms of turbine power characteristics and wake recovery. Before introducing the two stratified cases, in the next section, the results of a simulation without the stratified field will be analyzed. This analysis will be useful as a benchmark.

5.2 LES of a turbine in a non-stratified field

5.2.1 Simulation setup and field analysis

In this section the results of a simulation performed in absence of density stratification will be presented. First we introduce the simulation without stratification, since it will be used later in the dissertation as a reference. In the next sections the present

case will be compared to the simulations with a strong and a weak stable stratified condition. The comparison will be useful to determine whether the stratification might bring changes in the results, in particular for what concerns the power output and wake development and retrieve. Moreover the common practice in the numerical simulation field of marine turbines is to perform simulations without considering the stratification. For these reasons it's important to evaluate if the stratification should be taken into account to reach results more congruent with the real scenario.
Before introducing the turbine inside the domain, it's necessary to analyze the field

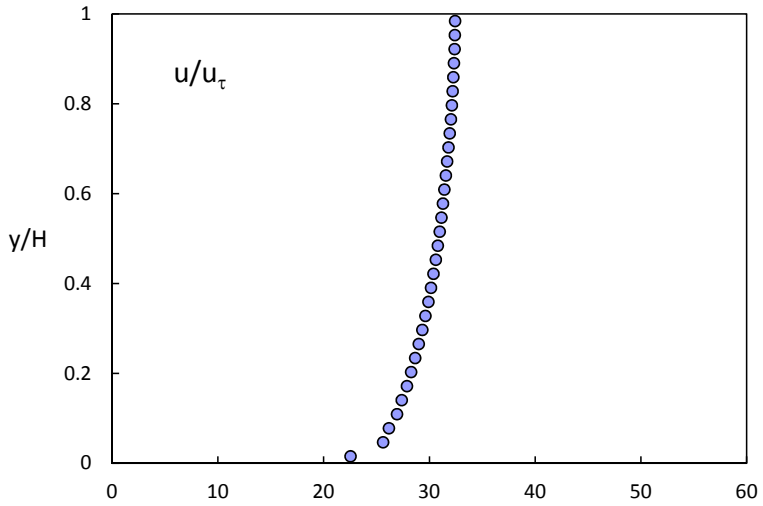

Figure 5.1: Vertical profile of non-dimensional mean streamwise velocity

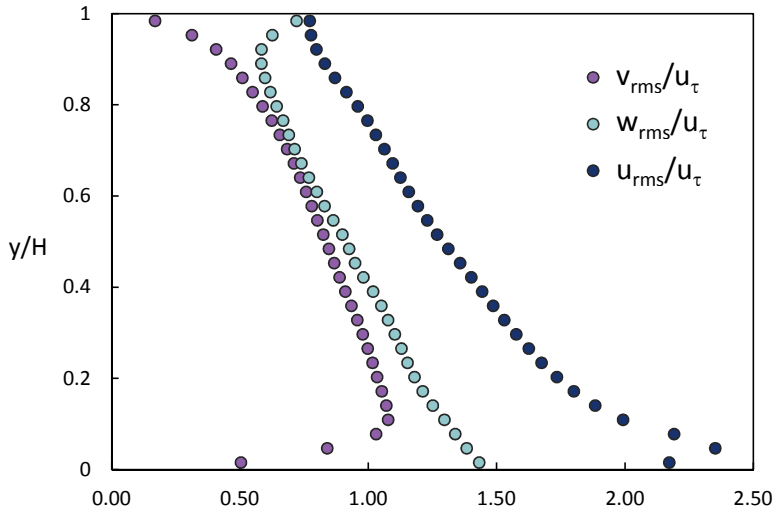

Figure 5.2: Vertical profile of *rms* of non-dimensional velocities fluctuations

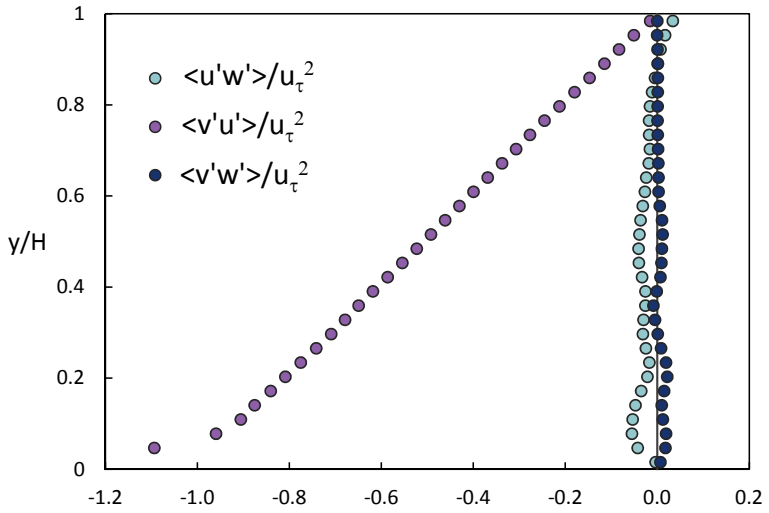

Figure 5.3: Vertical profile of non-dimensional Reynolds shear stresses

without the turbine to better understand the mechanisms that occurs in presence of the rotor. A first LES has been performed without the turbine. The domain of the simulation and the computational grid is the same used for the numerical validation of the ADM-R model. The velocity boundary conditions remain the same used for the ADM-R validation, except for the lateral walls where periodic condition is applied. Also the blade settings employed have the characteristics illustrated in section 4.2. The free stream velocity at the rotor hub height is equal to $U_\infty = 1.5$ m/s with a Reynolds number of $Re = 1.2 \cdot 10^6$, based on the rotor diameter. In the streamwise direction the flow was driven by a constant pressure gradient $dp/dx = 1.28 \cdot 10^{-6}$ m/s^2. The simulation has been run till the flow reached the steady state condition. The non-dimensional time needed to obtain the steady state condition is $t = 80.25$. The non-dimensional time has been calculated by means of the free stream velocity and the characteristic length which is H, the vertical dimension of the domain. The statistics have been calculated averaging in time, and over the horizontal planes of homogeneity. Figure 5.1 shows the vertical profile of the non-dimensional mean streamwise velocity. The vertical profiles of *rms* of velocity fluctuations are depicted in figure 5.2, the behavior of the *rms* near the free surface is consistent with the boundary condition imposed, where the shear is set to zero. Figure 5.3 shows the vertical profiles of the shear stresses: as expected, the shear components $< v'w' >$ and $< u'w' >$ both tend to zero; the shear component $< u'v' >$ is not negligible compared to the other components.

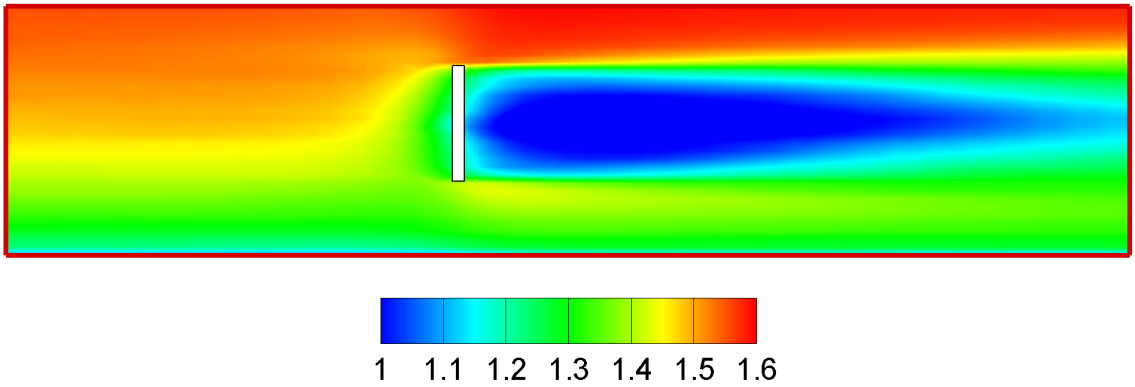

Figure 5.4: Contour plot of time averaged streamwise velocity U [m/s] for a vertical longitudinal plane $(x-y)$ which crosses the turbine center, non-stratified case.

5.2.2 Interaction between the turbine induced forces and the non-stratified field

During the above mentioned simulation data set at a fixed transverse plane have been collected, then a new LES has been performed with periodicity along the spanwise direction and with a non-periodic condition along the streamwise direction. The data set collected during the previous simulation are used as inflow data. Then the turbine was introduced into the domain and a LES was performed coupled with the ADM-R model. The simulation was run for a time equal to the previous simulations and the statistics has been made averaging the variables in time. In figure 5.4 it is shown the contour plot of time averaged streamwise velocity U for a vertical plane. The drop of velocities downstream the rotor is evident from figure 5.4. The wake gradually starts to recover moving downstream as the wake expands and entrains the surrounding field. The expansion of the wake is more evident analyzing figure 5.5, where the contour plot of the time averaged streamwise velocity is plotted for vertical spanwise planes at different downstream distances from the rotor. It can also be observed that as the wake spreads, the velocity deficit starts to recover. In figure 5.6 it is shown the contour plot of time averaged streamwise velocity for an horizontal plane, where it can be observed the lateral spreading of the wake and the velocity deficit. Figure 5.7 shows three velocities iso-surfaces which highlights the three dimensional deformation of the streamwise velocity field due to the rotor influence.

In order to assess the velocity deficit induced by the turbine and to define a quantity that is not dependent on the incoming velocity, we compute a non-dimensional

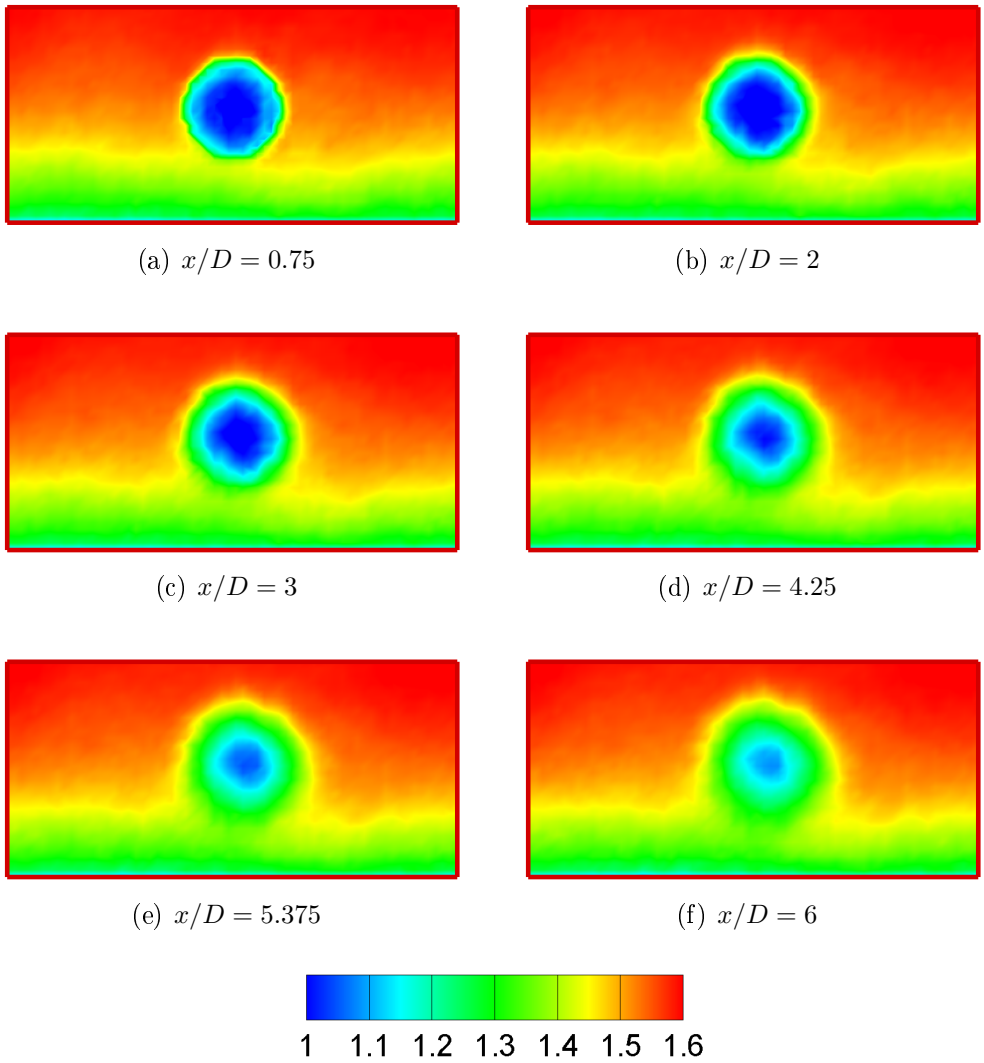

(a) $x/D = 0.75$ (b) $x/D = 2$

(c) $x/D = 3$ (d) $x/D = 4.25$

(e) $x/D = 5.375$ (f) $x/D = 6$

Figure 5.5: Contour plot of time averaged streamwise velocity $U\ U$ [m/s] for vertical traversal planes $(y-z)$, at different downstream distances, non-stratified case.

velocity deficit as follows [11]:

$$\frac{\Delta U}{U_{hub}} = \frac{(U_\infty - U)}{U_{hub}} \tag{5.1}$$

where U_∞ is the time averaged inflow velocity, U_{hub} is the time averaged inflow velocity at the hub height and U is the time averaged velocity at a specific downstream distance from the rotor. Through this quantity we can also evaluate the recovery of the wake as a function of the downstream distance from the turbine. Moreover

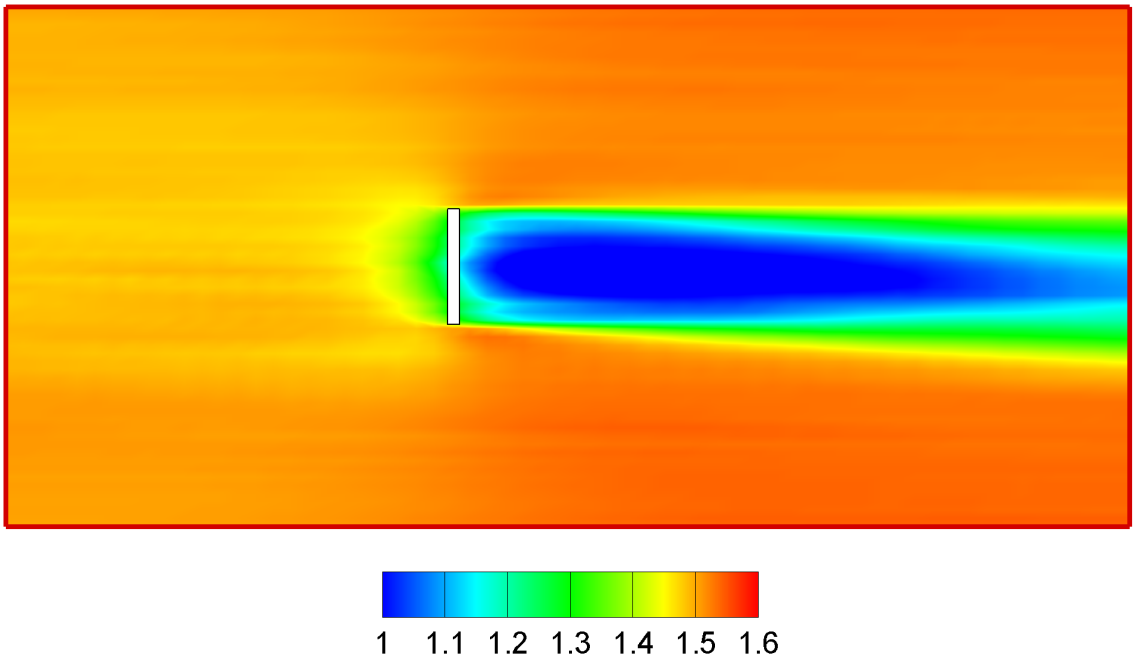

Figure 5.6: Contour plot of time averaged streamwise velocity U [m/s] for an horizontal plane $(x - z)$ which crosses the turbine center, non-stratified case.

using a non-dimensional velocity deficit, it is possible to make a comparison between cases that have different incoming velocities. Figure 5.8 shows the non-dimensional velocity deficit vertical profiles at specific rotor distances defined as x/D, where x is the coordinate in the x direction minus the x_{rot}, that is the coordinate of the rotor center in the streamwise direction. Figure 5.9 shows the non-dimensional velocity deficit horizontal profiles at two specific rotor distances. Figures 5.8 and 5.9 can help to understand more in detail the velocity deficit and wake recover illustrated in figures 5.4 and 5.6. As we move downstream the maximum non-dimensional velocity deficit, which is located near the center of the rotor, recovers from 0.437 at a distance of $x/D = 1$, up 0.3 at a distance of $x/D = 5$. The profiles for $x/D = 1$ and $x/D = 3$ exhibit a less regular shape compared to the one for $x/D = 5$, this is due to the proximity to the rotor of the two closer profiles. As concern the power characteristics, we found that the power output that the turbine can extract from the flow field is around 292 W with a power coefficient of $C_P = 0.35$.

An important physical quantity to take into account is the turbulent intensity that is responsible for the fatigue on the turbine structures [51] [52]. Besides the ambient turbulence which influences the development of the wake [8], turbulence

intensity induced by the presence of the rotor can have a remarkable effect on downstream turbines. In fact within a turbine farm, the downstream turbine hit by the wake of an upstream turbine could be subject to an increase of loads due to the high turbulence levels induced by the upstream rotor. Moreover, as we will see, the turbulence intensity represents an important factor in the development of the wake. The common practice suggests to analyze the behavior of streamwise turbulence intensity, however as reported by Abkar et al. [11] in the case of stratification the streamwise turbulence intensity is not enough to evaluate the impact of stratification on turbine wake. In order to take into consideration all turbulence intensity components, the total turbulence intensity is defined as:

$$TI = \sqrt{\frac{1}{3}\left(I_u^2 + I_v^2 + I_w^2\right)} \tag{5.2}$$

where:

$$I_u^2 = \frac{u_{rms}}{U_{hub}}$$
$$I_v^2 = \frac{v_{rms}}{U_{hub}}$$
$$I_w^2 = \frac{w_{rms}}{U_{hub}}$$

u_{rms} is the root mean square of turbulent streamwise velocity fluctuations, v_{rms} is the root mean square of turbulent spanwise velocity fluctuations, w_{rms} is the root mean square of turbulent vertical velocity fluctuations and U_{hub} is the time averaged of the streamwise inflow velocity.

Figures 5.10 and 5.11 show the total turbulence intensity respectively for a vertical plane and for an horizontal plane. From figures 5.10 and 5.11 it can be observed an enhancement of the total turbulence intensity in the wake of the rotor. Moreover it can be seen that the magnitude of the total turbulence intensity doesn't change significantly for the horizontal and vertical plane. To better understand the behavior of the turbulence intensity, in figures 5.12 and 5.13, the vertical and spanwise profiles of the total turbulence intensity are plotted for two distances downstream the rotor. Figure 5.12 shows that the total turbulence intensity has a peak at the top tip in the plane that crosses the turbine center. Instead observing figure 5.13, the total turbulence intensity shows a double peak at the top and bottom tip of the rotor. These results are qualitatively consistent with the outcome illustrated in the study of Abkar et al. [11]. The high values of turbulence intensity at the top tip for the streamwise profile and at the bottom and top for the spanwise profile, are connected to the strong production of turbulent kinetic energy associated with high level shear at those location. As it can be seen from fig 5.12 and 5.13, the profiles of the total turbulence intensity are not subject to damping between the

two downstream location, this is due to the fact that the far downstream location of the simulation domain is relatively short compared to the total wake extension.

In figures 5.14 and 5.15 shows respectively the contour plot of the $< u'v' >$ shear stress for a vertical plane and the contour plot of the $< u'w' >$ shear stress for an horizontal plane. These variables measure the entrainment of mean kinetic energy from the surrounding field into the wake. From figure 5.14 it can be observed that the presence of the turbine gives rise to a localized shear stress that forms at the wake edge. The $< u'v' >$ shear stress has a negative value at the upper edge and a positive value at the lower edge. As for $< u'v' >$, the $< u'w' >$ shear stress is localized at the edge of the wake, with a positive value at one side of the wake edge and a negative magnitude at the other side of the wake edge. This behavior is qualitatively consistent with Abkar et al. and it is due to the strong entrainment from the adjacent field into the wake. The magnitude of the $< u'v' >$ shear stress is higher than the $< u'w' >$ shear stress, this means that there is a more intense lateral momentum flux that implies an higher entrainment of mean kinetic energy from the lateral edged of the wake.

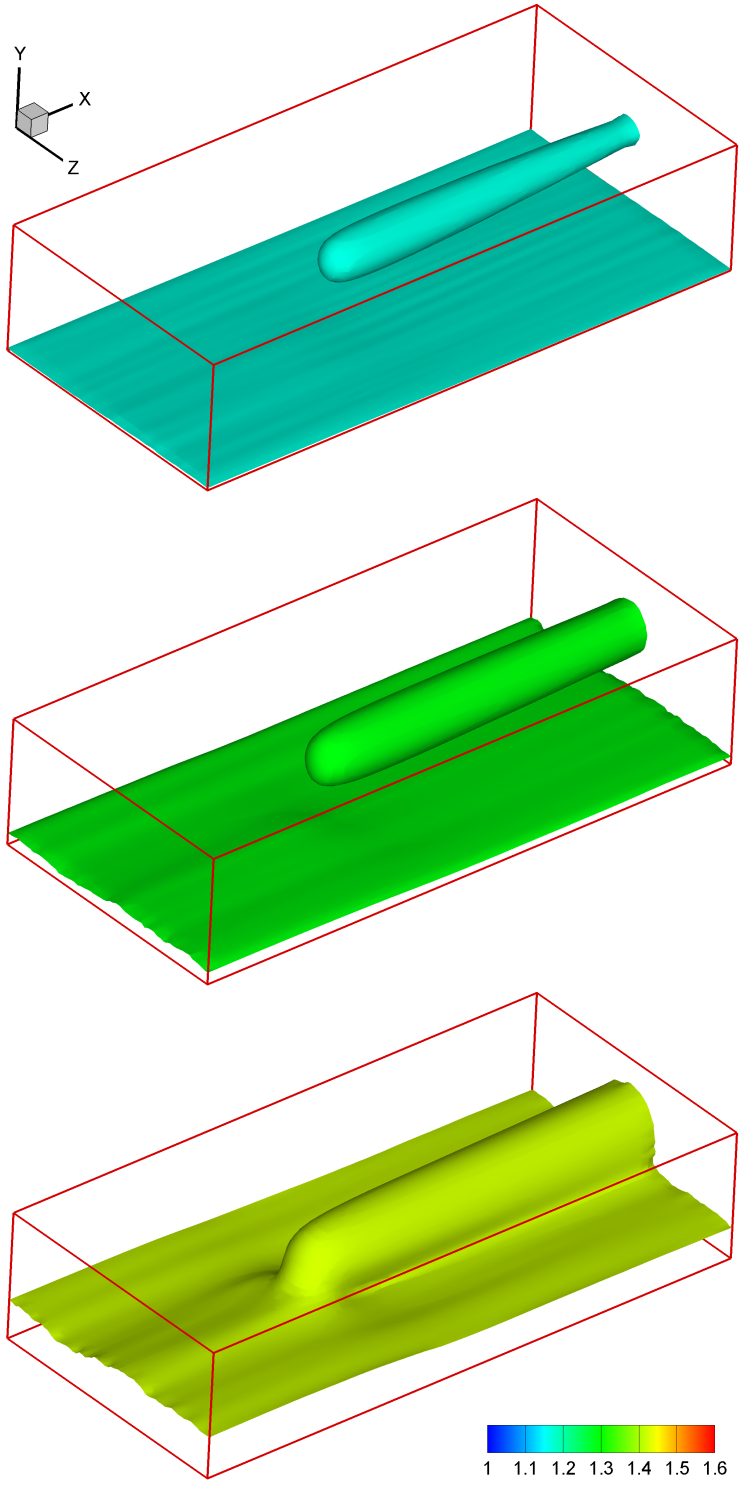

Figure 5.7: Iso-surfaces of time averaged streamwise velocity U [m/s], non-stratified case. Top: 1.17 m/s, middle: 1.29 m/s and bottom: 1.42 m/s

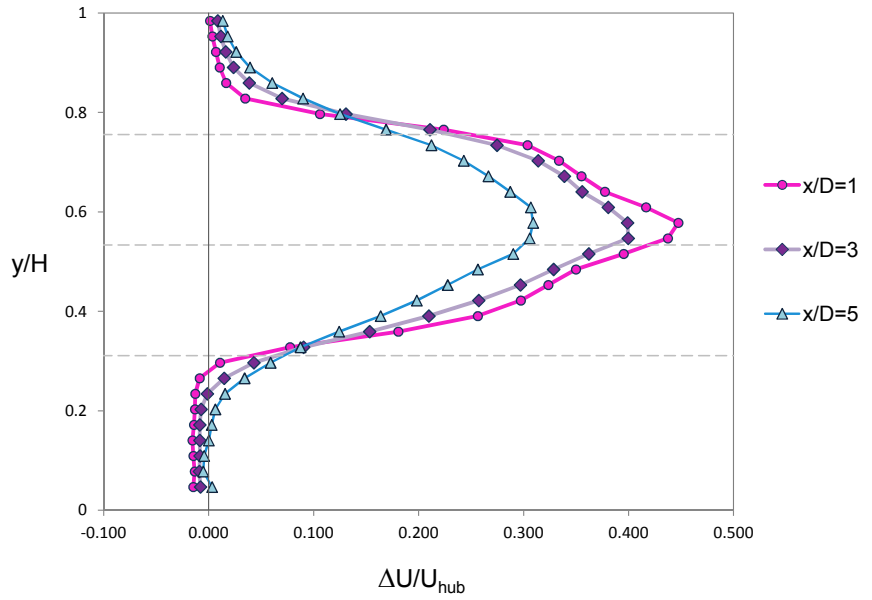

Figure 5.8: Non-dimensional velocity deficit profiles at different downstream distances from the rotor, for a vertical plane across the turbine center, non-stratified case.

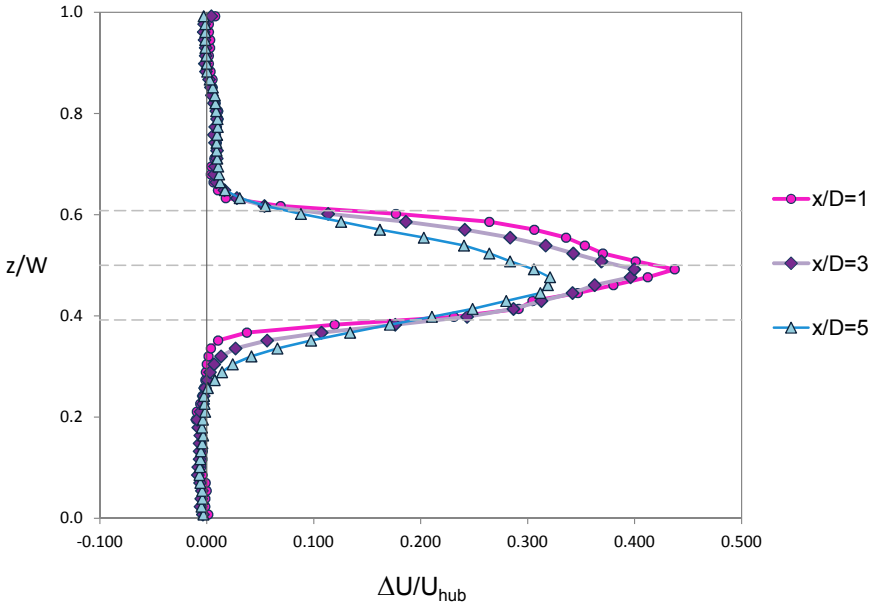

Figure 5.9: Non-dimensional velocity deficit profiles at different downstream distances from the rotor, for an horizontal plane across the turbine center, non-stratified case.

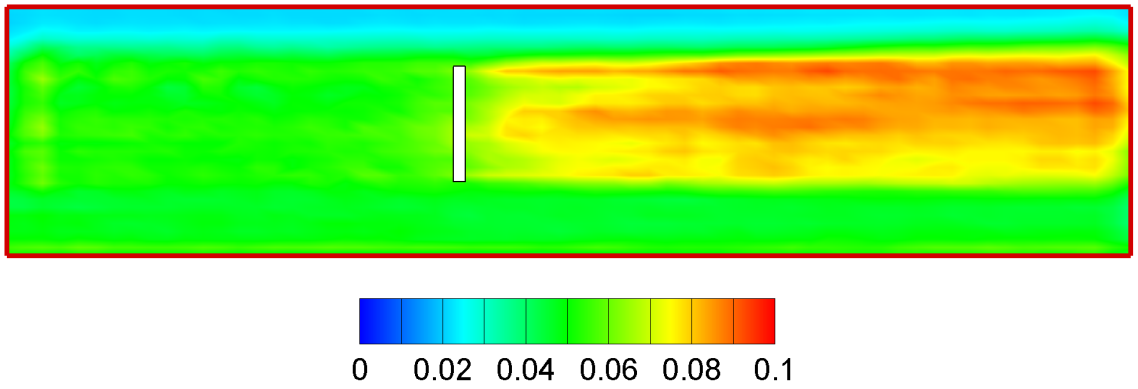

Figure 5.10: Contour plot of time averaged total turbulence intensity for a vertical longitudinal plane (x-y) which crosses the turbine center, non-stratified case.

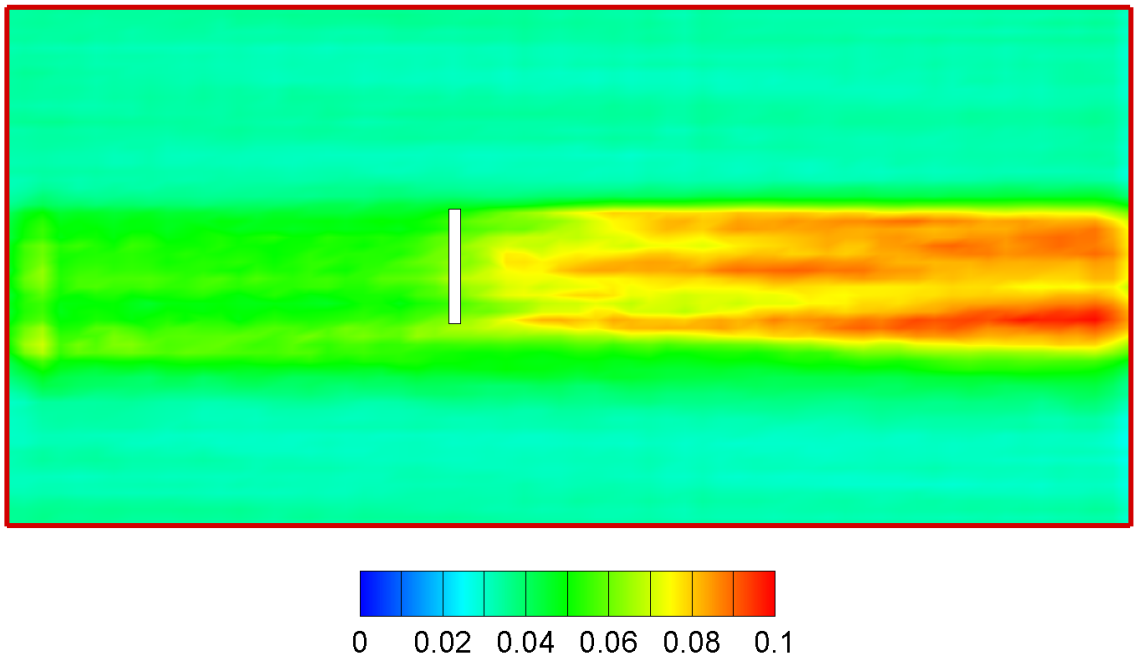

Figure 5.11: Contour plot of time averaged total turbulence intensity for an horizontal plane (x-k) which crosses the turbine center, non-stratified case.

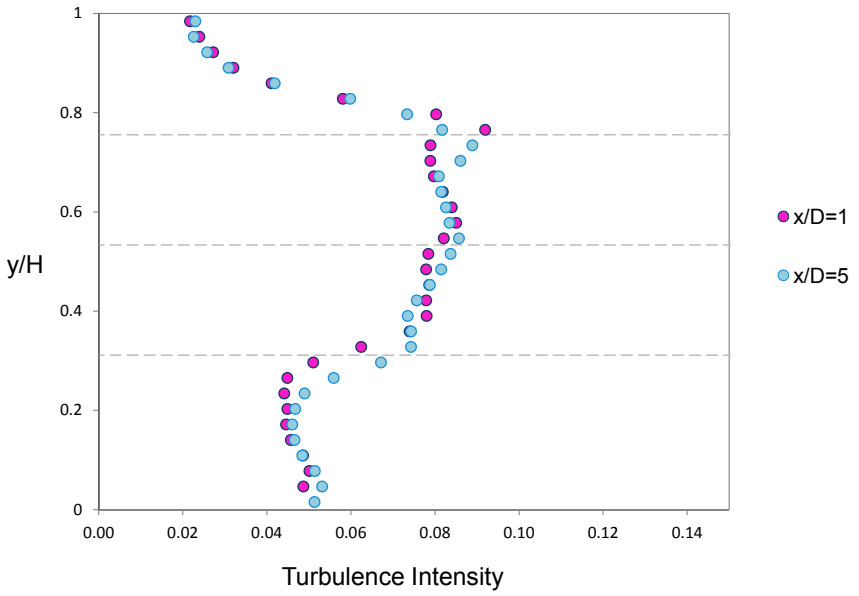

Figure 5.12: Time averaged vertical profiles of total turbulence intensity at two rotor distances for a vertical longitudinal plane that crosses the turbine center (x-y), non-stratified case.

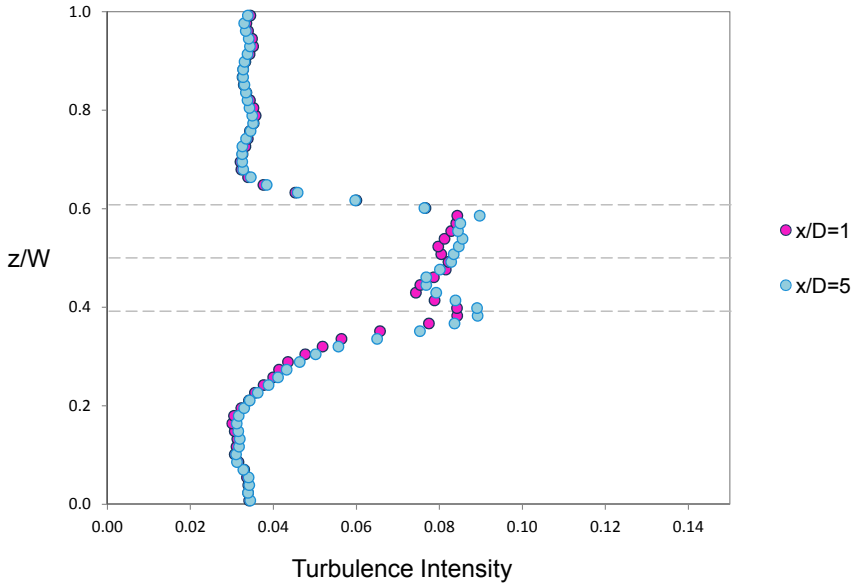

Figure 5.13: Time averaged spanwise profiles of total turbulence intensity at two rotor distances for an horizontal plane that crosses the turbine center (x-k), non-stratified case.

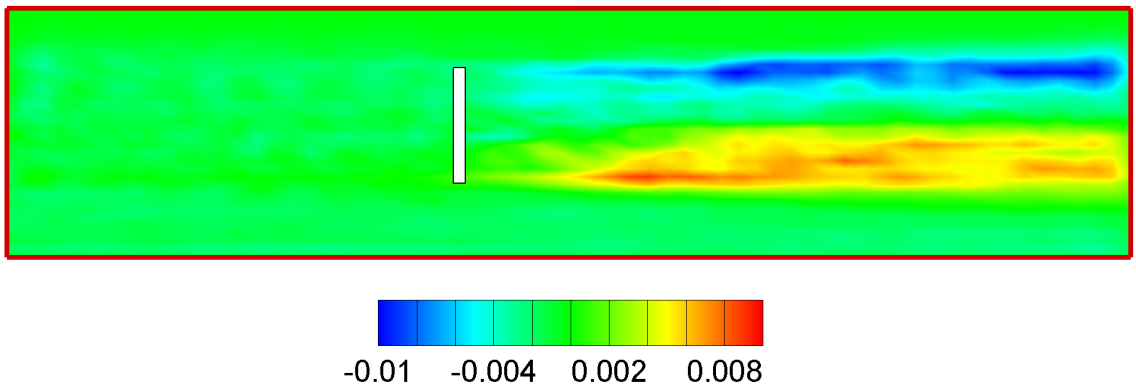

Figure 5.14: Contour plot of time averaged shear stress $< u'v' >$ for a vertical longitudinal plane (x-y) which crosses the turbine center, non-stratified case.

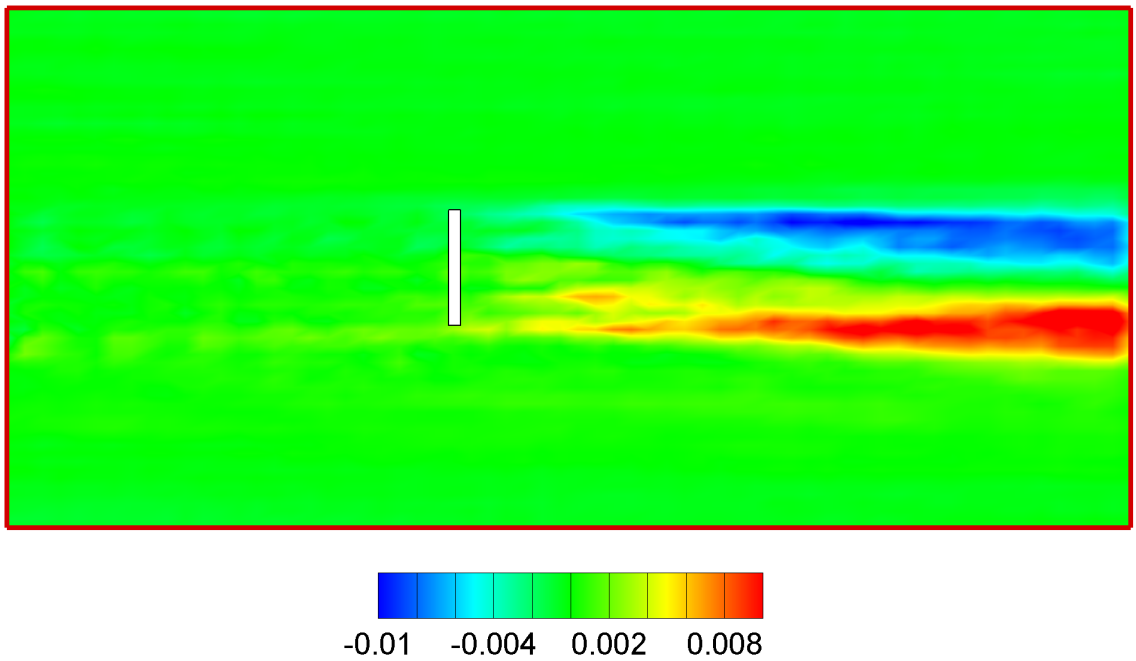

Figure 5.15: Contour plot of time averaged shear stress $< u'w' >$ for an horizontal plane (x-k) across the turbine center, non-stratified case.

5.3 LES of stable stratified conditions

The aim of this chapter is to investigate the influence of stable stratified conditions on wake characteristics and turbine performance. As we said before, we will study the flow and the interaction with the turbine in presence of two types of stratified conditions: a weak and a strong stable stratified condition. In order to simulate a weak stable condition, we imposed a temperature step, while in the case of strong stratified condition a salinity step is set. The salinity jump generates an higher density variation compare to the temperature jump. Before showing the characteristics of the two stratified fields we introduce below the characteristics of the simulations. The domain of the simulation is the same used for the numerical validation of the non-stratified case. Adiabatic boundary conditions are imposed for

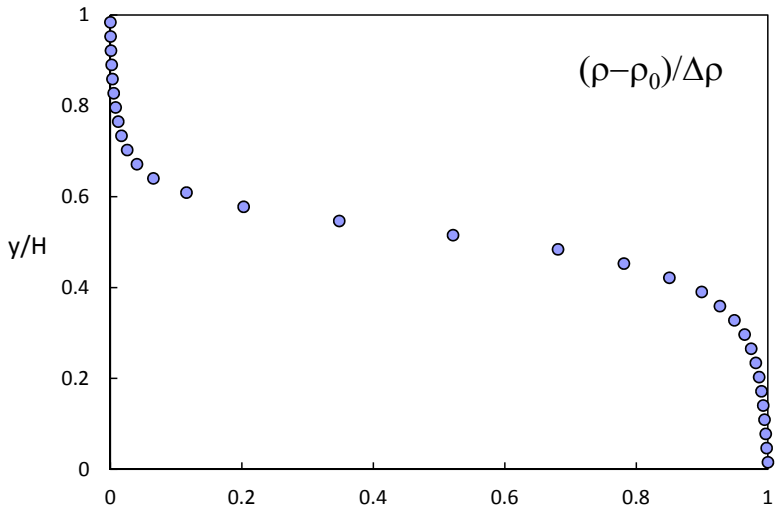

Figure 5.16: Vertical profile of non-dimensional mean density, weak stratification

temperature and salinity at the bottom of the domain and at the free surface implying absence respectively of heat fluxes and salinity fluxes at the boundaries. The velocity boundary conditions remain the same used for the non-stratified case. The simulation setup has been scaled in order to obtain a real-case value of the bulk Richardson number. The Richardson number is the ratio between potential and kinetic energy, where the numerator represents the potential energy barrier that the mixing must overcome and the denominator the kinetic energy that the shear flow should supply to maintain turbulence. It is defined as:

$$Ri_b = \frac{g\Delta\rho h}{\rho_0 U_\infty^2} \tag{5.3}$$

where h is the domain height, g is gravity, $\Delta\rho$ is the vertical density gap and ρ_0 the reference density. For the real case we set an height of $h = 36m$, as it can measure

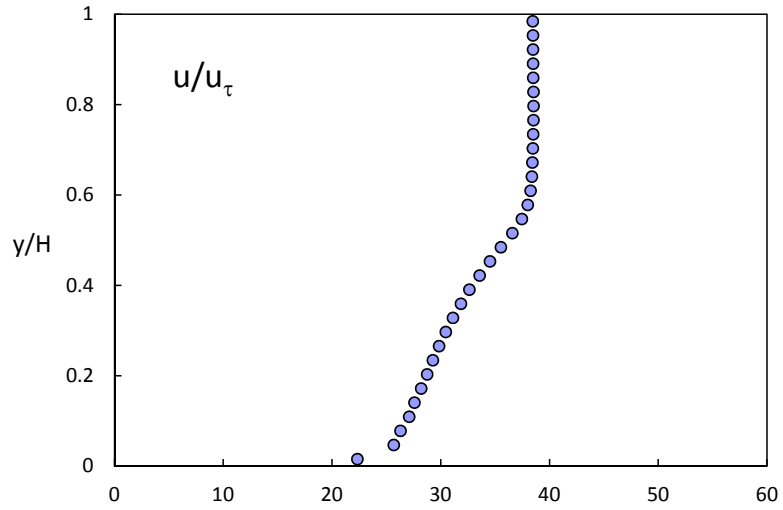

Figure 5.17: Vertical profile of non-dimensional mean streamwise velocity, weak stratification

the seabed or ocean floor depth, where the turbines are installed, and the velocity is set to $U_\infty = 1.5$ m/s. For the weak stratified case the temperature jump between the superficial and the deeper water was set to $\Delta T = 6.67$ degrees and consequently the ratio between $\Delta\rho$ and ρ_0 is $\Delta T\alpha = 0.001$ where α is the thermal expansion coefficient. As concerns the strong stratified case the salinity jump between the superficial and the deeper water was set to $\Delta S = 8$ ppt and consequently the ratio between $\Delta\rho$ and ρ_0 is $\Delta T\beta = 0.00632$ where β is the saline contraction coefficient. The resulting Richardson number for the real case and thus for the simulation is $Ri_{bw} = 0.118$ for the weak case and $Ri_{bs} = 0.992$ for the strong stratified case. As mentioned above, the dimensions of the simulation domain are the same of the non stratified case, and since the free stream velocity at the hub is set to $U_\infty = 1.5$ m/s, the value of g is 147 for the weak case simulation and 196.2 for the strong case simulation. These values are obtained from the equivalence of the bulk Richardson number of the simulation and the one of the real case. The Prandtl number employed in the weak stratified simulation is the typical value for thermal stratified oceanic flows and it is equal to $Pr = 6.5$, as regards the strong stratified condition induced by the salinity jump the Prandtl number is equal to 542.6. Under the conditions above mentioned, LESs have been performed in order to generate the two stratified fields characterized by a step-like jump of density. As reported in the study of Armenio and Sarkar [53], the transient development of the flow in presence of stable stratification, follows different steps in its evolution to turbulence and mixing. An initial transient is characterized by a sudden decrease of the wall shear stress, due to the sudden transformation of kinetic energy into potential energy and by flow

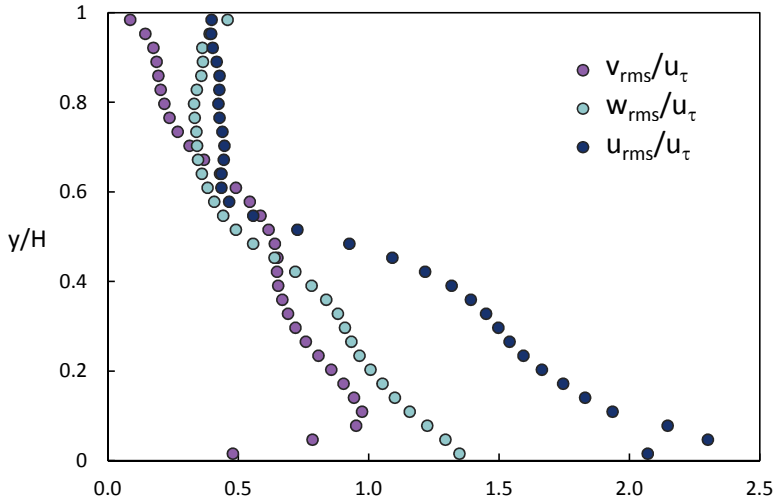

Figure 5.18: Vertical profile of rms of non-dimensional velocities fluctuations, weak stratification

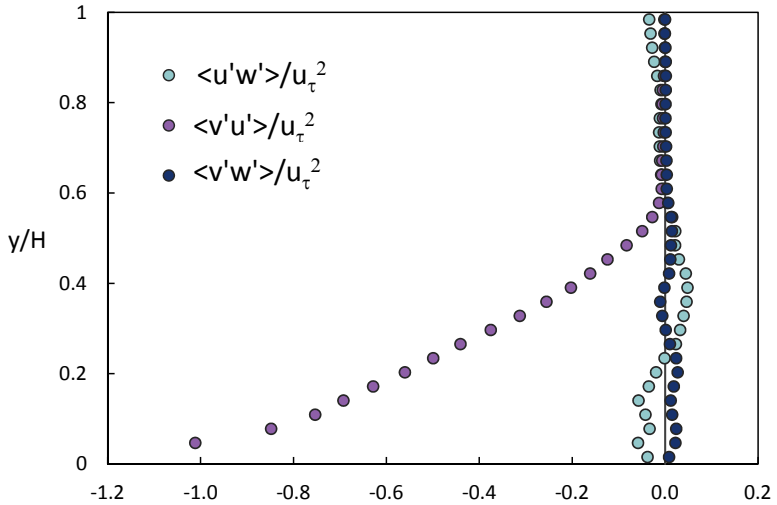

Figure 5.19: Vertical profile of non-dimensional Reynolds shear stresses, weak stratification

re-laminarization. Since the pressure gradient is constant, the unbalance between driving and drag force accelerates the flow, up to a new transition to turbulence, where the shear stress starts to increase again. The two stratified fields are obtained during the transient phase since this allows to obtain a mild smoothing of the step-like density profile; otherwise the mixing process would untied the step density profile advancing in time. However the data are collected and all the statistics are computed during a time window where the flow is nearly steady in a statistical sense.

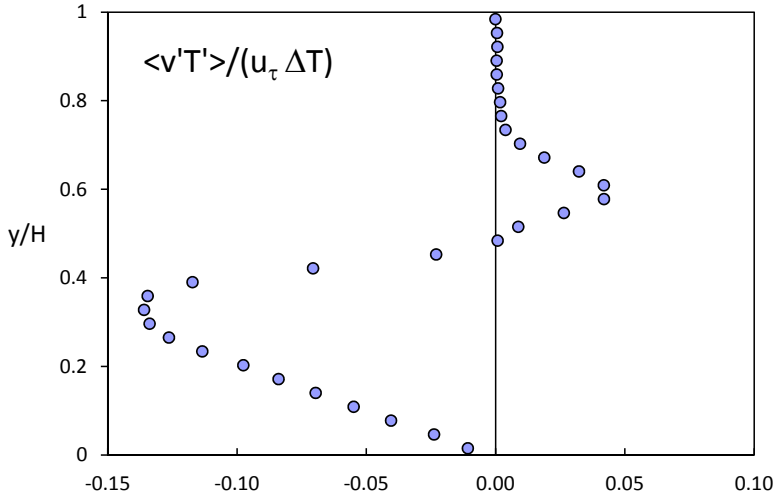

Figure 5.20: Vertical profile of non-dimensional temperature flux, weak stratification

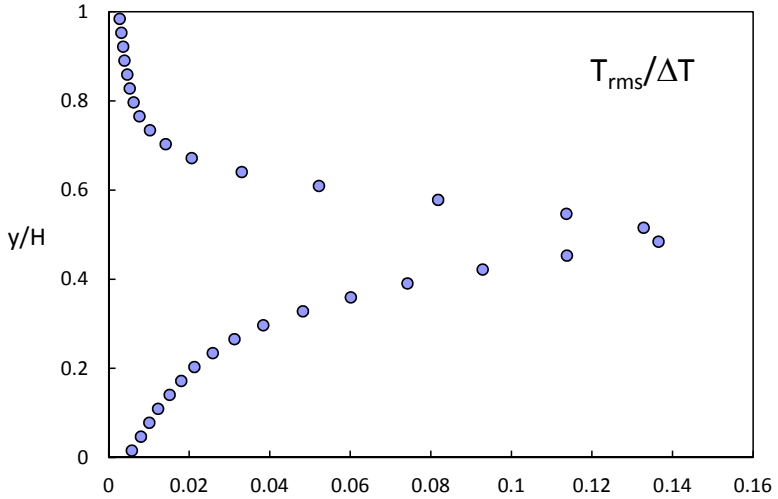

Figure 5.21: Vertical profile of non-dimensional temperature fluctuations, weak stratification

In order to make a comparison between the two stratified cases, the starting times of data collection (inflow field) for both cases is equal to 150. The time window for the two stratification cases has been chosen equal to $t \cdot N = 8$, where N is the Brunt Väisälä frequency [54], long enough for statistical convergence. The Brunt Väisälä frequency is defined as:

$$N = \sqrt{-\frac{g}{\rho_0}\frac{d\rho}{dy}} \tag{5.4}$$

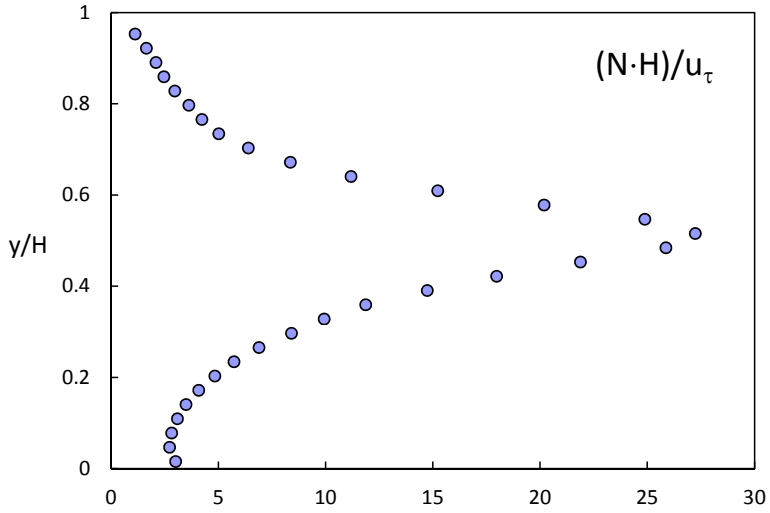

Figure 5.22: Vertical profile of non-dimensional Brunt Väisälä frequency, weak stratification

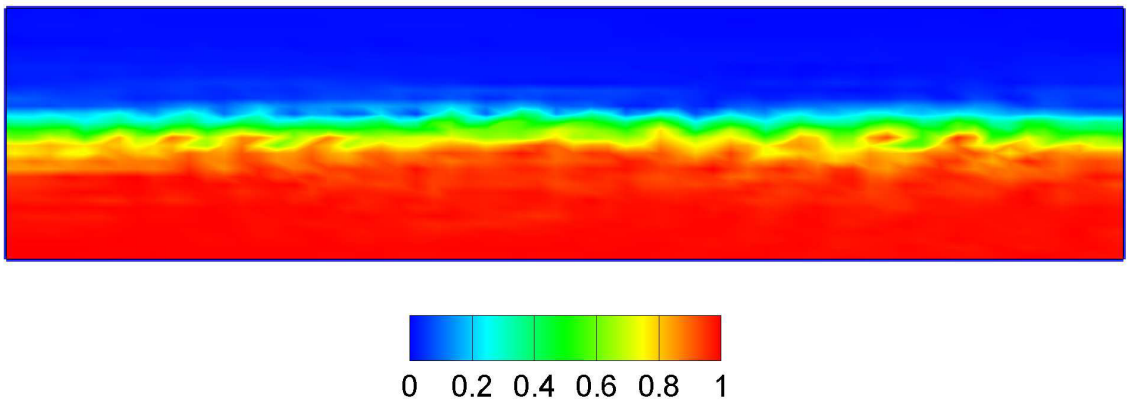

Figure 5.23: Contour plot of instantaneous non-dimensional density field for a vertical longitudinal (x-y) plane, weak stratification

The Brunt Väisälä frequency is the frequency of oscillation of a parcel when it is displaced from its equilibrium state. In fact in case of a stable stratified condition, if a parcel is displaced upward, the parcel will be surrounded by lighter fluid and so it will fall down gaining velocity, when reached again the initial equilibrium state it will go further down subject to the inertial force; then the parcel will be surrounded by heavier fluid and will be pushed upward and this oscillations will persist around the equilibrium state.

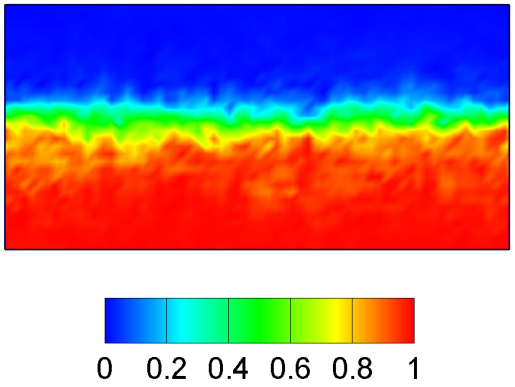

Figure 5.24: Contour plot of instantaneous non-dimensional density field for a vertical spanwise (z-y) plane, weak stratification

5.3.1 Analysis of weak stratified field

In this section the weak stratified field is analyzed. First it will be described the mean field and then the instantaneous characteristics of the field will follow. The statistics are calculated averaging in time, and over the horizontal planes of homogeneity. Figure 5.16 shows the vertical profile of the non-dimensional mean density, which exhibits a sharp gradient in the interface region. Figure 5.17 shows the mean streamwise velocity vertical profile that indicates that turbulence is completely suppressed in the upper area of the domain, whereas in the lower part a turbulence production an be observed due to the vertical velocity gradient coupled with the Reynolds stress showed in the next figures. he suppression of turbulence is confirmed analyzing the vertical profiles of rms of velocity fluctuations, figure 5.18, and profiles of the shear

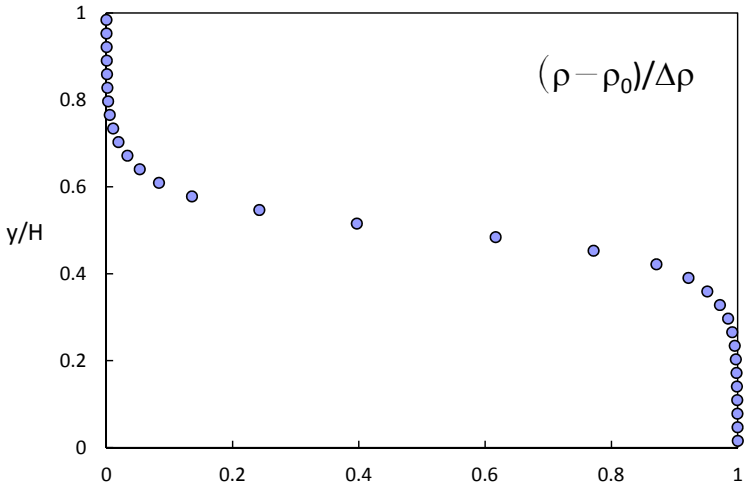

Figure 5.25: Vertical profile of non-dimensional mean density, strong stratification

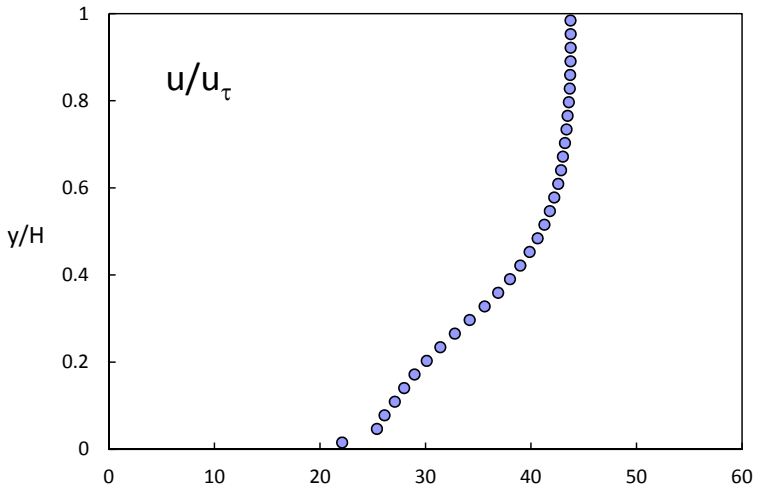

Figure 5.26: Vertical profile of non-dimensional mean streamwise velocity, strong stratification

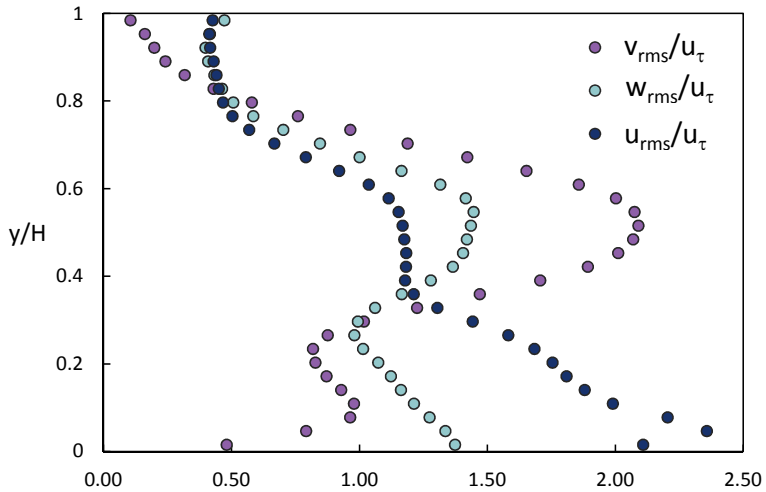

Figure 5.27: Vertical profile of rms of non-dimensional velocities fluctuations, strong stratification

stress, figure 5.19. Figure 5.20 shows the mean vertical temperature flux that before the interface reaches the maximum value and then toward the interface tends to zero. As expected the profile of root mean square of temperature fluctuations, figure 5.21, has its maximum at the centre of the channel, where the temperature gradient is maximum, while at the boundaries it tends to zero. The vertical profile of the Brunt Väisälä frequency, figure 5.22, reaches the maximum value at the interface where the density gradient and then the parcels frequency oscillation is maximum.

During the above mentioned simulation data set at a fixed transverse plane have

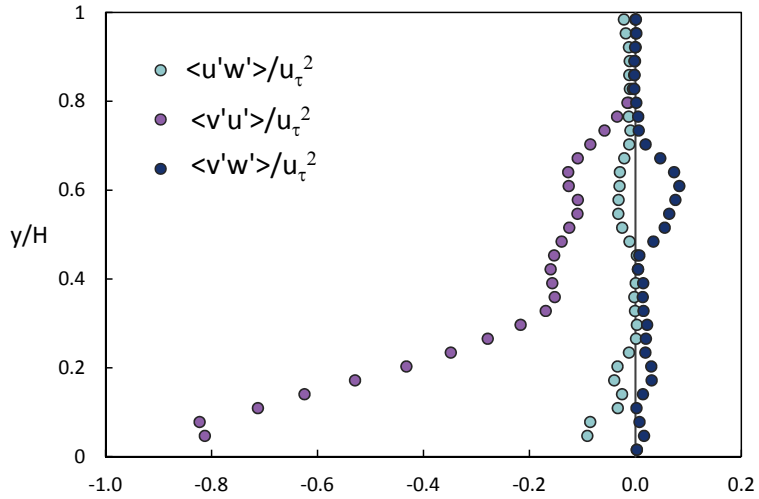

Figure 5.28: Vertical profile of non-dimensional Reynolds shear stresses, strong stratification

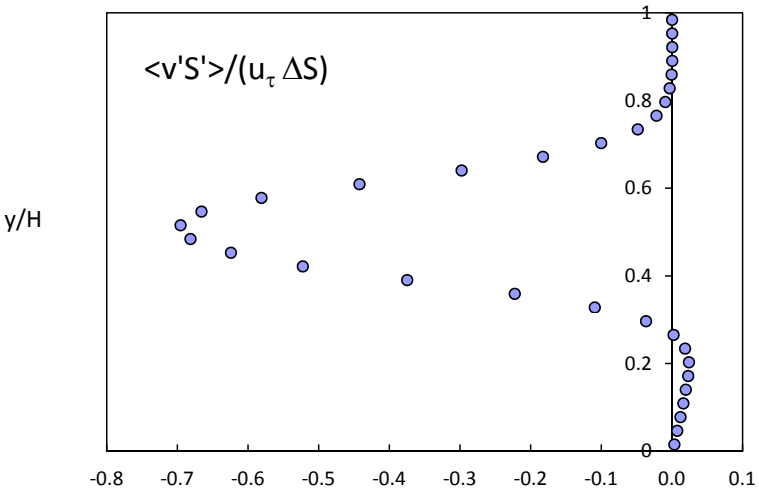

Figure 5.29: Vertical profile of non-dimensional temperature flux, strong stratification

been collected, then a new LES has been performed removing periodicity in the streamwise direction and imposing the data set collected before as inflow. Figures 5.23 and 5.24 show the contour plot of instantaneous temperature respectively for a vertical longitudinal and a vertical transversal plane. A core region is detected characterized by Kelvin-Helmotz dynamics and internal waves, wrapping the interface where the step-like density profile is present. Turbulent structures are visible

in the bottom region, where the solid wall supplies turbulent production; the top region appears less energetic in particular going up toward the free surface, where production of turbulence is absent. The internal waves depicted in figures 5.23 and 5.24, convert forth and back potential energy into kinetic energy.

5.3.2 Analysis of strong stratified field

The results of a LES simulation performed in order to obtain the strong stable stratified field are below described. As for the weak simulation case, the statistics are calculated averaging in time and over the horizontal planes of homogeneity. Figure 5.25 shows the vertical profile of the mean non-dimensional density, which is the result of the smoothing of the step-like density due to the vertical diffusion of momentum. Figure 5.26 shows the mean velocity vertical profile that compared to the weak stratified case, figure 5.17, exhibits a steeper gradient. As for the weak stratification, the turbulence is suppressed in the upper area of the domain. The turbulence production occurs in the lower region due to the vertical velocity gradient

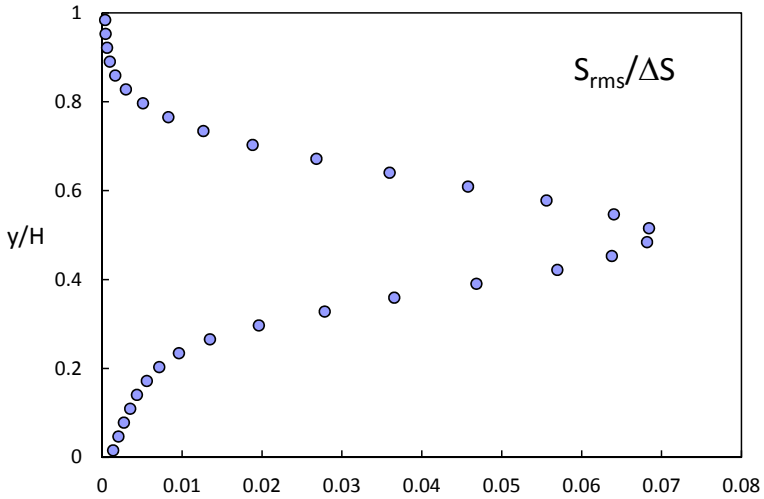

Figure 5.30: Vertical profile of non-dimensional temperature fluctuations, strong stratification

coupled with the Reynolds stress which are shown in the next figures. Analyzing the vertical profiles of rms of velocity fluctuations, figure 5.27, it can be seen that at the core of the channel, where internal waves occur, there are high values of *rms*. Figure 5.28 shows the profiles of the shear stress, where again toward the free surface the turbulence is suppressed. In figure 5.29 it shown the vertical salinity flux which as expected has negative values and its minimum is located at the core of the channel. The profile of root mean square of salinity fluctuations, figure 5.30, has its maximum

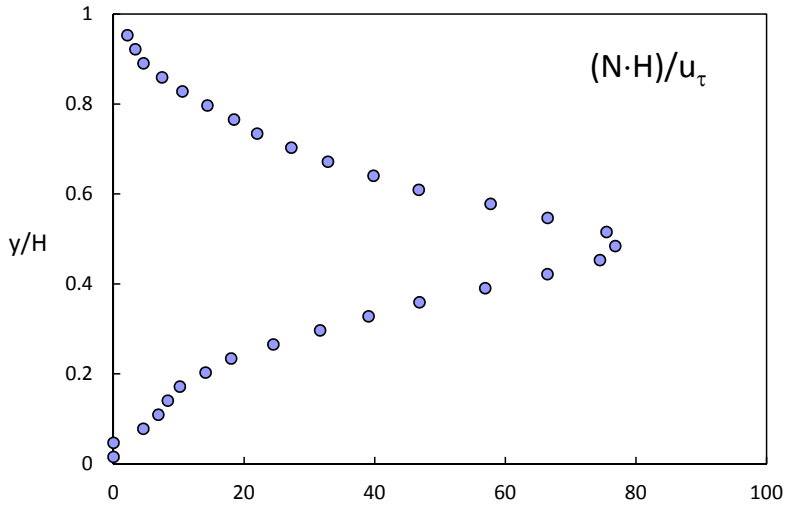

Figure 5.31: Vertical profile of non-dimensional Brunt Väisälä frequency, strong stratification

at the center of the channel, where the salinity gradient is maximum. The vertical profile of the Brunt Väisälä frequency, figure 5.31, reaches the maximum value at the interface where the density gradient and then the parcels frequency oscillation are maximum. Since in the case of strong stratification the density difference is much higher compared to the weak stratified case, as a consequence the Brunt Väisälä frequency of the strong condition, figure 5.31, is higher than the weak condition, figure 5.22. As for the previous case we removed the periodicity in the streamwise direction and we performed a LES with the dataset collected at fixed transversal planes as inflow. Analyzing the contour plot of the instantaneous salinity field for

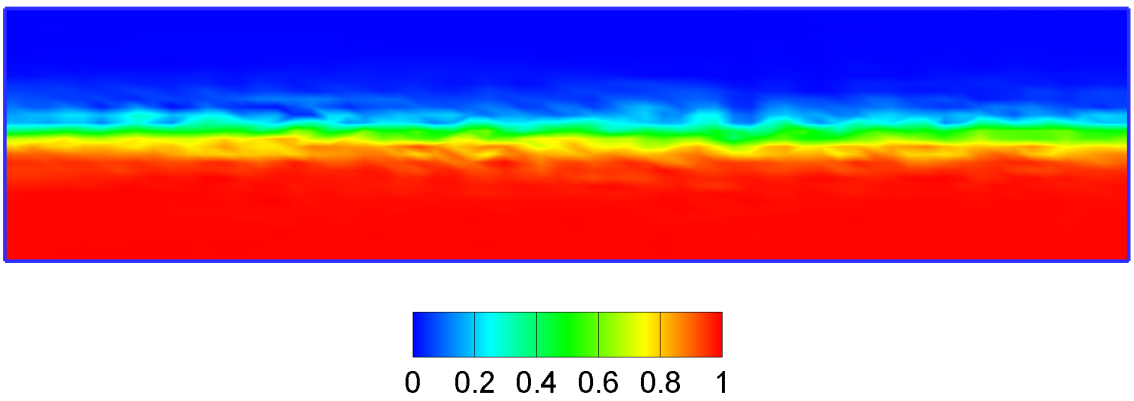

Figure 5.32: Contour plot of instantaneous non-dimensional density field for a vertical longitudinal (x-y) plane, strong stratification

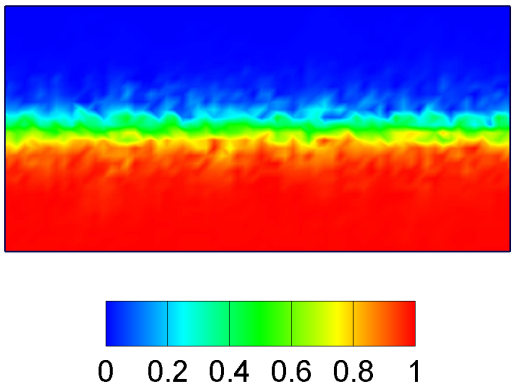

Figure 5.33: Contour plot of instantaneous non-dimensional density field for a vertical spanwise (y-k) plane, strong stratification

a vertical longitudinal plane and a vertical spanwise plane, figures 5.32 and 5.33, we observe the dynamics already detected for the weak case: the development of Kevin-Helmotz instabilities and internal waves at the interface.

5.4 Influence of stratification on the turbine field

5.4.1 Interaction between turbine induced forces and weak stratification

After the simulation and the analysis of the weak stable stratified case, the turbine was introduced into the domain and a LES was performed coupled with the ADM-R model. As a result of the simulation, in presence of weak stable stratification, figure 5.34 shows the contour plot of the time averaged streamwise velocity for a vertical plane. Figure 5.34 shows the wake development downstream the turbine. It can be observed that the wake is deflected downward, especially when compared to the wake of the non-stratified case of figure 5.4. Moreover, the velocity deficit shape

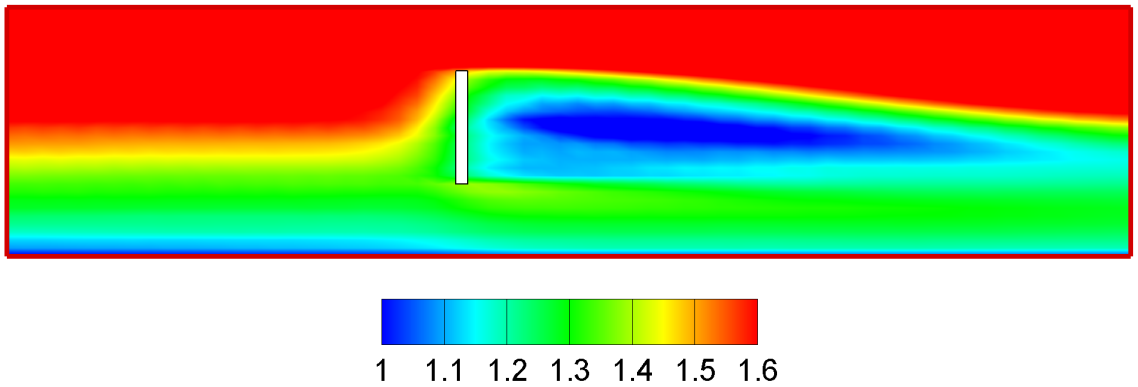

Figure 5.34: Contour plot of time averaged streamwise velocity U [m/s] for a vertical longitudinal plane $(x - y)$ which crosses the turbine center, weak stratified condition.

is not symmetric as in the non-stratified case. From figure 5.35 which shows the contour plot of the time averaged streamwise velocity U for an horizontal plane, it can be observed the downstream lateral spreading and entrainment of the wake and the consequently partial recovery of the velocity deficit. The contour plot of the time averaged streamwise velocity U for transverse vertical planes at different downstream distances, figure 5.36, helps us to understand the downstream development of the wake. As we move downstream, the wake is pushed downward by the above fluid, while the velocity deficit recovers gradually. As we will see, the recovery of the velocity deficit is due to the entrainment of fluid mainly from the bottom and laterally. The three dimensional streamwise velocity iso-surfaces, highlights the deformation of the streamwise velocity field caused by the rotor, figure 5.37. Compared to the non-stratified field, figure 5.7, the velocity iso-surface of 1.51 m/s shows that the wake spreads more laterally and less vertically than the non-stratified case.

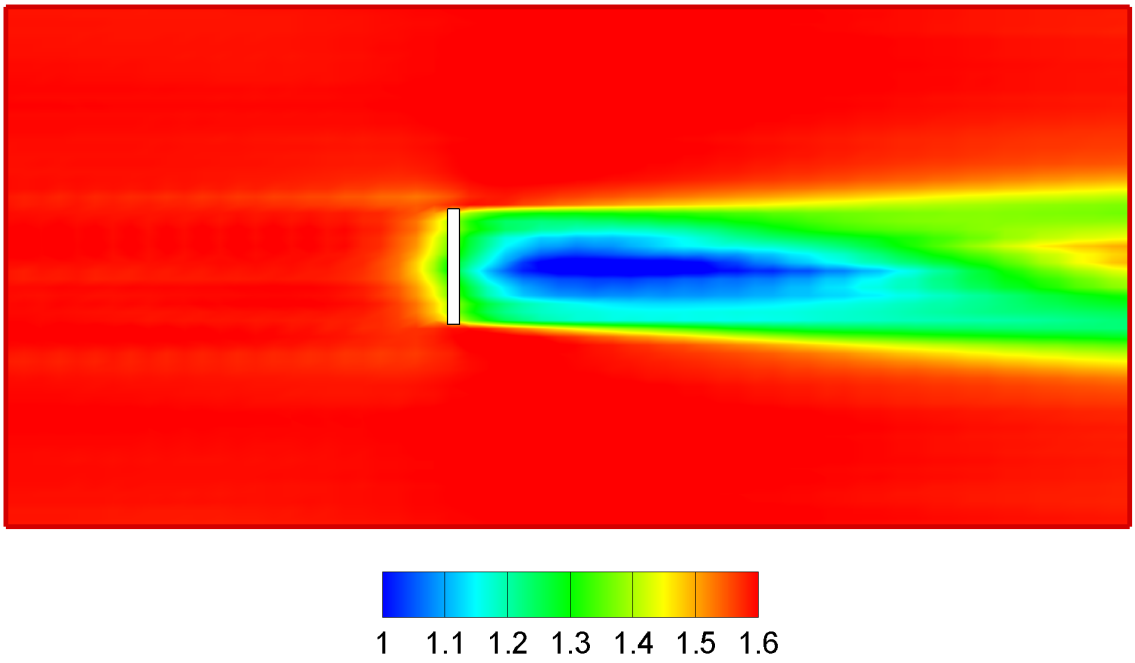

Figure 5.35: Contour plot of time averaged streamwise velocity U [m/s] for an horizontal plane $(x - z)$ which crosses the turbine center, weak stratified condition.

In fact analyzing figures 5.37 and 5.7 it can be observed that the vertical spreading of the wake is restricted and the vertical deformation of the flow field is constrained by the stable stratification. The development of the wake above illustrated, can be ascribed to the so called meandering behavior [55] [56] [57]. This phenomenon has been investigated in literature since it assumes a particular importance in turbine farms. The meandering phenomenon consists in the lack of alignment between the center of the rotor and the trajectory of the wake center. The meandering behavior of the wake is here caused by the stable stratification effect. The total turbulence intensity for a vertical and an horizontal plane are respectively shown in figures 5.38 and 5.39. It can be noticed that the turbulence intensity is subject to an increase due to the presence of the turbine. The turbulence intensity behavior can be analyzed in detail from figures 5.40 and 5.41 where we show respectively the vertical and spanwise profiles of the total turbulence intensity at two distances downstream the rotor. As concerns the vertical profiles, figure 5.40, the maximum value of the total turbulence intensity is not located at the top tip as in the non-stratified case, figure 5.12, since here the wake is subject to vertical meandering and is pushed downward by the above fluid. For this reason, the maximum level of turbulence

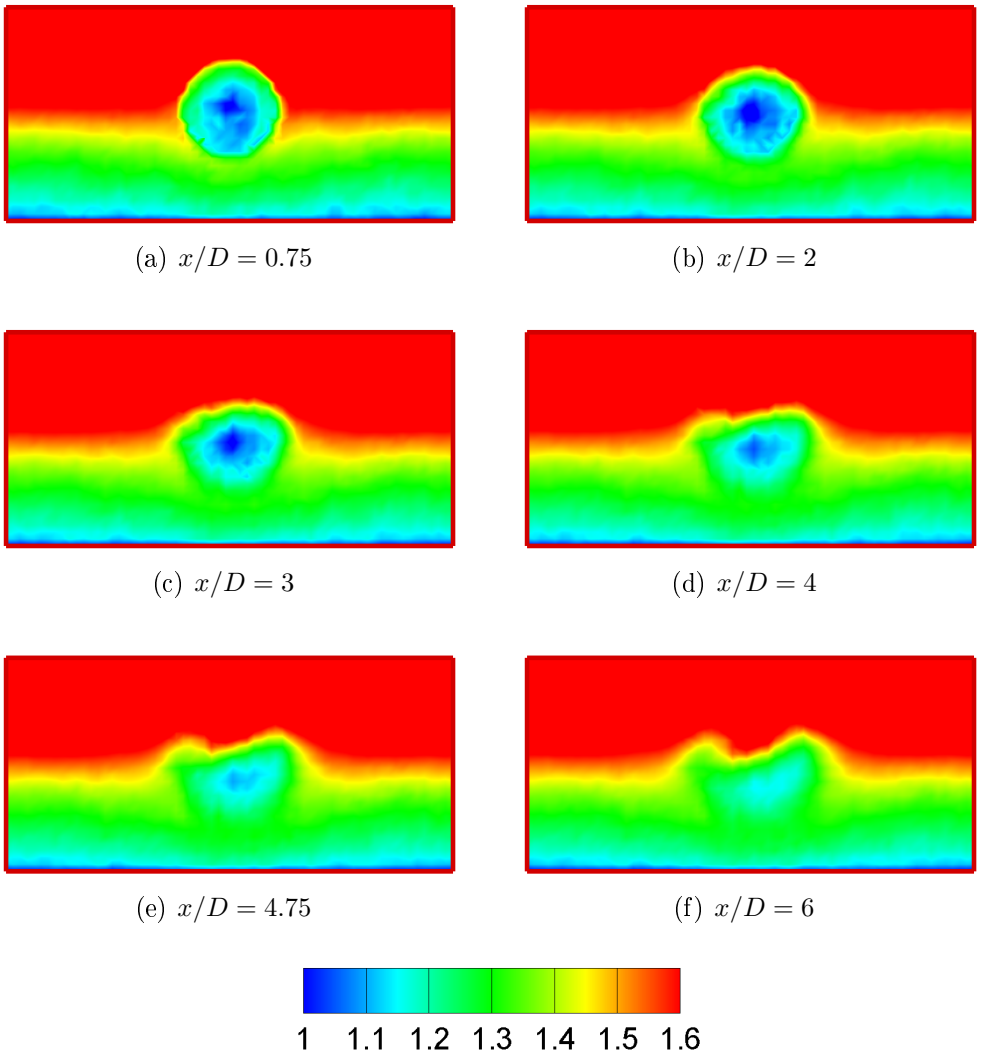

(a) $x/D = 0.75$ (b) $x/D = 2$

(c) $x/D = 3$ (d) $x/D = 4$

(e) $x/D = 4.75$ (f) $x/D = 6$

Figure 5.36: Contour plot of time averaged streamwise velocity U [m/s] for vertical transverse planes $(y - z)$, at different downstream distances, weak stratified condition.

intensity is located at a lower position. As regards the figure 5.41, the total turbulence intensity at x/D=1 shows a double peak at the top and bottom tip of the rotor respectively, as for the non-stratified case, figure 5.13; this behavior is related to the intense production of turbulent kinetic energy and associated high level of shear at those locations. The horizontal turbulence intensity is slightly higher than the vertical. In figures 5.42 and 5.43 we show respectively the contour plot of the $< u'v' >$ shear stress for a vertical plane and the contour plot of the shear stress component $< u'w' >$ for an horizontal plane. Figure 5.42 shows that immediately

beyond the rotor there is a momentum flux from the boundary layer toward the wake, this implies that the wake entrain fluid from the field located below. This is consistent with the fact that the wake is forced into a region (the lower part of the domain) where turbulence is sustained by the bottom wall and is more intense than the surrounding field. Farther downstream, the momentum flux is from the above field toward the wake and consequently the wake entrain mean kinetic energy from the above field. Figure 5.42 shows that the lateral shear stress is located at the edge of the wake. These results are consistent to the development of the wake showed in figures 5.34 and 5.35. Figures 5.44, 5.45 and 5.46 show, respectively, the contour plot of the non-dimensional mean density field for a vertical longitudinal plane, for an horizontal plane and for vertical transverse planes at difference downstream distances. From figure 5.44 it can be observed that beyond the turbine, the interface is subject to a mixing and it grows vertically. This phenomenon is ascribed to the wake impact on the field: lower density fluid is transported toward a region with higher density. This gives rise to instabilities at the interface. Instabilities grow till they overturn and break up mixing the two fluids, as illustrated in figure 5.46. Figure 5.47 shows the contour plot of the instantaneous non-dimensional density field for a vertical plane, where it can be seen the internal waves and the temperature mixing.

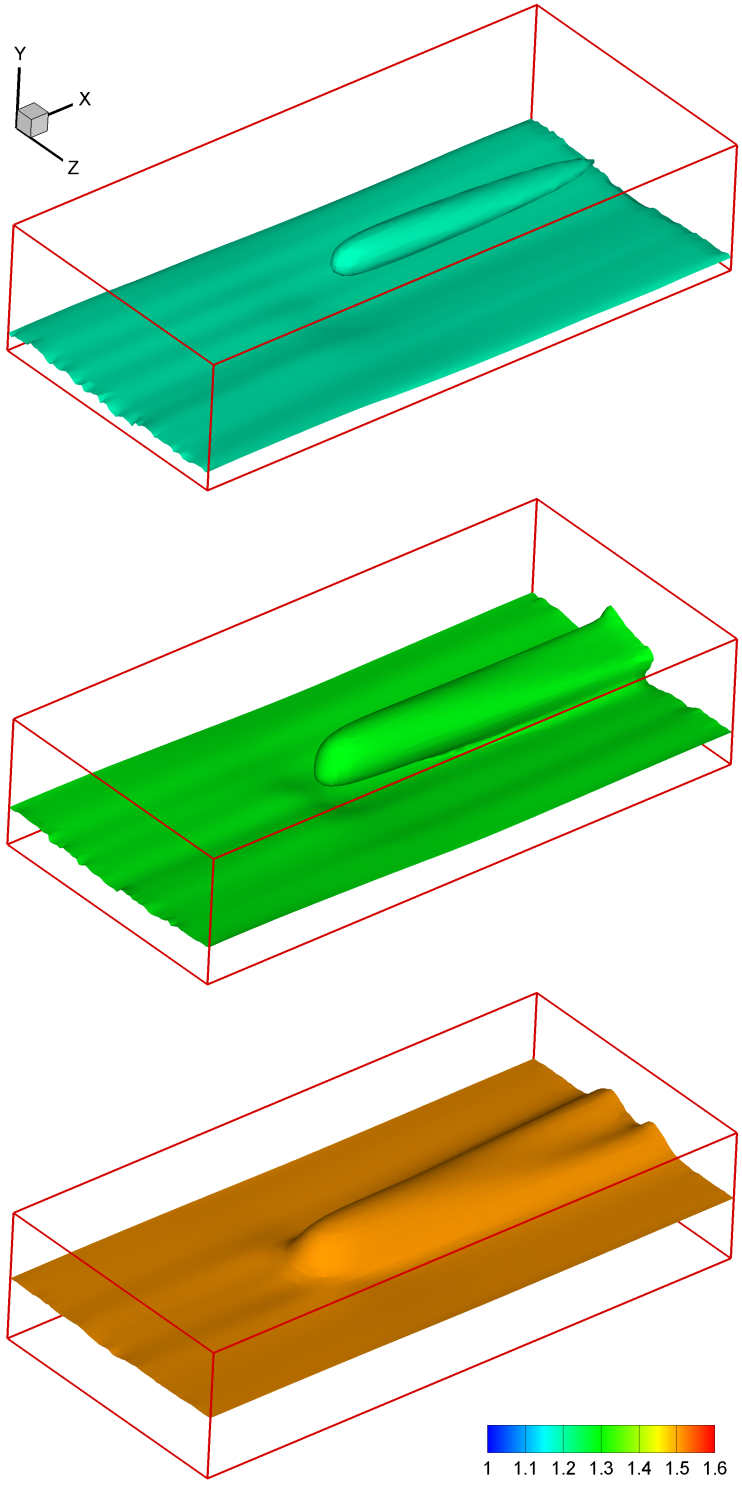

Figure 5.37: Iso-surfaces of time averaged streamwise velocity U [m/s], weak stratified condition. Top: 1.19 m/s, middle: 1.29 m/s and bottom: 1.51 m/s

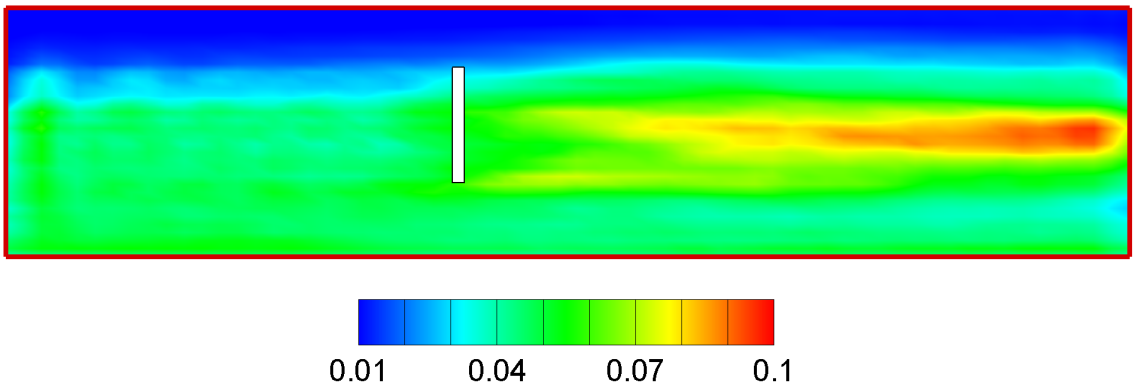

Figure 5.38: Contour plot of time averaged total turbulence intensity for a vertical longitudinal plane $(x - y)$ which crosses the turbine center, weak stratified condition.

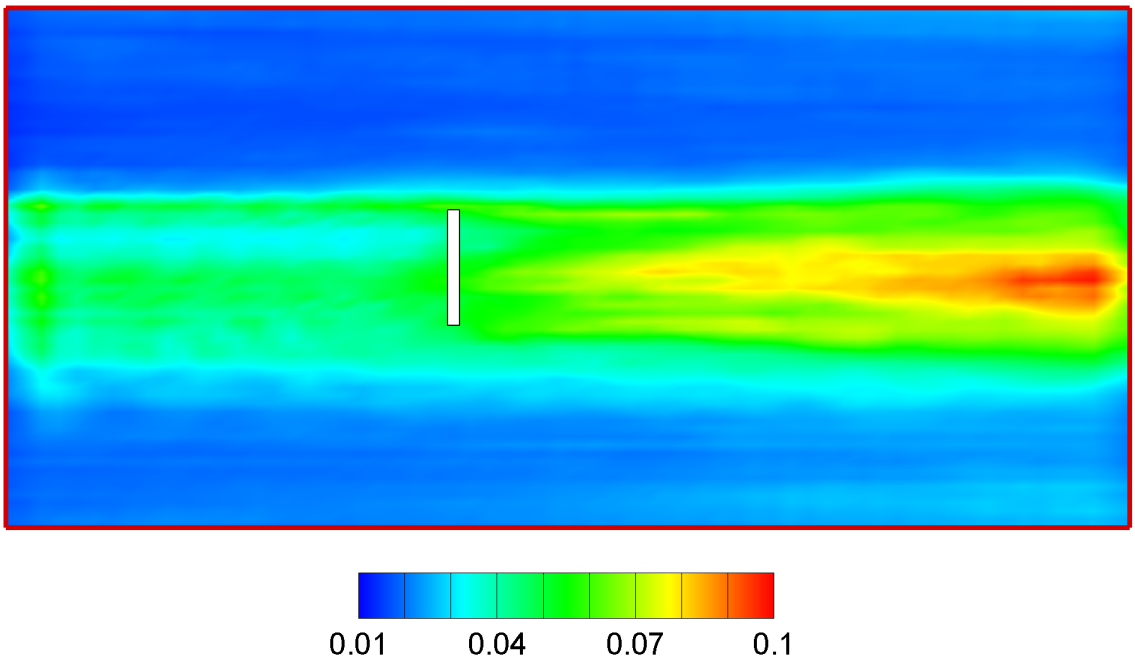

Figure 5.39: Contour plot of time averaged total turbulence intensity for an horizontal plane $(x - z)$ which crosses the turbine center, weak stratified condition.

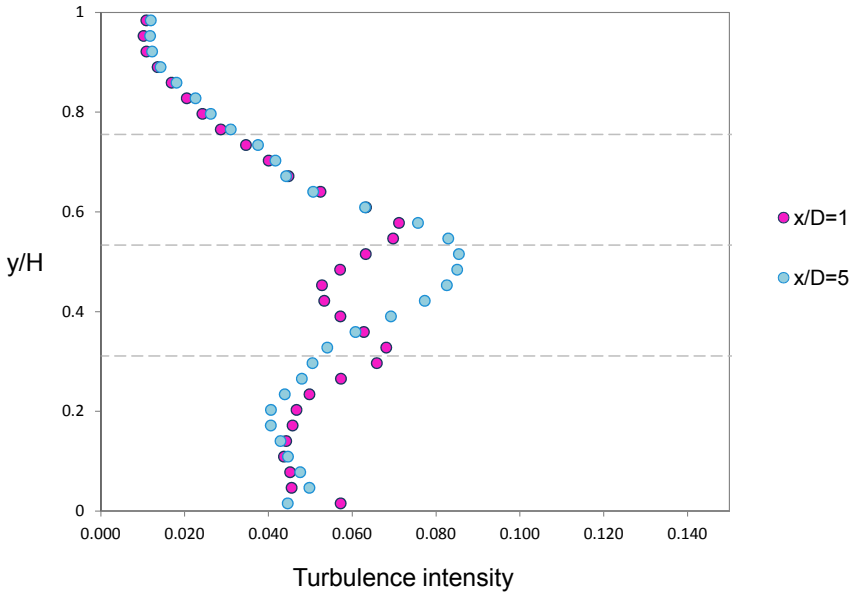

Figure 5.40: Vertical profiles of time averaged total turbulence intensity at two rotor distances for a vertical longitudinal plane that crosses the turbine center $(x-y)$, weak stratified condition.

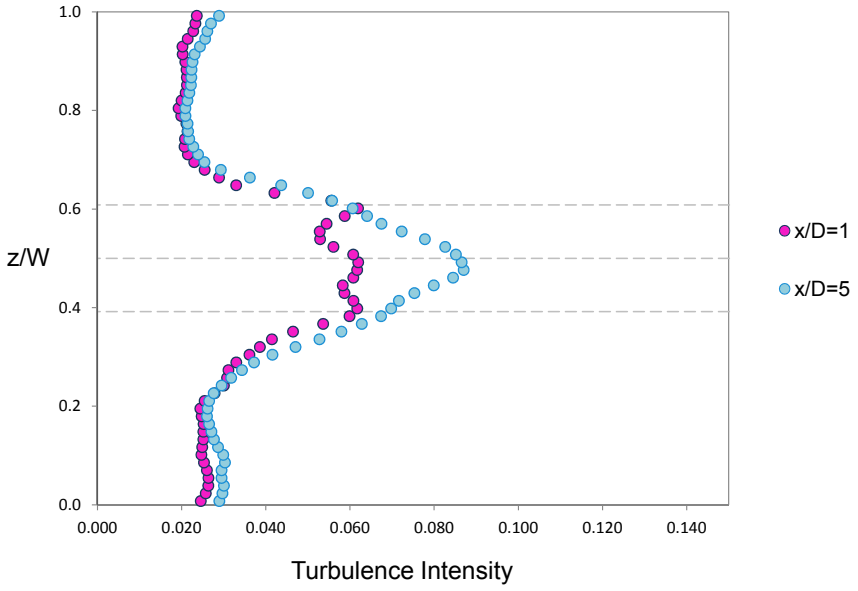

Figure 5.41: Transverse profiles of time averaged total turbulence intensity for an horizontal plane $(x-z)$ which crosses the turbine center, weak stratified condition.

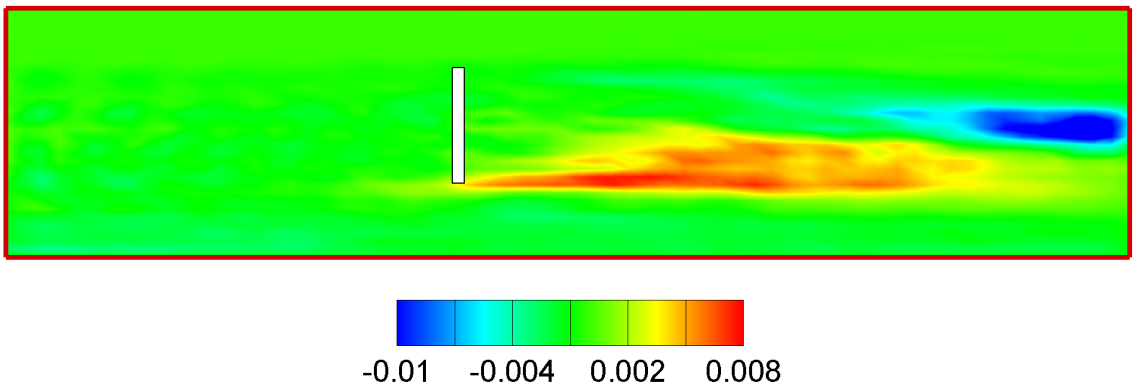

Figure 5.42: Contour plot of time averaged shear stress $< u'v' >$ for a vertical longitudinal plane $(x - y)$ which crosses the turbine center, weak stratified condition.

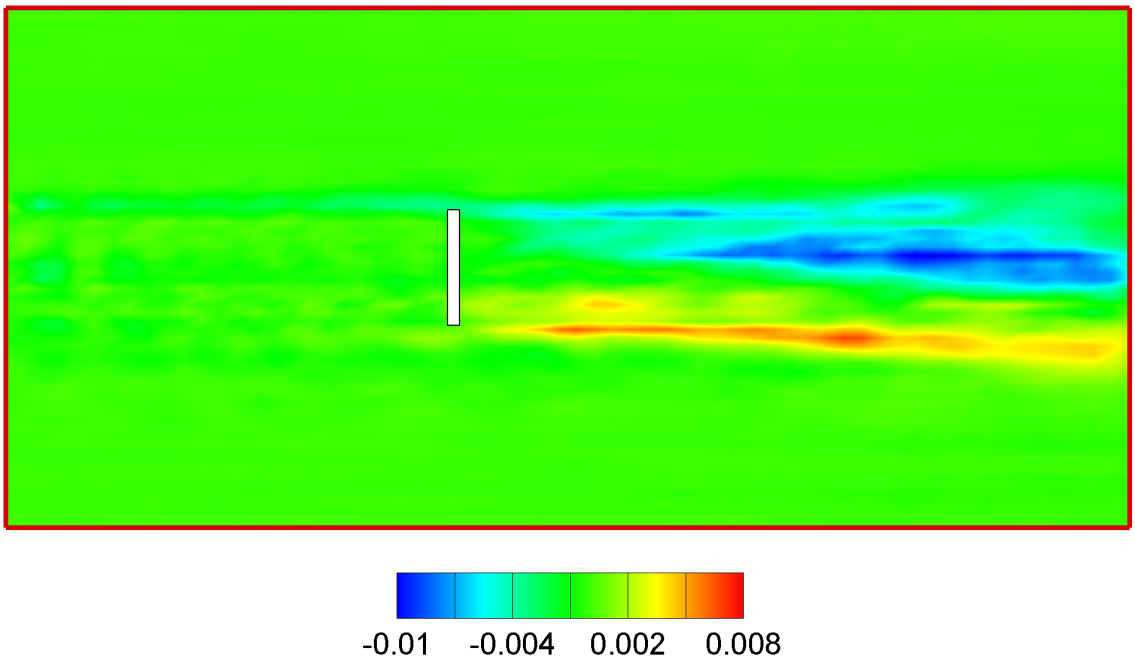

Figure 5.43: Contour plot of time averaged shear stress $< u'w' >$ for an horizontal plane $(x-z)$ which crosses the turbine center, weak stratified condition.

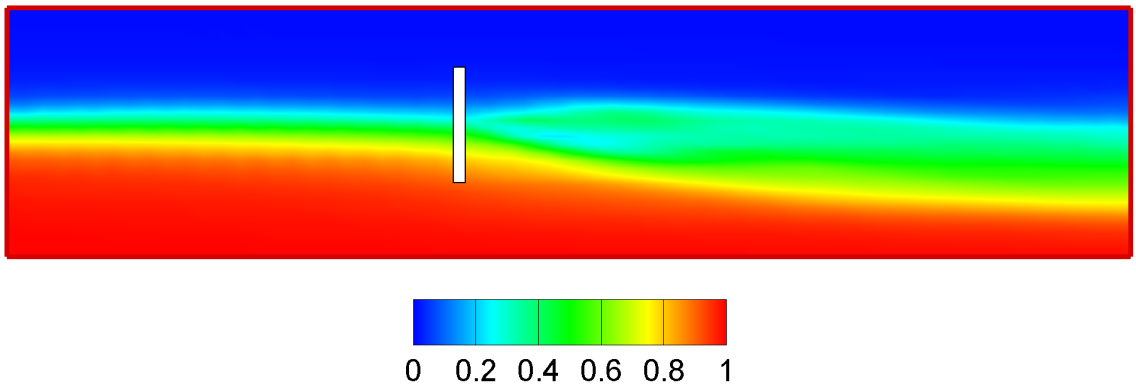

Figure 5.44: Contour plot of time averaged non-dimensional density for a vertical longitudinal plane $(x-y)$ which crosses the turbine center, weak stratified condition.

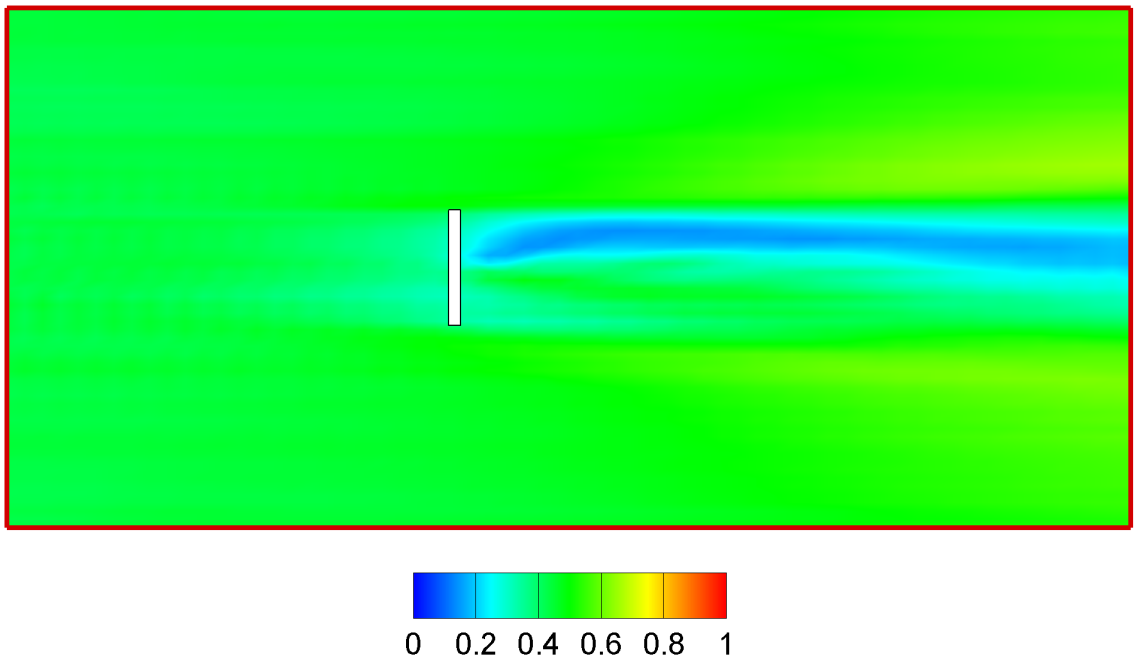

Figure 5.45: Contour plot of time averaged non-dimensional density for an horizontal plane $(x-z)$ which crosses the turbine center, weak stratified condition.

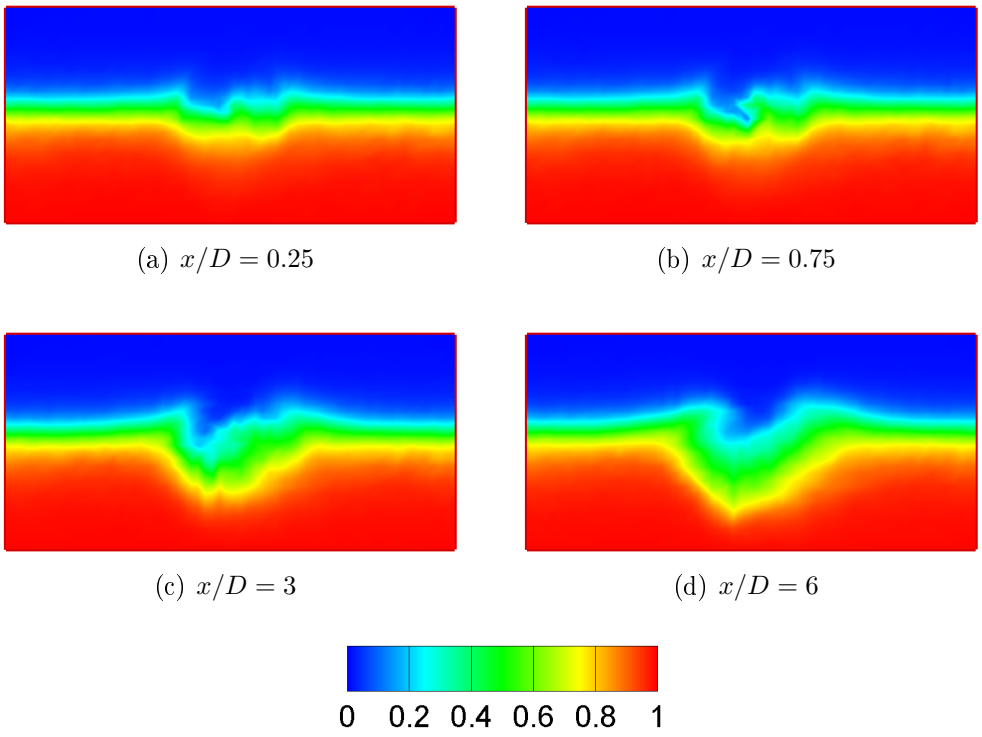

(a) $x/D = 0.25$ (b) $x/D = 0.75$

(c) $x/D = 3$ (d) $x/D = 6$

Figure 5.46: Contour plot of time averaged non-dimensional density for vertical transverse planes $(y-z)$ at different downstream distances, weak stratified condition.

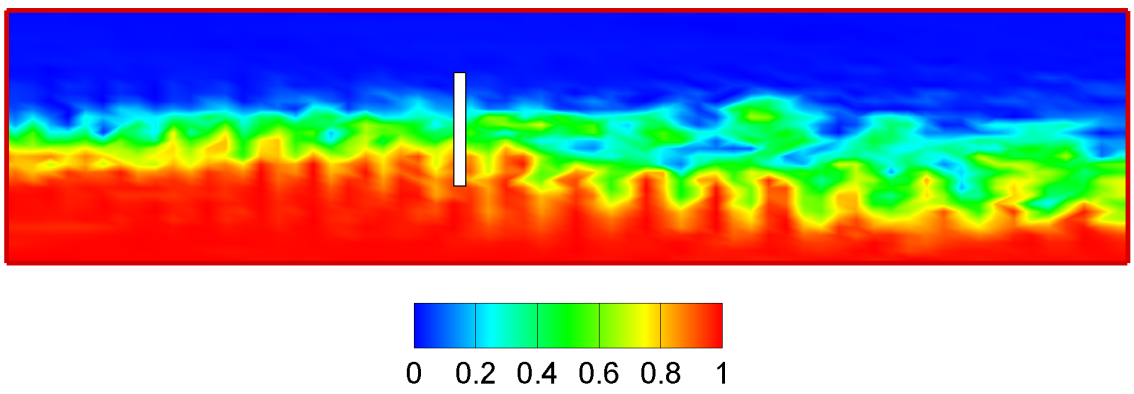

Figure 5.47: Contour plot of instantaneous non-dimensional density field for a vertical transverse plane (x-y) which crosses the turbine center, weak stratified condition.

5.4.2 Interaction between the turbine induced forces and the strong stratification

Subsequently to the simulation of the strong stratified case, the turbine was then introduced into the domain and a LES was performed coupled with the ADM-R model. The simulation was run for a non-dimensional time equal to $t = 80.2$, as for the non-stratified case and the weak stratified case. The statistics illustrated below have been calculated averaging the variables in time. Figures 5.48 and 5.49 show the contour plot of the time averaged streamwise velocity U respectively for a vertical and horizontal plane. The wake that forms behind the rotor loses its own typical shape (see the analogous contour plot for the non-stratified case of figure 5.4). Here, the wake is subject to the phenomena of meandering mentioned in section 5.4.1. This particular behavior of the wake can be explained because of the different relative speeds of the two layers. The stratification causes the development of two layers with different velocities, and the stronger stratification intensifies the relative motion between the two layers. Figure 5.50 shows the contour plot of the instantaneous velocity field and the velocity vectors which can help to understand the flow dynamics depicted in figure 5.48. Looking at the figures 5.48 and 5.50,

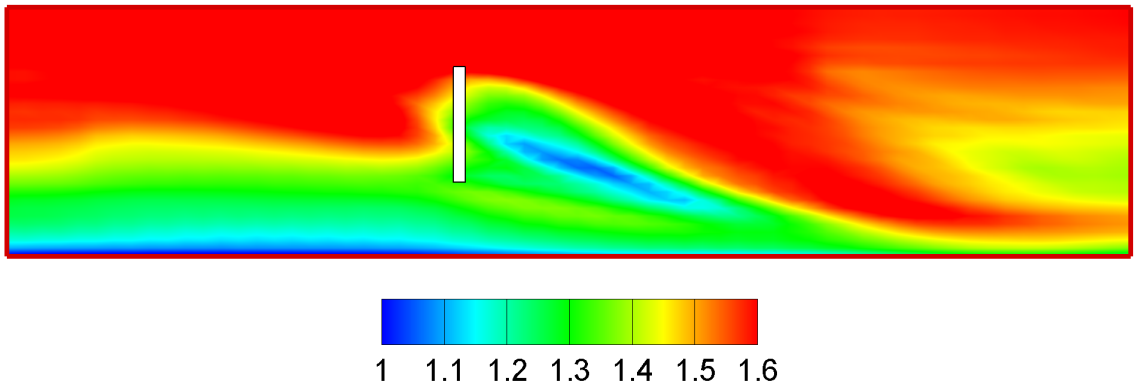

Figure 5.48: Contour plot of time averaged streamwise velocity U [m/s] for a vertical longitudinal plane $(x - y)$ which crosses the turbine center, strong stratified condition.

we observe that when the freestream fluid of top layer reaches and goes beyond the turbine location, it finds the wake that moves at a slower velocity. Since the top fluid bumps into a fluid much slower in a region where the fluid should be faster, it is forced to glide over the surface of the wake pushing the wake downward. Figure 5.51 shows the contour plot of the time averaged streamwise velocity U for vertical spanwise planes at different downstream distances. From figure 5.51 it can be observed that as the faster fluid penetrates the bottom layer, an eddy forms and entrains the fluid of the top layer. The eddy blends the fluid of the bottom layer into

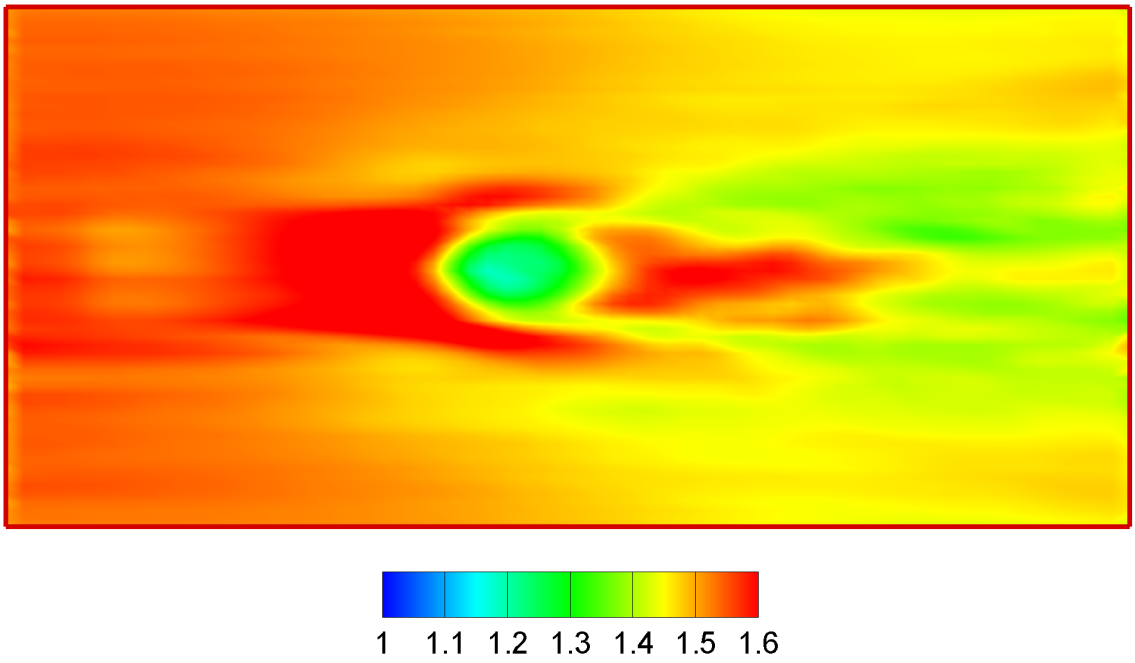

Figure 5.49: Contour plot of time averaged streamwise velocity U [m/s] for an horizontal plane $(x-k)$ which crosses the turbine center, strong stratified condition.

the fluid of top layer that previously penetrated the bottom layer. In figure 5.52, the velocity vectors are plotted for vertical planes at two downstream distances, where the eddy is evident. From figure 5.52, it can be seen that as we move downward the eddy enlarges and the mixing between the two fluids increases. This process of mixing increases instabilities and generates large waves at the interface. Figure 5.53 shows three streamwise velocities iso-surfaces which highlights the three dimensional deformation of the wake. Compared to the weak stratified case, it can be noticed that the lateral deformation of the wake is more pronounced. Immediately beyond the rotor, the increase of stratification prevents the wake to grow vertically toward the top of the domain. Moreover looking at the 1.32 m/s iso-surface the vertical meandering of the wake and the decreases of velocities are well captured.

In order to analyze the behavior of the turbulence intensity, figures 5.54 and 5.55 show the total turbulence intensity respectively for a vertical and a horizontal plane. Figure 5.54 shows that the region where total turbulence intensity has maximum values is located downstream the rotor in the lower part of the domain, as it can be seen also from figure 5.56 for $x/D = 5$. Here the wake, pushed downward by the faster fluid, entrains the surrounding field. In figure 5.55 it can noticed that the maximum total turbulence intensity has maximum values at the edge of the

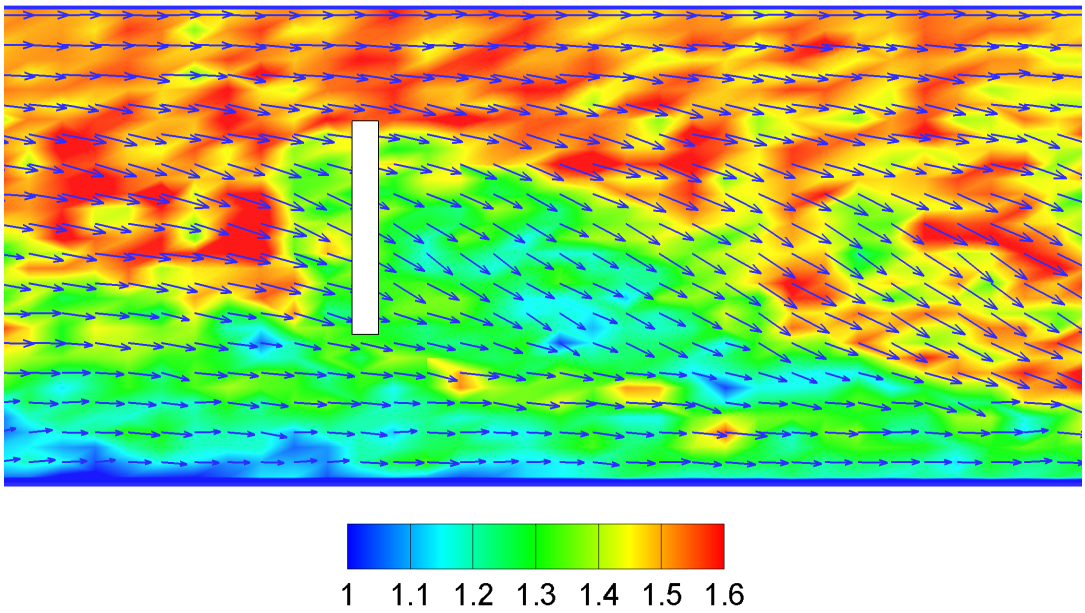

Figure 5.50: Contour plot of instantaneous streamwise velocity field and projection of velocity vectors on a vertical longitudinal plane $(x-y)$, which crosses the turbine center, strong stratified condition.

wake. This behavior already seen in particular for the non-stratified case, figure 5.13, can be observed in detail in figure 5.57, where the transverse profiles of total turbulence intensity are plotted for two different downstream distances. Comparing figures 5.54 and 5.55, we can deduce that the horizontal turbulence intensity is higher than the vertical. The high level of turbulence intensity can be associated to the intense production of turbulent kinetic energy and turbulent mixing, which are more intense laterally compared to the vertical direction. In figures 5.58 and 5.59 we show respectively the contour plot of the $< u'v' >$ shear stress for a vertical plane and the contour plot of $< u'w' >$ shear stress for an horizontal plane. In this case the analysis of the shear stresses is more difficult since the wake of the turbine is subject to a strong vertical meandering. As mentioned before, these quantities are responsible for the entrainment of mean kinetic energy into the wake. Because of the development of the eddy that mixes the rotor's wake with the faster fluid, there is a strong exchange of momentum flux and entrainment, as can be seen from figures 5.58 and 5.59. Besides the analysis of the velocity field, we want now to evaluate the impact of the turbine induced forces on the density field in case of strong stable stratified condition. Looking at figure 5.60, where the contour plot of time averaged non-dimensional density for a vertical plane is displayed, we observed that the density step is subject to mixing due to the presence of the turbine. This result was expected from the analysis of the mean velocity since the faster fluid which has a lower density,

sliding over the wake brings the lower density fluid into the region of high density fluid. Substantially the turbulent eddy raises dense fluid above the less dense fluid. The development of the eddy and the consequent overturn accelerated the mixing process. Figure 5.61 shows the contour plot of mean non-dimensional density for vertical planes at different downstream positions, where it can be observed that the mixing region expands as we move downward. Moreover, the maximum vertical mixing takes place at the center of the wake. Figures 5.62 and 5.63 show respectively the contour plot of the instantaneous field for a vertical longitudinal plane and for transverse planes localized at different downstream distances. From the analysis of the instantaneous field it can be observed the intense local instabilities that lie at the interface between the two layers which are subject to mixing.

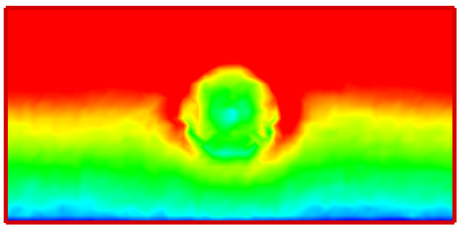

(a) $x/D = 0.25$

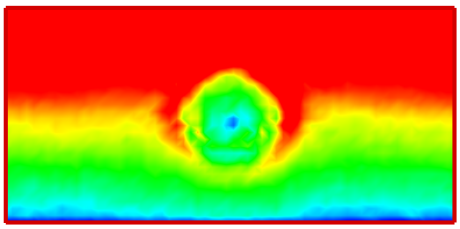

(b) $x/D = 0.5$

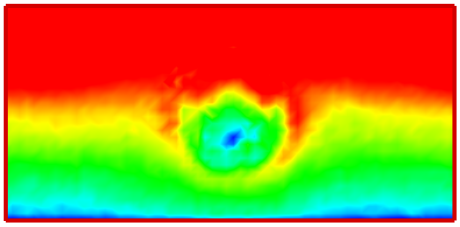

(c) $x/D = 1$

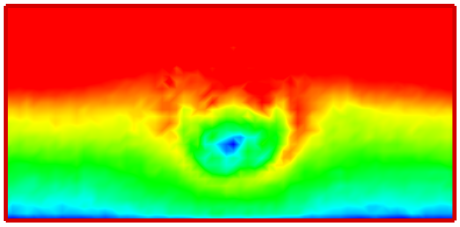

(d) $x/D = 1.25$

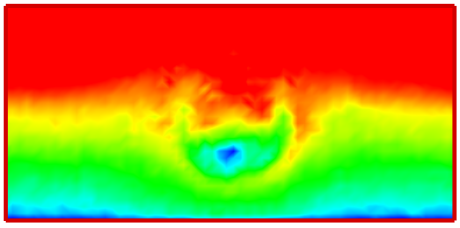

(e) $x/D = 1.5$

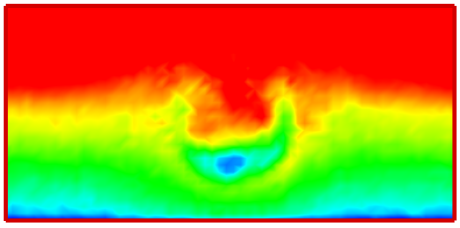

(f) $x/D = 1.75$

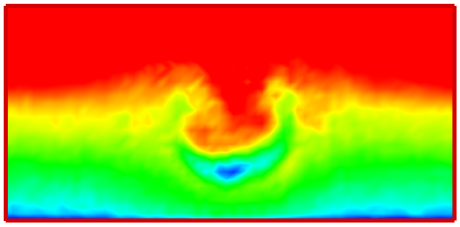

(g) $x/D = 2$

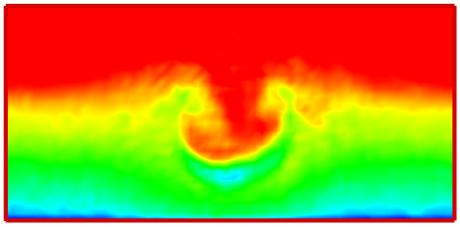

(h) $x/D = 2.25$

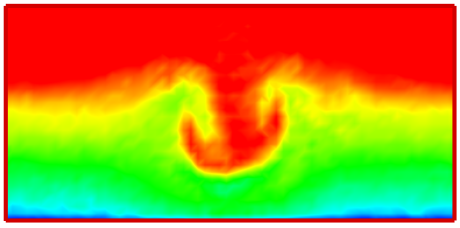

(i) $x/D = 2.75$

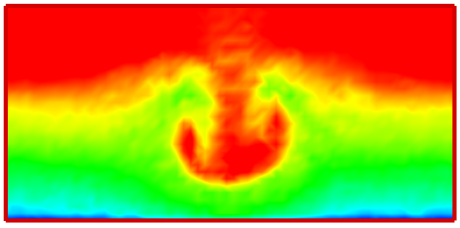

(j) $x/D = 3.25$

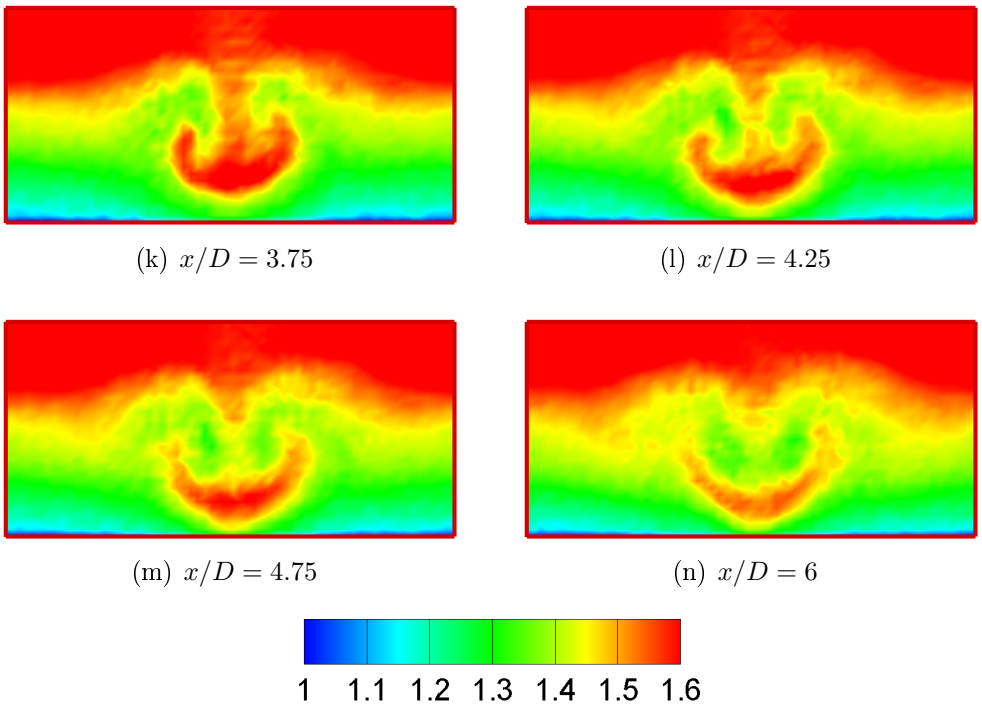

(k) $x/D = 3.75$ (l) $x/D = 4.25$

(m) $x/D = 4.75$ (n) $x/D = 6$

Figure 5.51: Contour plot of time averaged streamwise velocity U [m/s] for vertical transverse planes $(y - z)$, strong stratified condition.

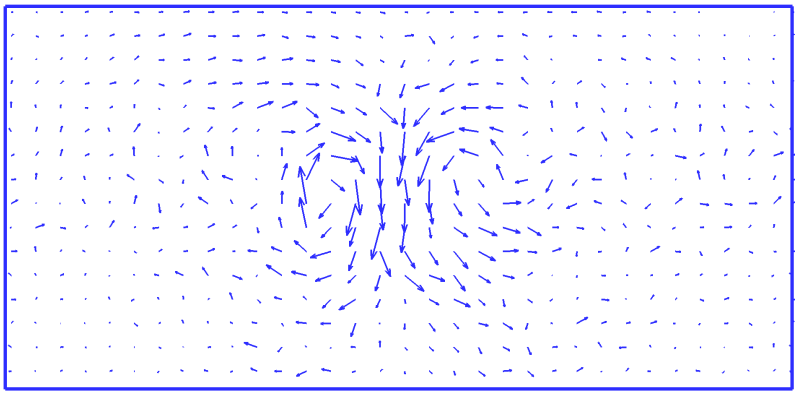

(a) $x/D = 0.77$

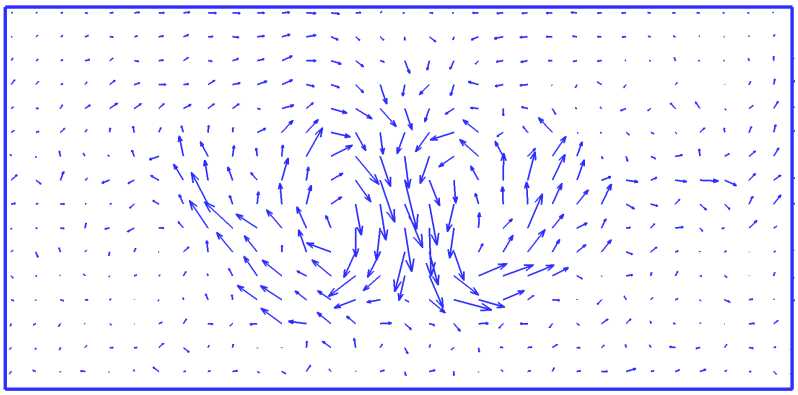

(b) $x/D = 2.25$

Figure 5.52: Projection of instantaneous velocity vectors on vertical transverse planes $(y - k)$, strong stratified condition.

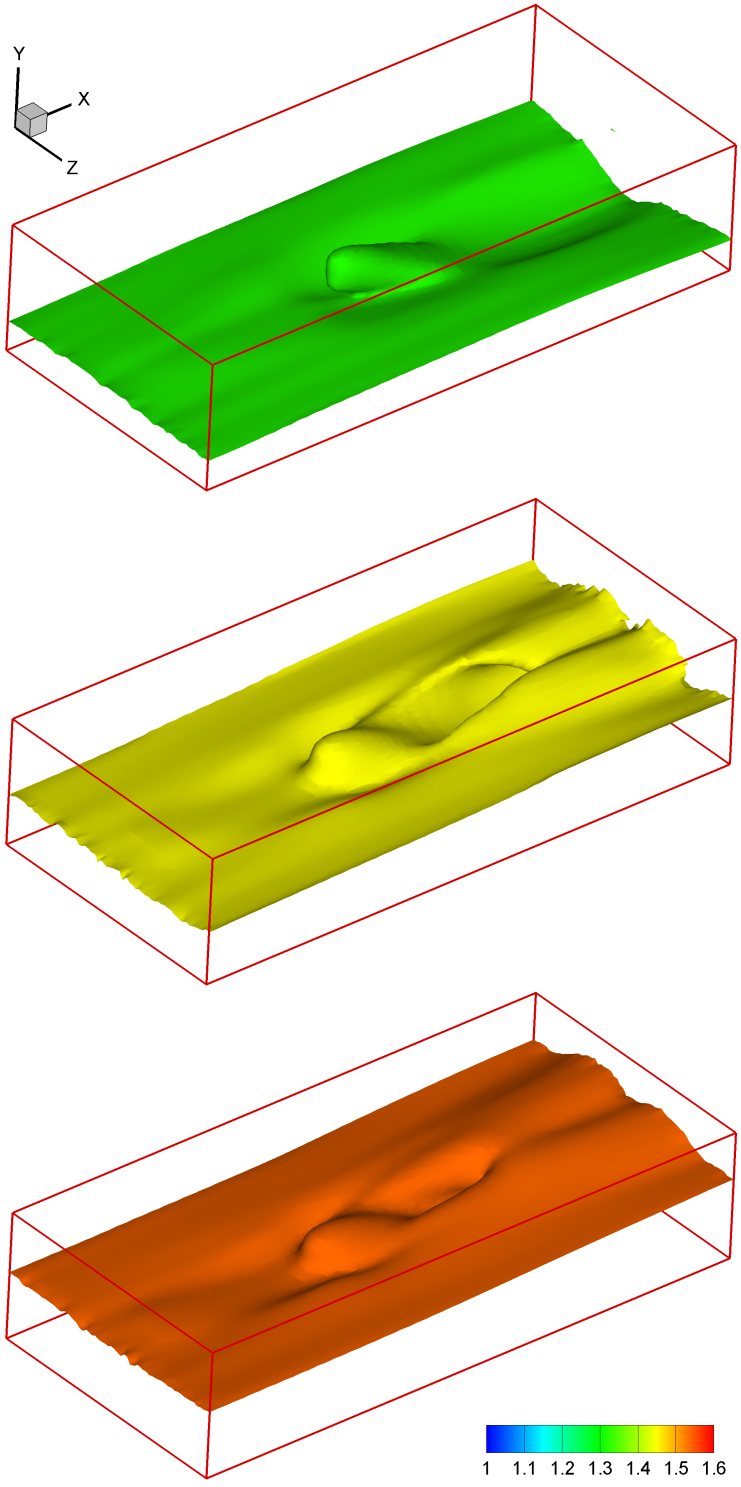

Figure 5.53: Iso-surfaces of time averaged streamwise velocity U [m/s], strong stratified condition. Top: 1.32 m/s, middle: 1.45 m/s and bottom: 1.54 m/s

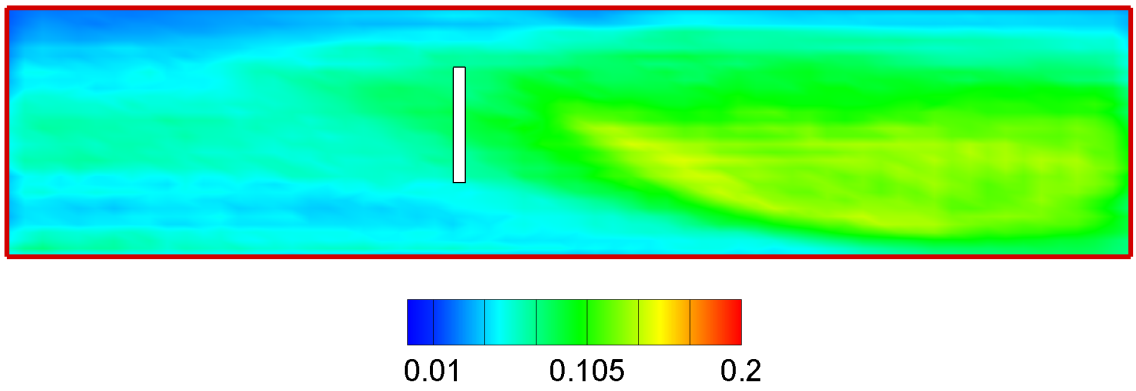

Figure 5.54: Contour plot of time averaged total turbulence intensity for a vertical longitudinal plane $(x - y)$ which crosses the turbine center, strong stratified condition.

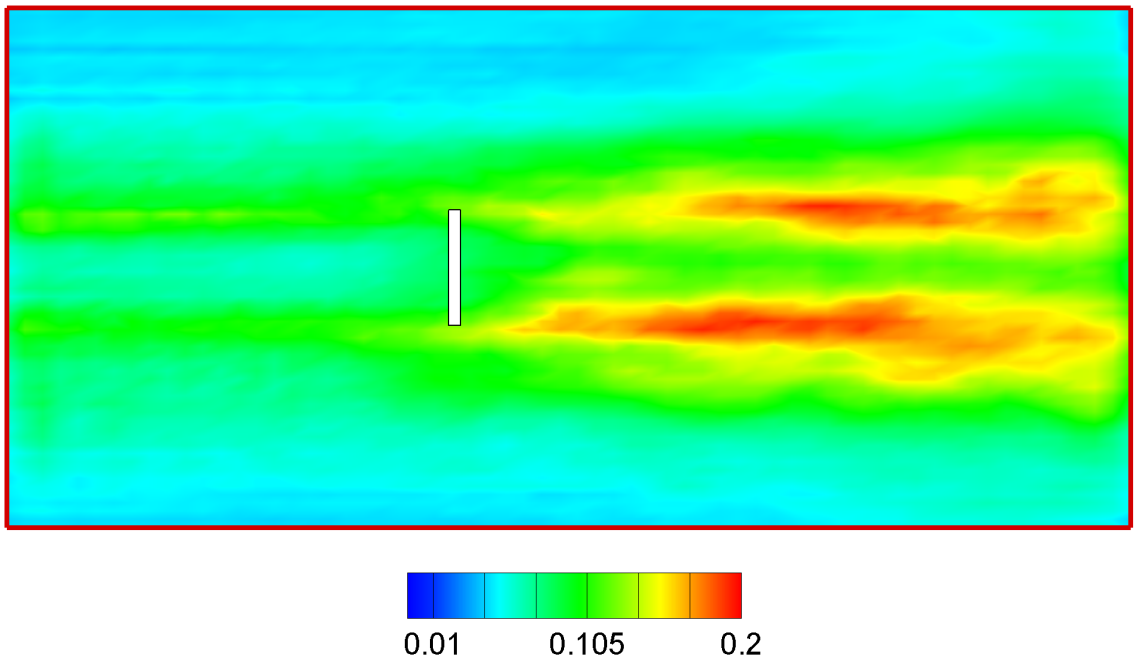

Figure 5.55: Contour plot of time averaged total turbulence intensity for an horizontal plane $(x - z)$ which crosses the turbine center, strong stratified condition.

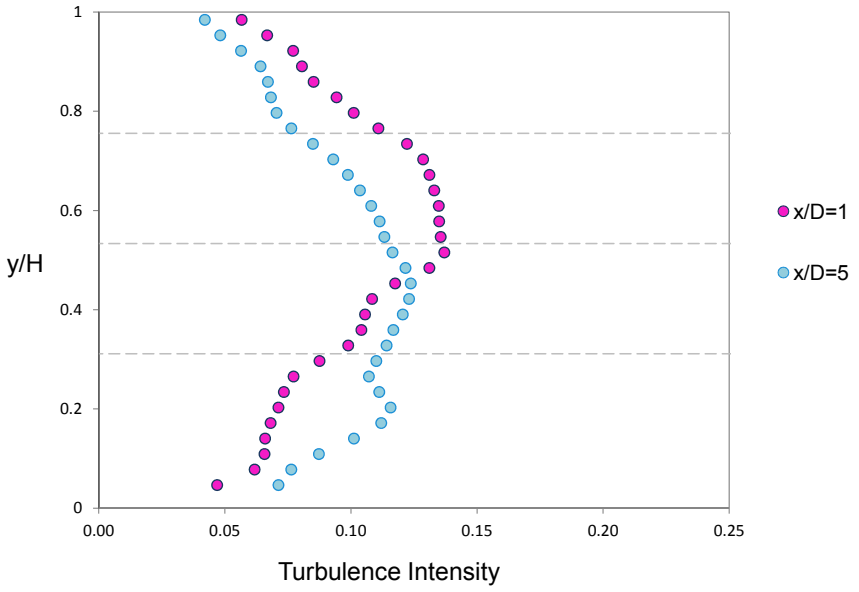

Figure 5.56: Vertical profiles of time averaged total turbulence intensity at two rotor distances for a vertical longitudinal plane that crosses the turbine center $(x - y)$, strong stratified condition.

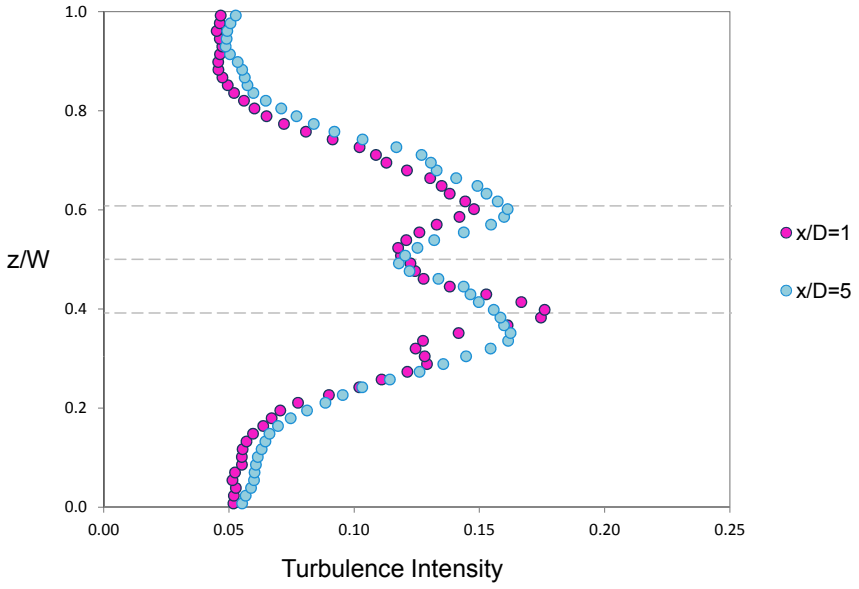

Figure 5.57: Transverse profiles of time averaged total turbulence intensity at two rotor distances for an horizontal plane $(x-k)$ which crosses the turbine center, strong stratified condition.

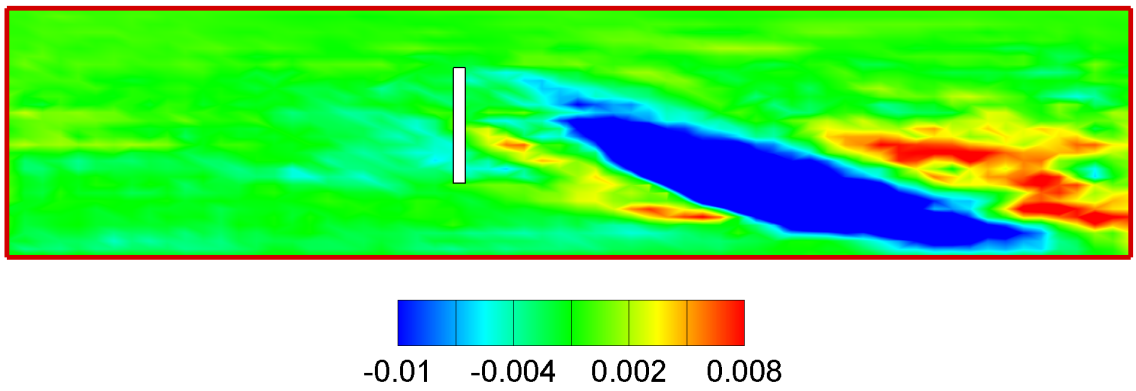

Figure 5.58: Contour plot of time averaged shear stress $< u'v' >$ for a vertical longitudinal plane $(x-y)$ which crosses the turbine center, strong stratified condition.

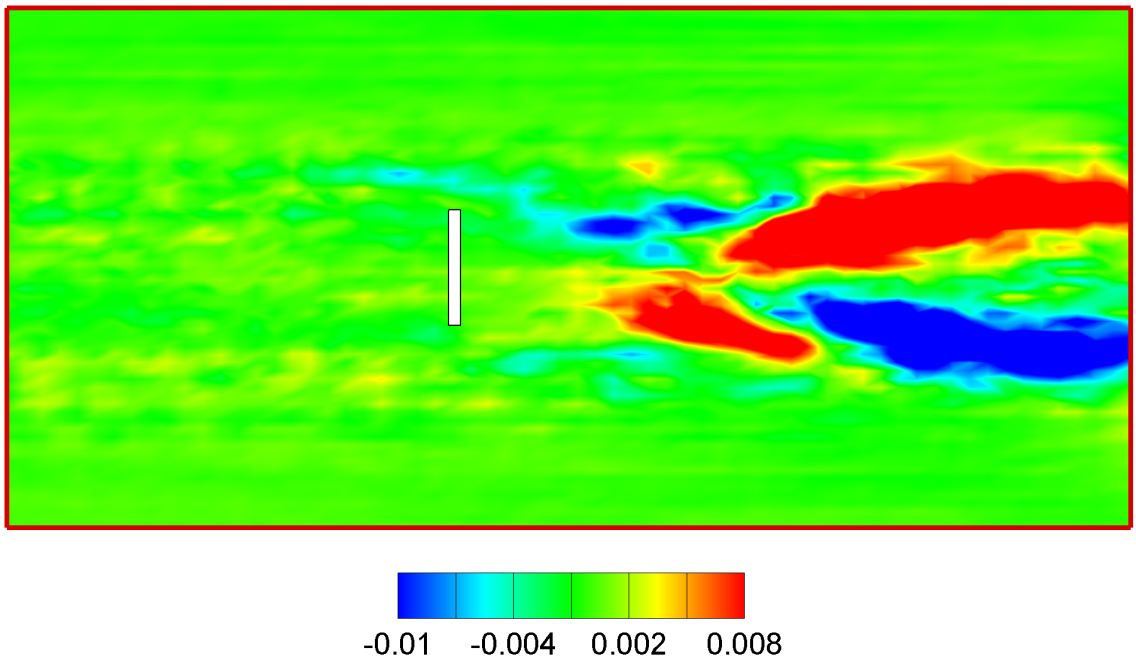

Figure 5.59: Contour plot of time averaged shear stress $< u'w' >$ for an horizontal plane $(x-z)$, strong stratified condition.

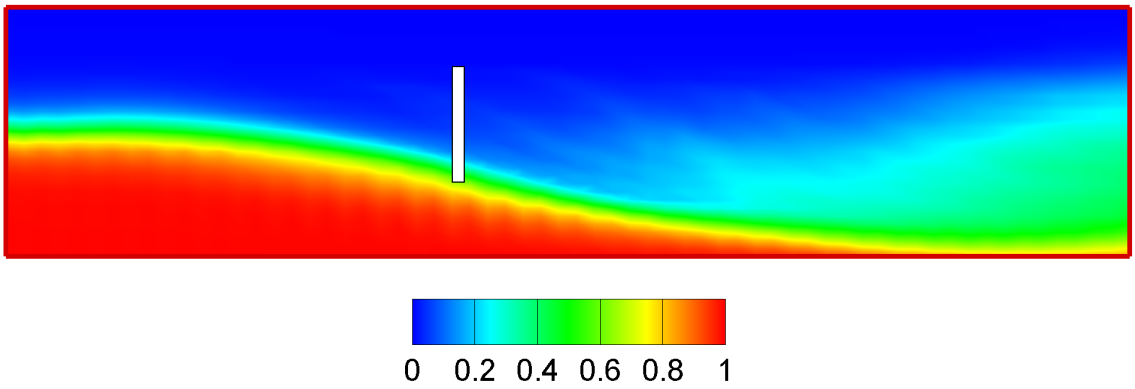

Figure 5.60: Contour plot of time averaged non dimensional density for a vertical longitudinal plane $(y-z)$ which crosses the turbine center, strong stratified condition.

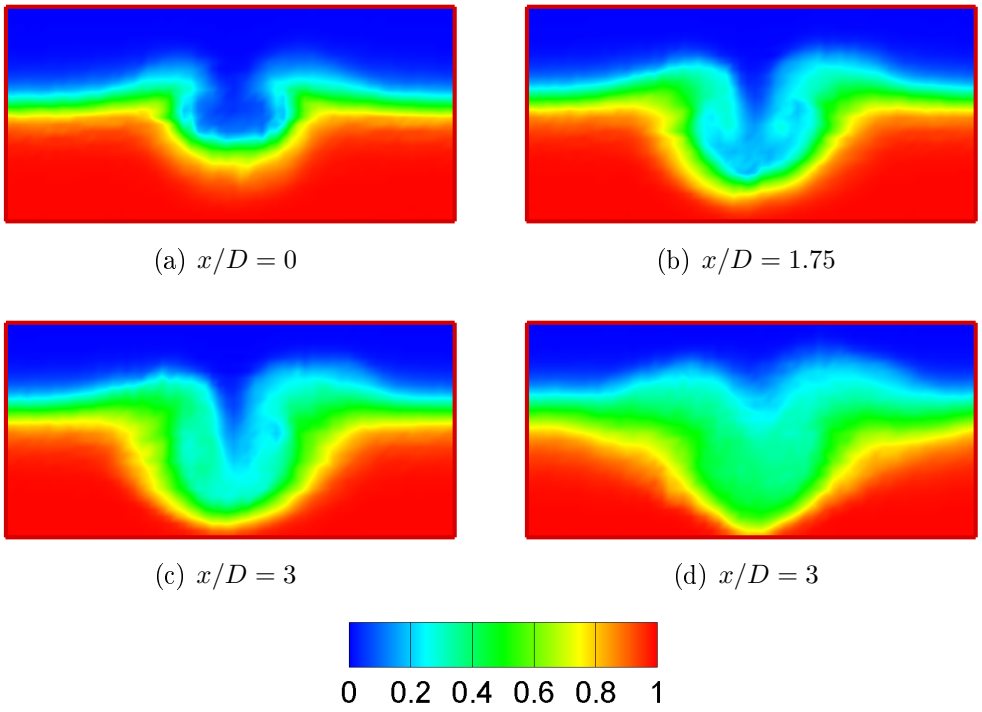

(a) $x/D = 0$ (b) $x/D = 1.75$

(c) $x/D = 3$ (d) $x/D = 3$

Figure 5.61: Contour plot of time averaged non-dimensional density for vertical transverse planes $(y - z)$ at different downstream distances, strong stratified condition.

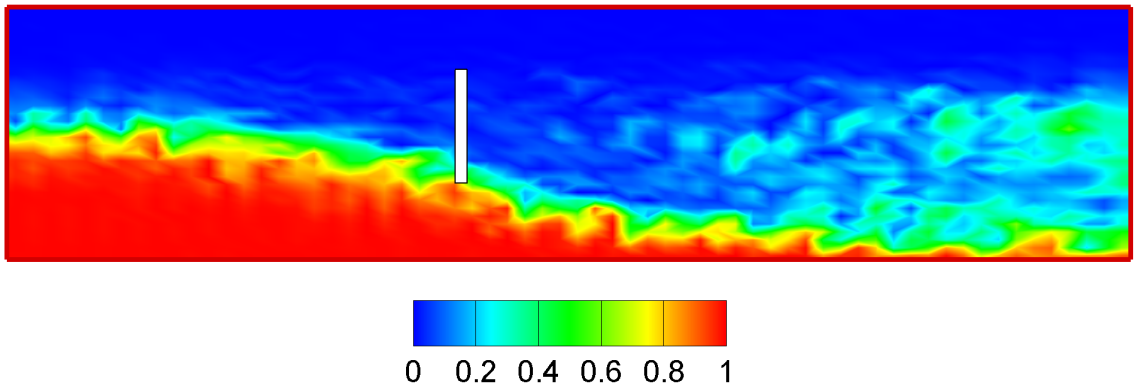

Figure 5.62: Contour plot of instantaneous non-dimensional density field for a vertical plane $(y - z)$ which crosses the turbine center, strong stratified condition.

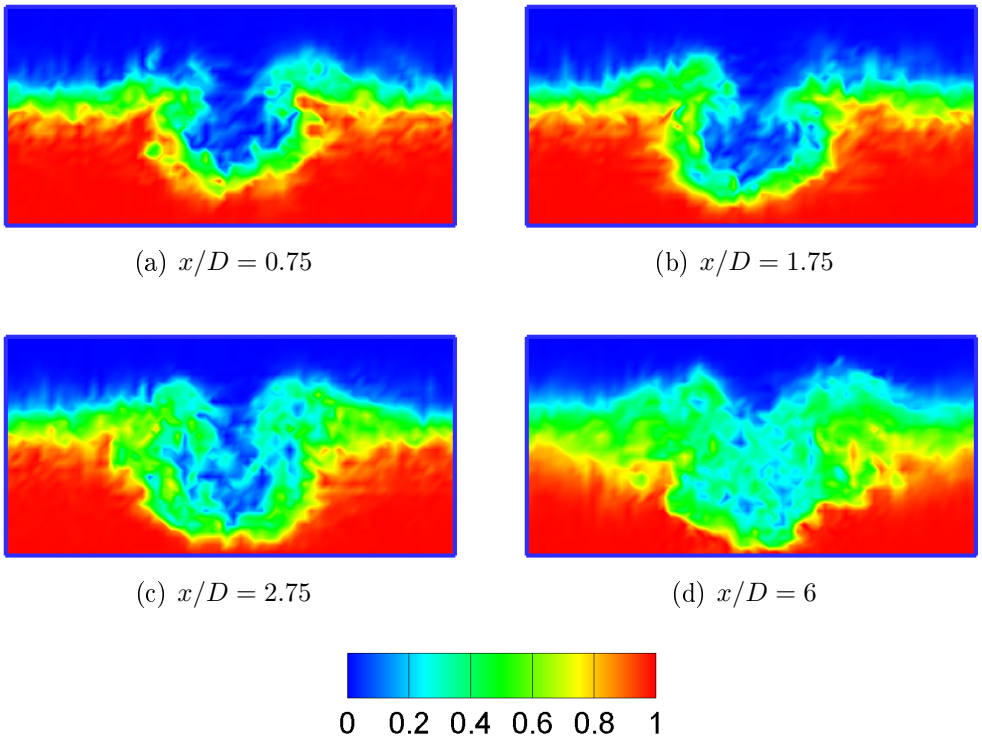

(a) $x/D = 0.75$ (b) $x/D = 1.75$

(c) $x/D = 2.75$ (d) $x/D = 6$

Figure 5.63: Contour plot of time averaged non-dimensional density for vertical transverse planes $(y - z)$ at different downstream distances, strong stratified condition.

5.5 Comparison of the results

In this section a comparison between the impact of the weak and the strong stratification on power performance and wake characteristics will be carried out. The power that can be extracted has been computed for the two stratification cases. For the weak stratified case, the power obtained is equal to 333 W and the power coefficient is $C_P = 0.358$. Instead, for the strong stratification, the power is equal to 373.3 W and the power coefficient is $C_P = 0.365$. The turbine produces more energy in case of strong stratification since velocities increase more than in the weak stratification case. This is particularly true if we compare the strong stratified case with the non-stratified case where the difference amounts to 28%. The main result is that comparing the turbine performance in terms of power coefficient for the two stratification cases, it turns out that the power coefficient is not subject to substantial changes, actually it experiences a relative increase of 2%. If we compare the power coefficient of the non-stratified case with the strong stratified case, it experiences a slight increase of 4%. Analyzing the mean streamwise velocity, we observe that in the case of weak stratification the wake is subject to a moderate vertical meandering. The wake entrainment is supplied mainly from the underneath and lateral flow field. Instead, in case of strong stratification, the vertical shifting of the wake center is rather remarkable. The wake is pushed downward and the fluid

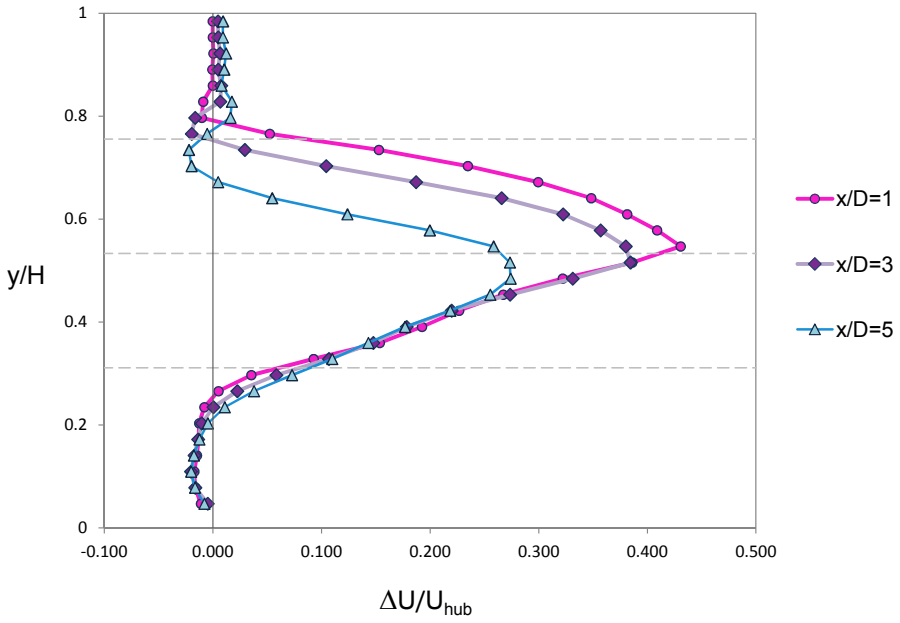

Figure 5.64: Non-dimensional velocity deficit profiles at different downstream distances from the rotor, for a vertical plane across the turbine center, weak stratification.

is mixed by a large scale eddy. From the comparison of the contour plot of the mean streamwise velocity, figures 5.34 and 5.48, we observe that the wake recovers faster in the case of strong stable stratified condition. This result is confirmed analyzing the non-dimensional velocity deficit for the weak stratified case and for the strong stratification. Figures 5.64 and 5.65 show the non dimensional velocity deficit profiles for the weak stratified case respectively for a vertical plane and for an horizontal plane. The profiles in figures 5.64 and 5.65 refer to specific distances downstream the rotor. As we move downstream, the velocity deficit reduces gradually and recovers from 0.431 at a distance of $x/D = 1$, up to 0.260 at a distance of $x/D = 5$. The non-dimensional velocity deficit profiles for the strong stratification case are shown in figures 5.66 and 5.67, respectively for a vertical and for an horizontal plane. From figure 5.66 we observe that velocity recovers quickly and increases near the bottom as expected from figure 5.51, since the faster fluid sliding toward the bottom is mixed by means of the eddy into the slower fluid. At $x/D = 1$ the maximum velocity deficit is equal to 0.218 and at $x/D = 5$ is 0.073. Therefore a remarkable difference between the weak and the strong stratified cases is detected as regards the velocity deficit recover. The faster recover of the wake in the case of strong stratification is consistent with the analysis of turbulence intensity. In fact the turbulence intensity of the strong case, figures 5.54 and 5.55, is higher than the

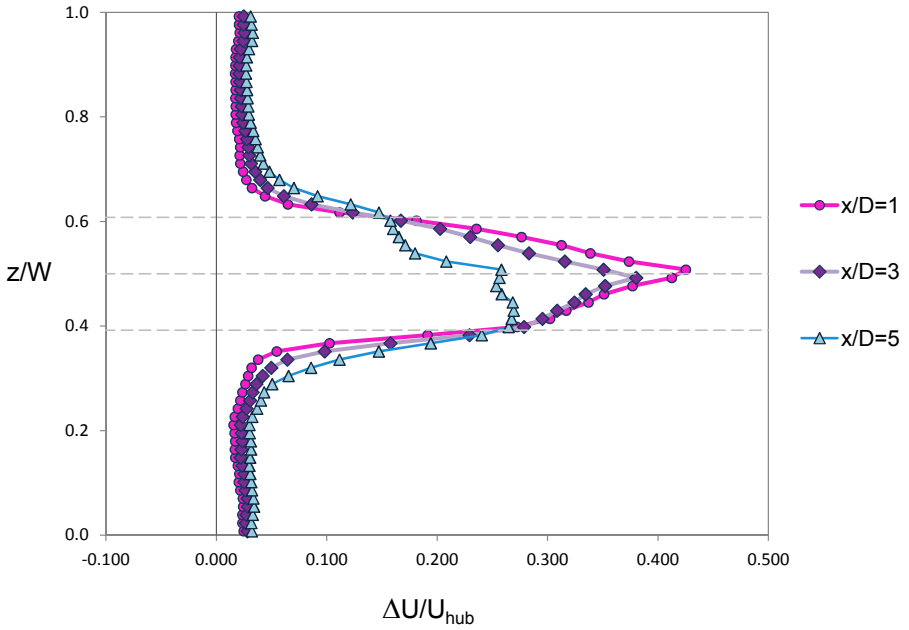

Figure 5.65: Non-dimensional velocity deficit profiles at different downstream distances from the rotor, for an horizontal plane across the turbine center, weak stratification.

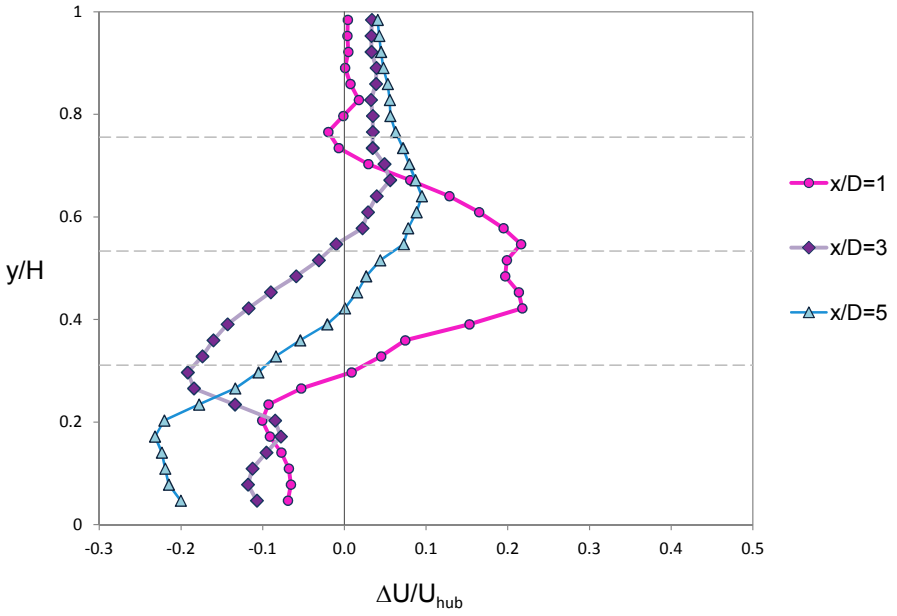

Figure 5.66: Non-dimensional velocity deficit profiles at different downstream distances from the rotor, for a vertical plane across the turbine center, strong stratification.

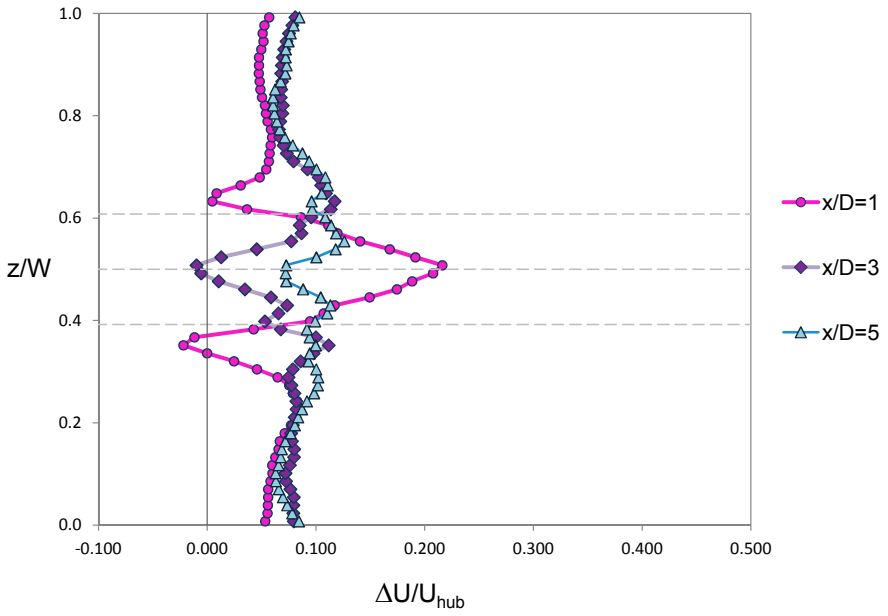

Figure 5.67: Non-dimensional velocity deficit profiles at different downstream distances from the rotor, for an horizontal plane across the turbine center, strong stratification.

turbulence intensity of the weak stratified case, figures 5.38 and 5.39. The same holds for the shear stress which is higher for the strong case, figures 5.58 and 5.59, compared to the weak case, figures 5.42 and 5.43. Finally, it clearly appears that the density mixing is more intense in case of strong stratification; this is consistent with the results previously analyzed.

Chapter 6

Conclusions

The present study was mainly focused on the evaluation of the impact of marine stable stratification on turbine performance and wake characteristics. Stratification can characterize the sites where turbines are installed, this is the case of estuarine basins and shelf seas where marine stratification is an important factor for the marine environment dynamics. For this reason and also because the effects of marine density stratification is an issue that hasn't been yet investigated, there was the need to provide an insight on the interaction between the turbine and stable stratified conditions.

The present study was carried out by means of LES, in particular simulations were performed using the in-house LES-COAST model which solves the filtered form of three dimensional Navier-Stokes equations and the two equations for temperature and salinity. The capability of LES-COAST in describing the phenomena of coastal areas under stratified conditions have been demonstrated by literature. LES methodology is nowadays a powerful tool in the investigation of detailed turbulent flows, in particular turbulence is significantly in the wake of turbines and moreover turbulence intensity plays an important role in wake development. The LES-COAST model is coupled with a module for the turbine which computes the turbine induced forces. To model the normal and tangential forces that the turbine generates, we employed the ADM-R model, which takes into account the rotation of the wake downstream the rotor. Forces computed through the ADM-R model are then applied to the flow field as a body force. The ADM-R was validated using experimental data supplied by literature. From the comparison between numerical results and experimental data, it has been proved the capability of the model in reproducing the thrust and power characteristics of a turbine. In order to evaluate the interaction between the turbine and the stratification, two types of stable stratified conditions have been simulated: a weak and a strong stratified condition. The weak stratification has been simulated imposing a temperature jump in order

to obtain a vertical density profile with a step shape. The same has been done for the strong stratification, but imposing a salinity jump which gives rise to higher density variation compared to the weak case. Then the turbine was introduced into the stratified fields. We also performed a simulation of a turbine in a non-stratified field, which has been used as a benchmark for the analysis of the interaction between the turbine and the two stratified cases. Finally the results of the non-stratified case and the two stratified cases have been analyzed and compared.

As regards the power efficiency, the main outcome is that the power coefficient is not subject to substantial variations, actually it experiences an increase of 2% between the weak and the strong stratification cases. Comparing the power coefficient of the non-stratified case with the strong stratified case, it experiences at any rate a slight increase of 4%. Since the streamwise velocity increases due to the stratification effect and the power coefficient is subject a slight increase, this implies that the turbine produces more energy in the case of strong stratification. Specifically, the power that can be extracted in the weak case is equal to 333 W, against the value of 373.3 W obtained in the strong stratification case. The difference is more substantial if we compare the non-stratified case with the strong stratified case, where there is a relative increase of power that amounts to 28%.

Concerning the wake development and recover, the results of the weak stratified case show that the wake is deflected downward by the stratified field. Moving downstream, the wake retrieves the velocity deficit mainly entraining the lateral and the underneath flow field. As concerns the strong stratification, the wake is subject to a remarkable vertical meandering. The wake is pushed downward by the faster fluid of the top layer and the eddy causes the mixing of the two fluids in the bottom area of the domain. The comparison of the velocity deficit between the two cases, highlights that the recovery of the wake is faster for the strong stratified condition. The faster recover of the wake is consistent with the analysis of the total turbulence intensity and shear stresses, indeed these quantities reach higher values in the case of strong stratification. Analyzing the wake shape, it can be observed that as the stratification intensifies, the lateral spreading of the wake increases. The esteem of the wake extent is particularly significant for the arrangement of a cluster of turbines. The assessment of the total power extraction of an array has a substantial dependence on the recovery of velocities wakes deficits. If the wake of an upstream rotor affects remarkably the field of the subsequent turbine the power extracted will be subject to a decrease that is related to the amount of the velocity deficit. Vice versa if the wakes recover faster the turbines can be arranged at lower distances from each other. In this perspective, the faster recover of the wake in case of strong stratification is an important result since it points out that in order to estimate adequately the extent and the recovery of the wake, it's necessary to take into account the stratification characteristics of the sites where marine turbines are installed.

Concerning the effects of the turbine on stratification, we observed that the mixing effect due to the turbine induced forces is more intense in the case of strong stratification. This effect is due to the vertical meandering of the wake and the strong mixing supplied by the eddy that overturns high density fluid over lower density fluid. This is an important result, since indicates that the presence of turbines can modify the environmental dynamics controlled by the stratification and, as a consequence, might influence the development of chemical and biochemical processes.

Since this research represent a first insight into the evaluation of the effects of stable stratified condition on turbine performance and wake characteristics, further studies should be carried out, for example the dimension of the simulation domain might be extended, in particular in the streamwise direction both upstream and downstream. As it can be noticed, in particular analyzing turbulence intensity contour plots of the stratified fields, the presence of the rotor together with the stratification entail an upstream propagation of the disturbance. On the other side increasing the domain downstream extent from the rotor allows to investigate the behavior of the wake in the far region. Another aspect that could be taken into account is the placement of the rotor center in the vertical direction. In the current study we decided to place the rotor center in the middle of the domain were the density profile has the maximum gradient. The relocation of the rotor toward the top or the bottom could alter the dynamics of the wake development. This arrangement should be made according to the conditions of the sites where the turbines should be installed and also in order to identify the best configuration in view of a general efficiency of a turbine farm. Although in the present study, to reach a grid resolution independence, the number of grid cells which covers the rotor area are set widely greater than the threshold indicated by literature, in a future work, in order to assess qualitatively the accuracy of the results, a grid refinement study might be carried out together with a comparison with real site measurement. The achievements above mentioned would be a step toward a forthcoming use of the model as a tool for the application field.

Acknowledgements

The preliminary version of this work was presented during the OWEMES 2017 conference. We acknowledge IEFLUIDS S.R.L. for the use of the software and Regione Friuli Venezia Giulia who has partially financed its development (PAR-FSC 2007-2013).

Bibliography

[1] P.A. Lynn: *Electricity from Wave and Tide-An introduction to Marine Energy*, John Wiley & Sons Ltd., 2014

[2] X. Bai, E.J. Avital, A. Munjiza, J.J.R. Williams: *Numerical simulation of a marine current turbine in free surface flow*, Renewable Energy, vol. 63, pages 715-723, 2014

[3] R. Noruzi, M. Vahidzadeh, A. Riasi: *Design, analysis and predicting hydrokinetic performance of a horizontal marine current axial turbine by consideration of turbine installation depth*, Ocean Engineering, vol. 108, pages 789-798, 2015

[4] P. Mycek, B. Gaurier, G. Germain, G. Pinon, E Rivoalen: *Numerical and Experimental Study of the Interaction between two Marine Current Turbines*, International Journal of Marine Energy, vol. 1, pages 70-83, 2013

[5] M.J. Churchfield, Y. Li, and P.J. Moriarty: *A Large-Eddy Simulation Study of Wake propagation and Power Production in an Array of Tidal Current Turbines*, European Wave and Tidal Energy Conference 2011, Southampton, England, 2011

[6] F. Maganga, G. Germain, J. King, G. Pinon, E. Rivoalen: *Experimental characterization of flow effects on marine current turbine behavior and on its wake properties*, IET Renew. Power Gener., vol. 4, iss. 6, pages 498-509, 2010

[7] T. Blackmore, W.M.J. Batten and A.S. Bahaj: *Influence of turbulence on the wake of a marine current turbine simulator*, Proceeding of the Royal Society A470:20140331, 2014

[8] P. Mycek, B. Gaurier, G. Germain, G. Pinon, E. Rivoalen: *Experimental study of the turbulence intensity effects on marine current turbines behaviour. Part I: One single turbine*, Renewable Energy, vol. 66, pages 729-746, 2014

[9] W. Zhang , C. D. Markfort, F. Porté-Agel: *Wind-Turbine Wakes in a Convective Boundary Layer: A Wind-Tunnel Study*, Boundary-Layer Meteorology, vol. 146, pages 161-179, 2013

[10] M.J. Churchfield , S. Lee, J. Michalakes, P.J. Moriarty: *A numerical study*

of the effects of atmospheric and wake turbulence on wind turbine dynamics, Journal of turbulence, vol. 13, N14, 2012

[11] M. Abkar, F. Porté-Agel: *Influence of atmospheric stability on wind-turbine wakes: A large-eddy simulation study*, Physics of Fluids, vol. 27, 2015

[12] Z. Yang, T. Wan: *Modeling the Effects of Tidal Energy Extraction on Estuarine Hydrodynamics in a Stratified Estuary*, Estuaries and Coasts, vol. 38, pages 187-202, 2015

[13] M. De Dominicis, R. O'Hara Murray, J. Wolf: *Multi-scale ocean response to a large tidal stream turbine array*, Renewable Energy, vol. 114, pages 1160-1179, 2017

[14] Y. Zhiyin: *Large-eddy simulation: Past, present and the future*, Chinese Journal of Aeronautics, vol. 28, pages 1-24, 2015

[15] A. Scotti: *Large Eddy Simulation in the ocean*, International Journal of Computational Fluid Dynamics, vol. 24, pp. 393-406, 2010

[16] R.J.A.M. Stevens, J. Graham, C. Meneveau: *A concurrent precursor inflow method for Large Eddy simulations and applications to finite length wind farms*, Renewable energy, vol. 68, pp. 46-50, 2014

[17] J. Meyers, C. Meneveau: *Optimal turbine spacing in fully developed wind farm boundary layers*, Wind energy, vol. 15, pp. 305-317, 2012

[18] F. Porté-Agel, Y. T. Wu, H. Lu and R.J. Conzemius: *Large-eddy simulation of atmospheric boundary layer flow through wind turbines and wind farms*, Journal of Wind Eng Ind Aerodyn, vol. 99, pages 154-168, 2011

[19] Y.T. Wu, F. Porté-Agel: *A large-Eddy Simulation of Wind-Turbine Wakes: Evaluation of Turbine Parametrization*, Boundary-Layer Meteorol, vol. 138, pages 345-366, 2011

[20] A. M. Abolghasemi , M. D. Piggott, J. Spinneken, A. Viré, C. J. Cotter and S. Crammonde: *Simulating tidal turbines with multi-scale mesh optimisation techniques*, Journal of Fluids and Structures, vol. 66, pages 69-90, 2016

[21] F. Roman, G. Stipcich, V. Armenio, R. Inghilesi, and S. Corsini: *SLarge eddy simulation of mixing in coastal areas*, International Journal of Heat and Fluid Flow, vol. 31, pages 327-341, 2010

[22] J. Smagorinsky: *General circulation experiments with the primitive equations*, Monthly Weather Review, vol. 91, pages 99-164, 1963

[23] R. Mikkelsen: *Actuator disc methods applied to wind turbines*, Diss. Technical University of Denmark, 2003

[24] J.F. Manwell, J.G. McGowan, A.L. Rogers: *Wind energy explained*, John Wiley & Sons Ltd., 2009

[25] M. Calaf, C. Meneveau and J. Meyers: *Large eddy simulation study of fully developed wind-turbine array boundary layers*, Physics of Fluids, vol 22, 015110, 2010

[26] M Calaf, M. B. Parlange and C. Meneveau: *Large eddy simulation study of scalar transport in fully developed wind-turbine array boundary layers*, Physics of Fluids, vol 23, 23:126603, 2011

[27] Y.T. Wu, F. Porté-Agel: *Simulation of turbulent flow inside and above wind farms: model validation and layout effects*, Boundary-Layer Meteorol, vol. 146, pages 181-205, 2013

[28] Y. T. Wu and F. Porté-Agel: *Modeling turbine wakes and power losses within a wind farm using LES: An application to the Horns Rev offshore wind farm*, Renewable Energy, vol. 75, pages 945-955, 2015

[29] L.A.Martinez Tossas and S. Leonrdi: *Wind Turbine Modeling for Computational Fluid Dynamics* NREL/SR-5000-55054, 2013

[30] W.M.J. Batten, M.E. Harrison, A.S. Bahaj: *Accuracy of the actuator disc-RANS approach for predicting the performance and wake of tidal turbines*, Philos Trans A Math Phys Eng Sci, 371(1985), p. 20120293

[31] A. Fernandez: *Numerical prediction of the turbulent wakes generated by a row of marine turbines*, International Journal of Marine Energy, vol 16, pages 41-50, 2016

[32] Q. Hu, Y. Li, Y Di and J. Chen: *A large-eddy simulation study of horizontal axis tidal turbine in different inflow conditions*, Journal of Renewable and Sustainable Energy, vol 9, 064501, 2017

[33] A. Maheri, S. Noroozi, C. Toomer: *Damping the fluctuating behaviour and improving the convergence rate of the axial induction factor in the BEMT based rotor aerodynamic codes*, European Wind Energy Conference and Exhibition 2006, EWEC 2006 - Athens, Greece, vol. 2, pages 1176-1179, 2006

[34] D.C. Maniaci: *An Investigation of WT_Perf Convergence Issues*, 49th AIAA Aerospace Sciences Meeting January 2011, Orlando, Florida, 2011

[35] S.A. Ning: *A simple solution method for the blade element momentum equations with guaranteed convergence*, Wind Energy, vol. 17(9), pages 1327-1345, 2014

[36] S.A. Ning, G. Hayman, R. Damiani, and J.M. Jonkman: *Development and validation of a new blade element momentum skewed-wake model within AeroDyn*, 33rd Wind Energy Symposium, 2015

[37] M.L. Buhl: *A new empirical relationship between thrust coefficient and induction factor for turbulent windmill state*, Technical Report NREL/TP-500-36834, National Renewable Energy Laboratory, August 2005

[38] R.P. Brent: *An algorithm with guaranteed convergence for finding a zero of a function*, The Computer Journal, vol. 14(4), pages 422-425, 1971

[39] Petronio, A., F. Roman, C. Nasello, and V. Armenio: *Large-Eddy Simulation model for wind driven sea circulation in coastal areas*, Nonlinear Processes in Geophysics, vol. 20, pp. 1095-1112, 2013

[40] Galea, A., M. Grifoll, F. Roman, M. Mestres, V. Armenio, A. Sanchez-Arcilla, and L. Zammit Mangion: *Numerical Simulation of Water Mixing and Renewals*

in the Barcelona Harbour Area: The winter season, Environmental Fluid Mechanics, vol. 14, pp. 1405-1425, 2014

[41] M. A. Santo: *Large-eddy simulation of wind-driven circulation in a peri-alpine lake: implications of complex surrounding orography and thermal stratification on hydrodynamics of lake Ledro*, PhD thesis, 2016

[42] I. Balog: *Analysis of fluid-mechanical efficiency of offshore wind turbines from regional to local scale*, PhD thesis, 2014

[43] J. Zang, R. Street, J. Koseff: *A non-staggered grid, fractional step method for time-dependent incompressible Navier-Stokes equations in curvilinear coordinates*, Journal of computational Physics, vol. 114, pages 18-33, 1994

[44] J. Kim, P. Moin: *Application of fractional step to incompressible Navier-Stokes equations*, Journal of Computatonal Physics, vol. 59, pages 308-323, 1985

[45] U. Piomelli: *Wall-layer model for large-eddy simulations*, Progress in Aerospace Sciences, vol. 44, pages 437-446, 2008

[46] A.S. Bahaj, A.F. Molland, J.R. Chaplin, W.M.J. Batten: *Power and thrust measurements of marine current turbines under various hydrodynamic flow conditions in a cavitation tunnel and a towing tank*, Renewable energy, vol. 32, pages 407-426, 2007

[47] A.S. Bahaj, W.M.J. Batten, G. McCann: *Experimental verifications of numerical predictions for the hydrodynamic performance of horizontal axis marine current turbines*, Renewable Energy, vol. 32(15), pages 2479-2490, 2007

[48] T. Stallard, T. Feng, P.K. Stansby: *Experimental study of the mean wake of a tidal stream rotor in a shallow turbulent flow*, Journal of Fluids and Structures, vol. 54, pages 235-246, 2015

[49] J. Sharples, P. Tett: *Modeling the effect of physical variability on the midwater chlorophyll maximum*, Journal of Marine research, vol. 52 (2), pages 219-238, 1994

[50] W.R. Geyer, D.K. Ralston: *The Dynamics of Strongly Stratified Estuaries*, Estuarine and Coastal Science, Elsivier, pages 37-51, 2011

[51] A. Rosen, Y. Sheinman: *The power fluctuations of a wind turbine*, J. Wind Eng. Ind. Aerodyn., vol. 59, pages 51-68, 1996

[52] I.A. Milne, R.N. Sharma, R.G.J. Flay, S. Bickerton: *The role of an onset turbulence on tidal turbine blade loads*, 17th Australasian Fluid Mechanics Conference, Auckland, 2010

[53] V. Armenio, S. Sarkar (2002) An investigation of stably stratified turbulent channel flow using Large-eddy simulation. Journal of Fluid Mechanics 459:1-42

[54] B. Cushman-Roisin, J.M. Beckers: *Introduction to geophysical fluid dynamics*, Academic Press, 2009

[55] G. España, S. Aubrun, S. Loyer, P. Devinant: *Wind tunnel study of the wake meandering downstream of a modelled wind turbine as an effect of large scale turbulent eddies*, J. Wind Eng. Ind. Aerodyn., vol. 101(0), pages 24-33, 2012

[56] S. Kang, X. Yang, F. Sotiropoulos: *On the onset of wake meandering for an axial flow turbine in a turbulent open channel flow*, J. Fluid Mech., vol. 744, pages 376-403, 2014

[57] L.P. Chamorro, C. Hill, S. Morton, C. Ellis: *On the interaction between a turbulent open channel flow and an axial-flow turbine*, J. Fluid Mech., vol. 716, pages 658-670, 2013